

KATHOLIEKE UNIVERSITEIT
LEUVEN

Arenberg Doctoral School of Science, Engineering & Technology
Faculty of Engineering
Department of Electrical Engineering

DEVELOPMENT OF AN AUTOMATED NEONATAL EEG SEIZURE MONITOR

Wouter Deburchgraeve

Dissertation presented in partial
fulfillment of the requirements for
the degree of Doctor
in electrical engineering

September 2010

DEVELOPMENT OF AN AUTOMATED NEONATAL EEG SEIZURE MONITOR

Wouter Deburchgraeve

Jury:
Prof. dr. C. Vandecasteele, president
Prof. dr. ir. S. Van Huffel, promotor
Prof. dr. ir. L. De Lathauwer
Prof. dr. G. Naulaers
Prof. dr. ir. M. Moonen
Prof. dr. ir. B. Puers
Dr. G.H. Visser (Erasmus M.C.)
Dr. P. Govaert (Sophia Child hospital)
Dr. S. Vanhatalo (Helsinki University)

Dissertation presented in partial fulfillment of the requirements for the degree of Doctor in electrical engineering

September 2010

© Katholieke Universiteit Leuven – Faculty of Electrical Engineering
Kasteelpark Arenberg 10, B-3001 Leuven (Belgium)

Alle rechten voorbehouden. Niets uit deze uitgave mag worden vermenigvuldigd en/of openbaar gemaakt worden door middel van druk, fotocopie, microfilm, elektronisch of op welke andere wijze ook zonder voorafgaande schriftelijke toestemming van de uitgever.

All rights reserved. No part of the publication may be reproduced in any form by print, photoprint, microfilm or any other means without written permission from the publisher.

D/2010/7515/74
ISBN 978-94-6018-235-8

Voorwoord

In de eerste plaats wil ik mijn promoter prof. dr. ir. Sabine Van Huffel bedanken voor de kans die ze mij gegeven heeft om een doctoraat te starten in haar onderzoeksgroep. Uw vertrouwen en enthousiasme waren een belangrijke steun om mijn doctoraat succesvol af te leggen. Tevens ben ik het Instituut voor de Aanmoediging van Innovatie door Wetenschap en Technologie in Vlaanderen (IWT-Vlaanderen) erkentelijk voor de financiële ondersteuning door middel van een specialisatiebeurs.

Verder gaat mijn dank uit naar dr. Joseph Perumpillichira en dr. Gerhard Visser van het Erasmus ziekenhuis in Rotterdam voor de steun en het geduld die ze met mij hadden bij het mij bijbrengen van neonataal EEG. Jullie medische inbreng was van bijzonder grote waarde.

Dit werk werd uitgevoerd in de context van een FWO project. Graag bedank ik dan ook Paul, Renate, Joleen, Wilfried, Ewout, Ivana en sinds kort Vladimir voor de altijd weer interessante FWO meetings die we een paar keer per jaar hadden. Met blijdschap zie ik de niet aflatende uitbreiding van de 'neoBrain' groep. Ik hoop van harte dat jullie er in slagen de 'neoGuard' monitor aan het bed van de patiënt te brengen.

De mensen van onze BIOMED onderzoekseenheid verdienen ook een bedanking. Met in het bijzonder Maarten de Vos en Katrien Vanderperren waarmee ik gedurende 4 jaar met veel plezier een bureau gedeeld heb. Maarten, bedankt voor het aangename gezelschap op onze vele reizen. Katrien, bedankt om mij te helpen de vele keren ik verloren liep in de administratie.

Dr. Sampsa Vanhatalo, thank you for your positive criticism about my work and for joining the jury. Also thank you for inviting me to the NOS symposium in Helsinki, it was a highlight of my PhD.

Hoog tijd om mijn ouders, grootouders en familie te bedanken voor hun onvoorwaardelijke steun. Vader en moeder, bedankt voor alle kansen die jullie mij al gegeven hebben en jullie geloof in mij.

Tot slot, Nathalie, bedankt voor je steun en liefde. Ik kijk er naar uit om samen met jouw een mooie toekomst uit te bouwen en al onze plannen te realiseren.

Abstract

Brain function requires a continuous flow of oxygen and glucose. An insufficient supply for a few minutes during the first period of life may have severe consequences or even result in death. This happens in one to six infants per 1000 live term births. Therefore, there is a high need for a method which can enable bedside brain monitoring to identify those neonates at risk and be able to start the treatment in time. The most important currently available technology to continuously monitor brain function is ElectroEncephaloGraphy (or EEG). Unfortunately, visual EEG analysis requires particular skills which are not always present round the clock in the Neonatal Intensive Care Unit (NICU). Even if those skills are available it is laborsome to manually analyse many hours of EEG. The lack of time and skill are the main reasons why EEG is not widely used in the NICU although many involved agree it should be.

The work presented in the current thesis aims at finding methods for automated analysis of neonatal EEG to facilitate its use in the NICU. In this thesis we focused on one of the most important treatable phenomena in neonatal EEG, namely neonatal seizures. Neonatal seizures are an important sign of central nervous system dysfunction and require immediate medical attention. The majority of neonatal seizures are subclinical, being detected only by EEG monitoring. Hence, there is scope for an automated EEG based seizure monitoring system.

The most important topic covered by this thesis is automated seizure detection. We identified the two main types of neonatal seizures and developed an appropriate detection strategy for each by mimicking the human observer reading EEG. The methods were validated on a large dataset. An implementation of the seizure detection able to run in real-time has been developed and succesfully tested at the bedside.

The EEG contains many artifacts of which some have similar morphology to neonatal seizures. These artifacts may lead to false positive detections by the seizure detector and therefore should be removed. We identified the most important artifacts in neonatal EEG leading to false positives and removed them using Independent Component Analysis (ICA). We quantify the benefit of artifact removal on seizure EEG by measuring the performance of the developed seizure

detector with and without artifact preprocessing.
As we are using the full 13 up to 17 channel EEG we have the ability to exploit the spatial resolution of the EEG. Therefore we developed two seizure localization methods based on Canonical / Parallel Factor Analysis (CPA) which are able to extract the spatial distribution of the seizure on the scalp. These distributions can be visualized to the user using topographic plots. Analysis of these plots leads to information about the depth of the seizure (cortical or subcortical), number of seizure foci present, spread of seizures to contralateral hemisphere, etc. Especially for the target public of non-expert users of EEG, these topographic plots provide easy understanding of the spatial information contained in the EEG which would otherwise need years of training. Both methods are validated on a large dataset. In this thesis we also provide a proof of concept study in which these methods are combined with dipole source localization in a realistic head model. This technology can be used to study the relationship between seizure localization and the location of brain damage as seen on Magnetic Resonance Imaging (MRI).
In the final chapter we propose three types of EEG monitors with increasing complexity that integrate the developed algorithms. Each of these would significantly improve neonatal seizure monitoring and hopefully we will see a commercial implementation in the future.

Korte inhoud

De hersenen hebben een continue toevoer nodig van zuurstof en glucose. Een onvoldoende toevoer gedurende een aantal minuten tijdens de eerste levensuren van een baby kunnen ernstige gevolgen en zelfs leiden tot de dood. Dit gebeurd in 1 tot 6 per 1000 voldragen geboortes. Hierdoor is er een hoge nood aan een monitor die toelaat om aan het bed van de patiënt de hersenen te bewaken. Dergelijke bewaking laat toe deze patiënten te identificeren en een behandeling te starten. De op dit moment belangrijkste beschikbare technologie om de hersenen continu te bewaken is ElectroEncephaloGraphy (of EEG). Jammer genoeg vereist visuele EEG analyse gespecialiseerde kennis die niet altijd beschikbaar is op de neonatale intensieve zorg. Een bijkomend probleem is dat dergelijke analyse zeer arbeidsintensief is. Het gebrek aan tijd en kennis zijn de voornaamste redenen dat EEG nog niet standaard in gebruik is op de neonatale intensieve zorgen.
Het doel van het voorgestelde werk in deze thesis is het ontwerp van algoritmes die op een geautomatiseerde manier het EEG analyseren zodat EEG bruikbaar wordt op de neonatale intensieve zorg. Hierbij lag de focus op één van de belangrijkste behandelbare fenomenen in het EEG, namelijk neonatale convulsies. Deze convulsies zijn een belangrijk signaal dat er iets mis is met het centrale zenuwstelsel en vereisen onmiddellijk medische zorg. Het merendeel van deze convulsies kunnen enkel met EEG gedetecteerd worden. Vandaar de nood aan een geautomatiseerde EEG convulsie monitor.
Het belangrijkste onderwerp van deze thesis is geautomatiseerde convulsie detectie. We hebben de 2 belangrijkste types van neonatale convulsies geïdentificeerd en voor elk werd een detectie algoritme ontworpen die de menselijke observator nabootst. Deze algoritmes zijn gevalideerd op een grote dataset. Een implementatie van dit algoritme dat in reële tijd kan werken werd ontwikkeld en succesvol getest aan het bed van de patiënt.
Het EEG bevat echter vele artefacten waarvan er een aantal dezelfde vorm hebben als convulsies. Deze artefacten leiden tot vals positieve detecties door de convulsie detector en moeten dan ook verwijderd worden. We hebben de 3 belangrijkste artefacten in neonataal EEG geïdentificeerd en een algoritme ontworpen die ze met behulp van Independent Component Analysis (ICA) uit het EEG kan verwijderen.

Doordat we 13 tot 17 EEG kanalen gebruiken is er heel wat spatiële informatie beschikbaar. Daarom werden 2 convulsie lokalisatie algoritmes ontwikkeld, gebaseerd op Canonical / Parallel Factor Analysis (CPA), die in staat zijn om de spatiële distributie van de convulsies te extraheren. Deze distributies kunnen gevisualiseerd worden aan de gebruiker door middel van topografische plots. Analyse van deze plots leidt tot informatie over de diepte van de convulsie (corticaal of subcorticaal), het aantal foci van de convulsie, spreiding van de convulsie naar de contralaterale hemisfeer, enz. Deze topografische plots maken de spatiële informatie in het EEG toegankelijk voor niet gespecialiseerde gebruikers. In deze thesis voorzien we ook een experimentele studie waarbij we de spatiële distributie van de convulsie combineren met dipoollokalisatie in een realistische hoofdmodel. Deze technologie kan gebruikt worden om het verband tussen de lokatie van de convulsie op de schedel en de precieze lokatie van de hersenschade te onderzoeken.
In het laatste hoofdstuk van de thesis stellen we 3 types van EEG monitors met toenemende complexiteit voor die van de ontwikkelde algoritmes gebruik maken. Elk van deze types is een significante verbetering van neonatale convulsie bewaking zoals die vandaag gedaan wordt. Hopelijk zien we dan ook in de toekomst een commerciële implementatie.

Nomenclature

List of symbols

$a, b, \ldots$	scalars
$\mathbf{a}, \mathbf{b}, \ldots$	vectors
$\mathbf{A}, \mathbf{B}, \ldots$	matrices
$\mathcal{A}, \mathcal{B}, \ldots$	tensors
$a_{ijk}, (\mathcal{A})_{ijk}$	element of $\mathcal{A}$ at position (i, j, k)
$\mathbf{I}$	identity matrix
i	$\sqrt{-1}$

Sets of numbers

$\mathbb{R}$	the set of real numbers

Basic operations

$\mathbf{A}^T$	transpose of the matrix $\mathbf{A}$
$\mathbf{A}^{-1}$	inverse
$[\mathbf{a}\,\mathbf{b}]$	matrix with columns $\mathbf{a}$ and $\mathbf{b}$
$\lvert a \rvert$	absolute value of a
$\langle \cdot, \cdot \rangle$	inner/scalar product
$\lVert \mathbf{A} \rVert$	Frobenius norm, $\sqrt{\text{trace}(\mathbf{A}^T \mathbf{A})}$
Σ	sum
$\prod$	product
$\times$	Cartesian product, $A \times B := \{(a_i, b_j)\}$
$\mathbf{a} \circ \mathbf{b}$	outer product of vectors $\mathbf{a}$ and $\mathbf{b}$
$\in$	belongs to

Abbreviations

AEEG	Amplitude integrated Electroencephalogram
BS	Burst Suppression
BSS	Blind Source Separation
BSR	Burst Suppression Rate
Candecomp	Canonical Decomposition
CCA	Canonical Correlation Analysis
CFM	Cerebral Function Monitor
CLM	Central Limit Theorem
CPA	Candecomp/Parafac Analysis
CSF	Cerebrospinal Fluid
ECG	Electrocardiogram
EEG	Electroencephalogram
EMG	Electromyogram
EVD	EigenValue Decomposition
EOG	Electro-oculogram
FFT	Fast Fourier Transform
FIR	Finite Impulse Response
FT	Fourier Transform
HIE	Hypoxic Ischaemic Encephalopathy
HOS	Higher-Order Statistics
HOSVD	Higher-Order Singular Value Decomposition
ICA	Independent Component Analysis
ICU	Intensive Care Unit
JADE	Joint Approximate Diagonalization of Eigenmatrices
O-CP	Oscillatory Candecomp Parafac
STFT	Short Time Fourier Transform
SVM	Support Vector Machine
MA	Moving Average
MR	Magnetic Resonance
MRI	Magnetic Resonance Imaging
NICU	Neonatal Intensive Care Unit
Parafac	Parallel Factor Analysis
PCA	Principal Component Analysis
RRE	Relative Residual Energy
SOBI	Second Order Blind Identification
SP-CP	Spike Candecomp Parafac
SNR	Signal to Noise Ratio
SVD	Singular Value Decomposition

Contents

Voorwoord i

Abstract iii

Notation vii

Contents ix

1 Overview 1

1.1 Introduction 1

1.2 Collaborations 4

1.3 Contributions 4

1.4 Chapter-by-chapter overview 5

2 Background: The brain and brain monitoring 9

2.1 The brain 9

2.1.1 Anatomy of the brain 9

2.1.2 Electrical brain activity 10

2.2 Electroencephalography or EEG 13

2.2.1 Scalp EEG 13

2.2.2 History of EEG 18

2.2.3 Practical applications of EEG 19

2.3 The neonatal brain 19
2.3.1 Neonatal brain damage 19
2.3.2 EEG monitoring of the neonate 20
2.3.3 Neonatal seizures 25
2.3.4 Neonatal EEG at the bedside 27
2.3.5 Artifacts in the neonatal EEG 28
2.3.6 Treatment options 30

3 Background: Mathematical techniques 35

3.1 Introduction 35
3.2 Rank of a matrix and the Singular Value Decomposition (SVD) . . 36
3.3 Principal Component Analysis (PCA) 37
3.4 Blind Source Separation (BSS) 38
3.4.1 The cocktail party problem 38
3.4.2 Independent Component Analysis (ICA) 39
3.5 Canonical / Parallel factor Analysis (CPA) 42
3.6 Fourier transform (FT) 44
3.7 Wavelet transform (WT) 47
3.8 Signal properties 49
3.8.1 Energy of a signal 49
3.8.2 Entropy of a signal 51

4 Automated neonatal seizure detection 53

4.1 Introduction 53
4.2 Detection methods 54
4.2.1 Detection strategy 54
4.2.2 Spike train type seizure detection 56
4.2.3 Oscillatory type seizure detection 64

4.2.4 Performance measures 69
4.3 Evaluation of the algorithm 71
4.3.1 Dataset 71
4.3.2 Results 71
4.4 Discussion 74

5 Automated removal of artifacts in the neonatal EEG 77
5.1 Frequency filters 77
5.1.1 Notch Filters 77
5.1.2 Finite Impulse Response (FIR) filter 78
5.2 BSS for artifact removal 79
5.2.1 Introduction 79
5.2.2 Methods 81
5.2.3 Results 88
5.2.4 Discussion 92

6 CPA for neonatal seizure localization 95
6.1 Introduction 95
6.2 Methods 96
6.2.1 CP decomposition 96
6.2.2 O-CP decomposition method 96
6.2.3 SP-CP decomposition 99
6.2.4 Spike triggered averaging 100
6.3 Results 101
6.3.1 Illustration of the application of the O-CP method 101
6.3.2 Illustration of the application of the SP-CP method 103
6.3.3 Robustness of the SP-CP method and comparison with spike triggered averaging 104
6.3.4 Comparison with visual analysis of the EEG 106

6.4 Discussion 109
6.4.1 Application of both methods to the same seizure 109
6.4.2 Dynamic seizures 109
6.4.3 Interpretation of the topographic plots 110
6.4.4 Comparison between topographic plots and visual analysis of the EEG 110
6.4.5 Practical applications of the methods 110

7 Neonatal seizure localization in a realistic head model. 113
7.1 Introduction 113
7.2 Materials and methods 114
7.2.1 Spatial distribution of the seizures on the scalp 114
7.2.2 MRI segmentation 115
7.2.3 Dipole source localization 115
7.2.4 Combination of methods 117
7.3 Results 117
7.4 Discussion 118

8 CPA applied to EEG transients and time varying EEG activity 121
8.1 SP-CP transient analysis 121
8.1.1 Application to a patient with a thalamic bleed 121
8.1.2 Application to complex occipito-frontal spikes 123
8.1.3 Discussion 124
8.2 O-CP analysis for EEG dynamics 124
8.2.1 Introduction 124
8.2.2 Method 124
8.2.3 Results 127
8.2.4 Discussion 132

9 On and Off-line software development and concepts for commercialisation 133

9.1 Graphical User Interface 133

9.2 Proof of concept at the bedside 135

9.3 Concepts for commercialisation 136

9.3.1 Basic 2-channel system 136

9.3.2 Basic multi-channel system 137

9.3.3 Advanced multi-channel system 137

9.4 Conclusion 138

10 Conclusions and open problems 139

10.1 General conclusions of the thesis 139

10.1.1 Neonatal seizure detection 139

10.1.2 Artifact removal 140

10.1.3 Neonatal seizure localization 140

10.1.4 Additional conclusions 141

10.2 Future work and open problems 141

10.2.1 Burst-suppression monitoring 141

10.2.2 Entropy analysis 142

10.2.3 Polysomnography analysis 143

Bibliography 147

Publication list 165

Curriculum vitae 169

Chapter 1

Overview

1.1 Introduction

Survival of neonates being treated in the Neonatal Intensive Care Unit (NICU) has greatly improved over the last decades, especially for preterms (Fig. 1.1, [86]). The numbers in Fig. 1.1 might be a bit optimistic but the trend is clear. This is mainly due to sophisticated artificial ventilation techniques, the use of pre- and post-natal steroids and the use of exogenous surfactant [115]. Neonates with perinatal brain damage from various etiology are an important subgroup for which these advancements can not fully prevent adverse neurodevelopmental outcome. Perinatal asphyxia in particular is an important cause of brain injury. It may lead to hypoxic-ischaemic encephalopathy (HIE) which occurs in one to six of every 1000 full term births [197, 44]. Because of the increased survival of preterms and in a constant quest of improving the outcome of neonates with brain damage, the focus in the NICU is gradually changing from mere survival techniques to increased bedside monitoring. Anyone visiting a NICU will be struck by the amount of equipment needed to monitor all the vital parameters, such as ElectroCardioGram (ECG), heart rate, blood pressure, respiration, oxygen saturation, etc. Many of these parameters are dedicated at making sure, the brain is in a good condition. Yet, the brain itself is often not directly measured. This is odd as there is a good modality to measure the functional activity of the brain, namely ElectroEncephaloGraphy or EEG. EEG measures the electrical activity of the brain using small electrodes attached to the scalp (Fig. 1.2). Many involved agree that EEG is highly valuable for brain monitoring of critically ill neonates. Yet, EEG is not standard practice in the NICU. The most important reasons for this absence is that the analysis of long-term EEG recordings of neonates is labor intensive, time consuming, expensive, requires specialized skills and can not be

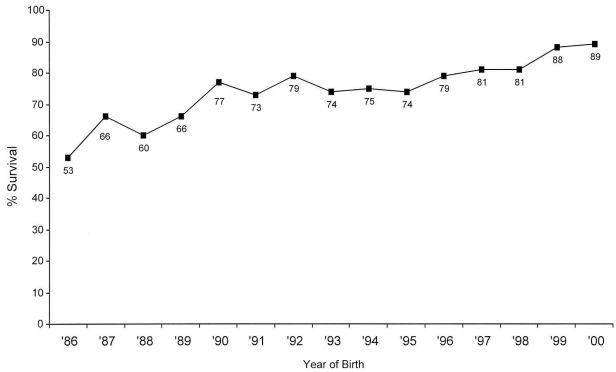

Figure 1.1: *Survival by year for preterms with gestational ages of 23 to 26 weeks. From [86].*

done at the bedside. Chapter 2 will discuss EEG into more detail.

One of the most important phenomena that can be observed in the EEG of neonates with brain damage are neonatal seizures. These are the most frequent major manifestation of neonatal neurological disorders [112, 215]. Seizures occur in a significant fraction of newborns. In prematures and low-birthweight infants, seizure incidence can even rise up to 25% [221]. The majority of the seizures occurring in neonates admitted to the NICU are subclinical, being detected only by EEG monitoring [82, 140]. To accurately detect neonatal seizures constant supervision of the EEG signal by a trained EEG specialist would be needed, which is not possible. Automated processing of the EEG, in order to eliminate the need of the specialist, is the key to bring EEG into the NICU. Therefore, there is a strong need for automated computerised EEG monitoring techniques that allow reliable detection of epileptiform discharges, including those not accompanied by clinical phenomena. This will allow fast decision making without the need for constant on-site expert supervision [209].

The goal of this thesis is to develop an automated EEG seizure monitor for term neonates after perinatal asphyxia. The main task of the monitor is to automatically detect the seizures and give an alarm to the people treating the neonate. This automated EEG analysis has to operate inside very narrow boundaries if it is to be accepted as a routine tool by the EEG community. Most of the empirical knowledge in clinical EEG analysis is based on visual pattern recognition, therefore automatic analysis must be shaped by the way the clinician sees the EEG. In this thesis, special care was taken in developing methodologies that are compatible to the knowledge of clinicians. The 'human observer' was always the starting point and a source of inspiration for a new method. This first chapter will give an

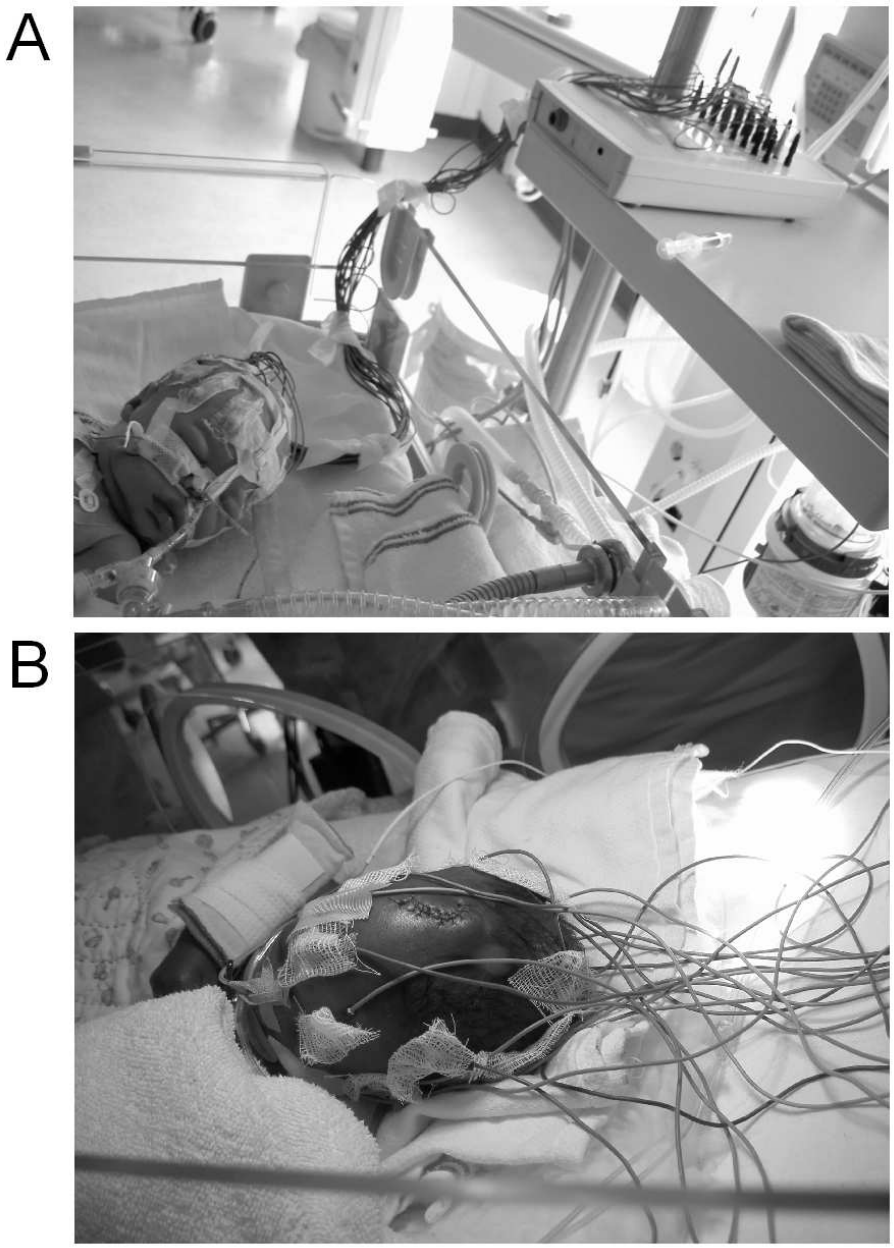

Figure 1.2: *EEG measurement of a newborn. Small electrodes are fixed to the scalp of the neonate to measure the electrical activity of the brain.*

overview of the contributions of this thesis dedicated to automation of neonatal EEG and in particular neonatal seizure monitoring.

1.2 Collaborations

The work presented in this thesis would not have been possible without the collaboration with many other people. This is an overview of the research groups involved and their respective responsibilities in the project.

- Department of Neonatology, Erasmus MC, University Medical Center Rotterdam. This department is where the neonates are being treated and where all the measurements are performed.
- Department of Clinical Neurophysiology, Erasmus MC, University Medical Center Rotterdam. This department is responsible for the interpretation and scoring of the recorded EEG signals.
- Image Processing and Interpretation Research Group (IPI) of the department of Telecommunications and Information Processing (TELIN) of the Faculty of Engineering at Ghent University (Universiteit Gent). This research group is responsible for the segmentation of the MR images and the building of the realistic head model. Chapter 7 is done in collaboration with this research group.
- Medical Imaging and Signal Processing (MEDISIP) of the department Electronics and Information systems (ELIS) of Faculty of Engineering at Ghent University (Universiteit Gent). This research group kindly provided us dipole source localization code and helped us to estimate the dipole in a realistic head model. Chapter 7 is done in collaboration with this research group.

1.3 Contributions

The most important contributions of this thesis to neonatal seizure EEG monitoring are three-fold.

1. Automated seizure detection: We developed two algorithms that automatically detect neonatal seizures in the EEG with high sensitivity and low amount of false positive detections.
2. Automated artifact removal: We developed an algorithm based on ICA-BSS that removes the three most important artifacts in neonatal EEG that

disturb seizure detection. These algorithms lower the amount of false positive detections without lowering the sensitivity for detection of true seizures.

3. Automated seizure localization: We developed two methods based on CPA that are able to extract the spatial distribution of the seizures on the scalp. These methods can make the spatial information present in the EEG available to inexperienced users.

Additional contributions:

1. Seizure localization in a realistic head model (in collaboration with the IPI and MEDISIP research groups of UGent).
2. General analysis algorithm for transients in the EEG originating from the same brain region (e.g. due to several pathologies like thalamic bleed, complex abnormal occipito-frontal spikes, interictal epileptiform spikes).
3. Time varying localization of activity in the EEG.
4. Software development for offline EEG analysis.
5. Real-time bedside seizure detection. The software for offline EEG processing was adapted to be able to run in real-time at the bedside. This allowed us to build a proof of concept setup for seizure detection at the bedside.

1.4 Chapter-by-chapter overview

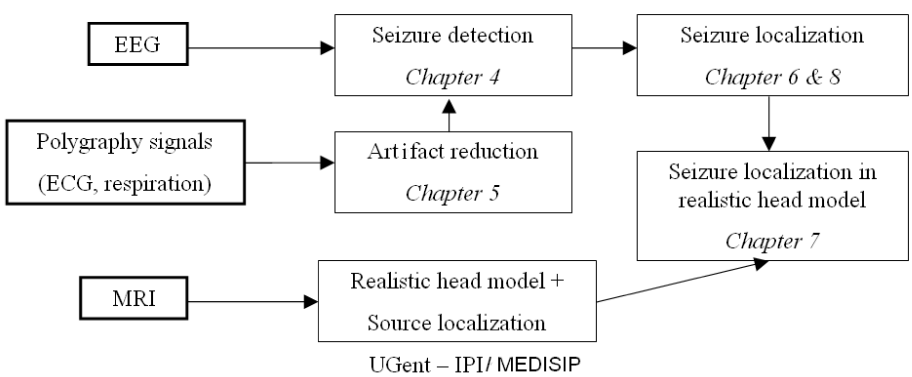

Figure 1.3: *Schematic overview of link between the most important chapters in the thesis.*

Chapter 2

Chapter 2 provides the necessary medical and technical background to the brain and brain monitoring. The chapter starts with an explanation of the basic structure of the brain and how electrical activity is generated. Next, we explain the basics of EEG monitoring to record the electrical brain activity and discuss its most important features. Next, we discuss the neonatal brain and how brain damage may occur and be treated. Finally, we explain the most important characteristics of neonatal EEG.

Chapter 3

Chapter 3 provides the necessary technical background of the techniques used throughout this thesis. We discuss the most important data decomposition techniques together with spectrum estimation with Fourier, time-frequency analysis with wavelets and the signal properties energy and entropy.

Chapter 4

Chapter 4 describes the development of the automated neonatal seizure detector. Neonatal seizures are split up into two basic types, the spike train and oscillatory type. For each type a separate seizure detector is developed. The detector is validated on a large dataset.

Chapter 5

Neonatal EEG recordings are sometimes obscured by different types of artifacts. Some of them have similar morphology as neonatal seizures and lead to false positive detections by the seizure detector. In this chapter the three most important artifacts leading to false positives are removed from the EEG using Blind Source Separation (BSS). This leads to an improved seizure detection. The method is validated on a large dataset.

Chapter 6

Chapter 6 describes the development of two CPA based methods (SP-CP and O-CP) that are able to extract the spatial distributions of neonatal seizures on the scalp. These methods provide additional information about the seizures to the neurophysiologist. The methods are validated on a large dataset.

Chapter 7

The spatial distributions obtained in chapter 6 can be used for source localization of seizures in a realistic head model. For this application we need the spatial distribution obtained from EEG, a segmented MRI and a source localization method. We illustrate the feasability of the combined methods on a set of patients. In a later phase, the combined methods can be used to study the relationship between EEG phenomena (e.g. seizures) and structural brain damage as seen on MRI.

Chapter 8

The methods developed in chapter 6 can be extended and used for other applications. SP-CP can be used as a general method for transient analysis in the EEG. We illustrate it's application on transients of an adult patient with a thalamic bleed and on transients of children with complex occipito-frontal spikes. The O-CP method can be extended with SVD analysis to analyze time varying activity in the EEG.

Chapter 9

Chapter 9 describes the software that was developed for on- and offline analysis of neonatal EEG. Several concepts for commercialization are proposed. Ranging from a simple 2 channel system to a full 17 channel EEG monitor.

Chapter 10

The last chapter gives several suggestions for further research. This further research should mainly be oriented to background EEG monitoring and polysomnography analysis and integration thereof. Finally, we summarize the important findings of this work.

Chapter 2

Background: The brain and brain monitoring

In this chapter an introduction is given to the medical background of the thesis. First, the anatomy and generation of electrical activity of the brain is discussed. Next, electroencephalography (EEG) or the technique by which we measure the electrical activity is described. Finally, the necessary medical background on the neonatal brain and neonatal EEG is given.

2.1 The brain

2.1.1 Anatomy of the brain

The brain consists of 2 symmetric hemispheres. The cortex, or outer layer of the brain, is divided into 4 lobes, i.e., the frontal, parietal, occipital and temporal lobe (Fig. 2.1). Each of these lobes contains many distinct areas that control different functions. The cortex is about 1.5-4.0 mm thick and consists of nerve cells, which are darker in colour and therefore called grey matter. The larger inner part of the brain is lighter and therefore called the white matter and consists only of the axons of the nerve cells. Fig. 2.2 shows a horizontal slice through the brain on which the white and grey matter can be distinguished.

The surface of the brain is convoluted and the furrows are called sulci while the ridges are called gyri. The division into sulci and gyri is mainly used in anatomy, while physiologists rather talk about functional areas, e.g. according to

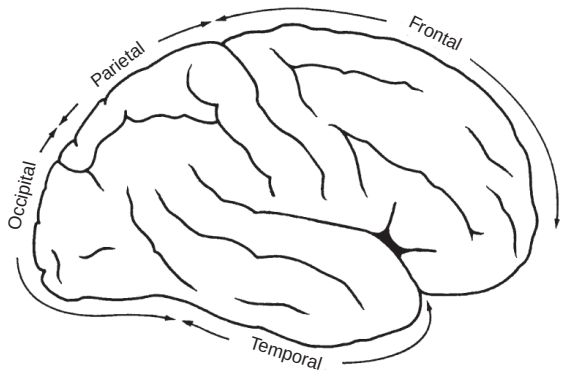

Figure 2.1: *Each hemisphere of the brain is divided in four different lobes. From [103].*

Brodmann. Tissue in such an area has the same histological pattern and thus similar functionality.

The brain consists of about 10^{10} nerve cells or neurons. Neurons possess dendrites, a cell body, an axon and synaptic terminals, as illustrated in Fig. 2.3. Dendrites extend from the cell body and share with it the function of receiving information from synaptic connections with adjoining neurons.

2.1.2 Electrical brain activity

The sources of the electrical activity in the brain measurable with EEG are cortical. These sources produce potential fields which can be recorded on the scalp as a time-varying voltage. The principal generators of the EEG are the synaptic potentials of pyramidal neurons (either excitatory or inhibitory) [149]. Each synapse acts like a battery driving current in a small loop. The field potentials around individual cells are very small, and they would not be recordable at the scalp except for the fact that the pyramidal cells are all algined perpendicular to the surface of the cortex. Therefore, if the activity is synchronous, the voltage fields produced by individual cells can summate to produce a potential large enough to be recorded at the scalp.
Neurons, like other cells, are electrically polarized so that their interior is negatively charged with respect to the outside of the cell. This potential difference, called the resting potential, is due to an unequal distribution of mainly Na^+, K^+ and Cl^- ions across the cell membrane. The electrical force that will act on the different

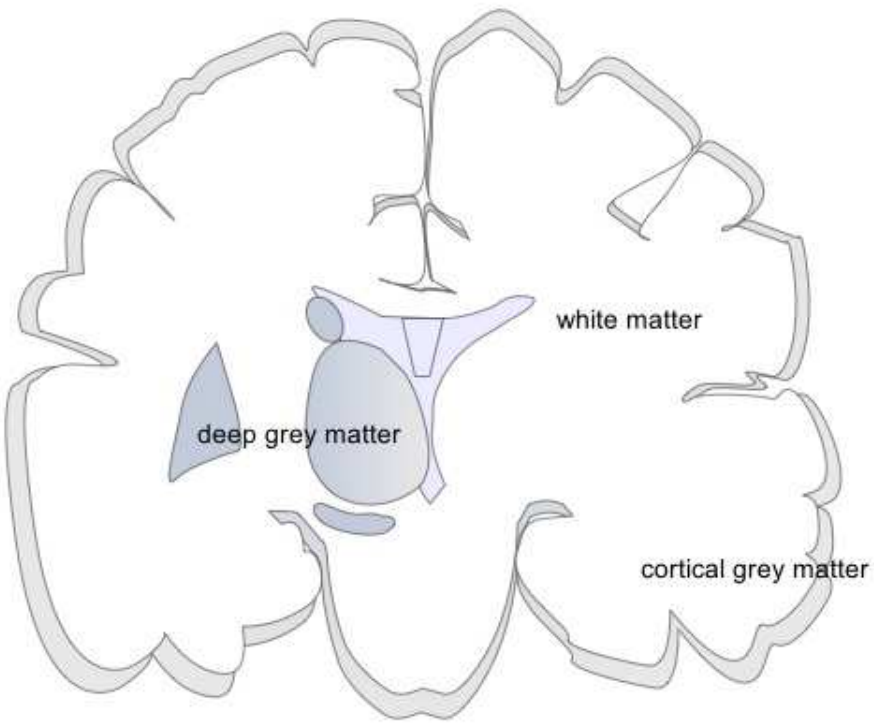

Figure 2.2: *A horizontal slice through the brain. The cortical grey matter, consisting of cell bodies and dendrites, can be found at the outmost surface of the brain (the cortex) and in some deeper structures. The inner part of the brain contains the axons of the nerve cells and is called white matter.*

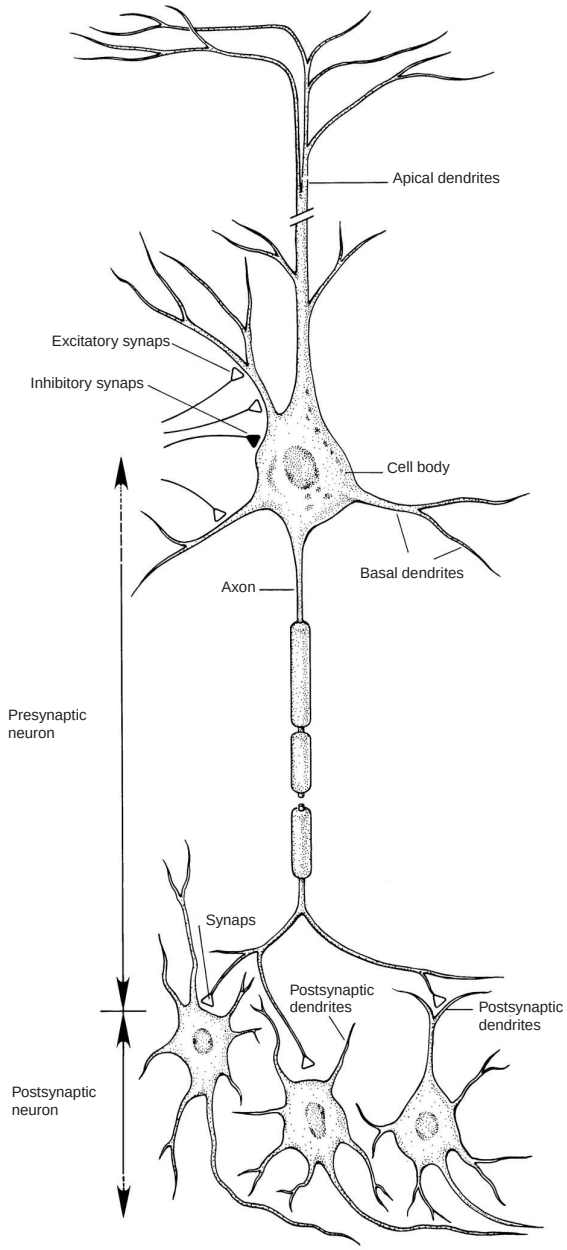

Figure 2.3: *The basic parts of a neuron are the cell body, dendrites, the axon and synaptic terminals. From [30].*

ions can be calculated from the Nernst equation:

$$E_M = \frac{RT}{nF} ln \frac{[M]_o}{[M]_i} \tag{2.1}$$

where R is the universal gas constant, T is temperature, n is the valence of the ion M, F is Faraday's constant, and $[M]_0$ and $[M]_i$ are the concentrations of M outside and inside the cell respectively. To calculate the membrane potential E_M, the following equation can be used:

$$E_M = \frac{RT}{F} ln \frac{P_K[K]_o + P_{Na}[Na]_o + P_{Cl}[Cl]_i}{P_K[K]_i + P_{Na}[Na]_i + P_{Cl}[Cl]_o} \tag{2.2}$$

Typical values for this resting potential are around -70 mV [179, 195, 30].

The membrane potential is the result of ions that can pass rather freely through the membrane (e.g. K^+ and Cl^-) and an active mechanism, namely the sodium-potassium pump, which pumps sodium (Na^+) out of the cell and potassium (K^+) into the cell. Since this pump is an active mechanism, it is energy consuming. The energy is received by using the cell's storage of adenosine triphosphate (ATP) and phosphocreatine. The major production of ATP and phosphocreatine is used to maintain the membrane potentials.

The resting potential can be disturbed by several millivolts by postsynaptic potentials. Depending on the chemical nature of the neurotransmitter released in the synaptic cleft, the postsynaptic membrane is depolarized (excitatory postsynaptic potential) or hyperpolarized (inhibitory postsynaptic potential). Excitatory currents, involving Na^+ or Ca^{2+} ions, flow inwardly towards an excitatory synapse and outwardly away from it. Inhibitory loop currents, involving Cl^- or K^+ ions, flow in the opposite direction. As every neuron has many synapses connecting to different neurons, the actual potential over a cell membrane is given by the spatial and/or temporal summation of the postsynaptic potentials. When the neuronal cell is depolarised beyond a critical level, an action potential is generated that proliferates along the axon and neurotransmitters are released. Excitatory postsynaptic potentials increase the chance of an action potential. Inhibitory postsynaptic potentials suppress action potentials.

2.2 Electroencephalography or EEG

2.2.1 Scalp EEG

A widely used standard for placing and denoting EEG electrodes on the scalp is the 10-20 system [95, 147]. This electrode placement provides a uniform coverage of the entire scalp. The landmarks for this system are the nasion and the inion

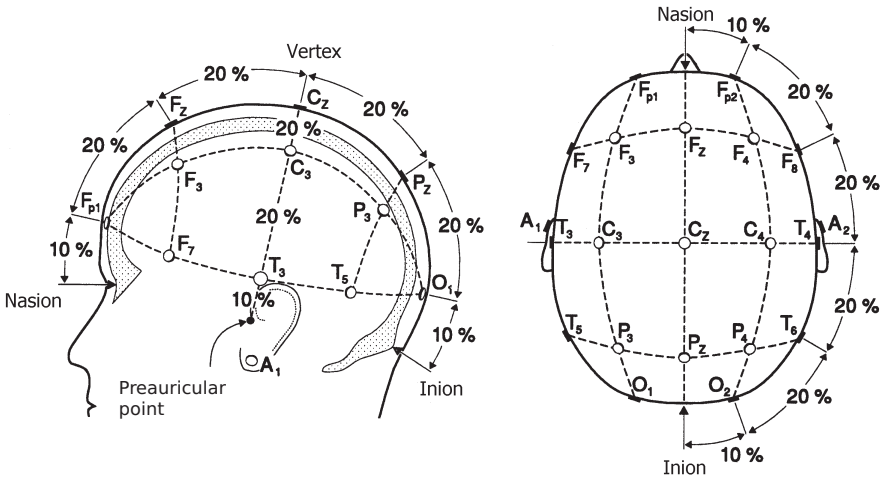

Figure 2.4: *The standard electrode placement according to the 10-20 international system: side view and top view of the head. It uses the distances between bony landmarks (the nasion, inion and preauricular points) of the head to generate a system of lines that run across the head and intersect at intervals of 10 or 20% of their total length. Electrodes are placed at the intersections. From [124].*

(Fig. 2.4). The distance between these point over the skull and between the ears is divided in 10% and 20% parts, which define 21 electrode positions. The first letter in the electrode name indicates which region it is placed over: F for frontal lobe, C for the central line dividing the head in a rear and front half, P for parietal lobe, O for occipital lobe, and T for temporal lobe. The numbers in the electrode name are odd for the left hemisphere and even for the right, and increase with increased distance from the longitudinal fissure.

Time domain properties of the EEG

The most common way to analyze EEG is by visual inspection in the time domain. Time domain resolution of EEG is excellent and in the order of ms. The amplitude of scalp EEG ranges normally from 5 μV to several hundred μV. The frequency content ranges from 0.01 Hz to several hundred Hz, but conventionally these frequencies are filtered off using a low-pass filter at around 50-70 Hz [212]. Normally the EEG is visualised in 10 s time windows showing all channels simultaneously. An overview of the essential characteristics of EEG analysis is given [51]:.

1. Wavelength (in time)
2. Voltage (amplitude)

3. Waveform (morphology)
4. Regulation (sustained activity)
   (a) Frequency (sustained rhythm in which the mean frequency does not vary significantly)
   (b) Voltage (smoothness of the envelope of the waxing and waning of voltage)
5. Manner of occurrence (random, serial, continuous)
6. Locus
7. Reactivity (eye opening, mental calculation, acapnia, sensory stimulation, movement, affective state)
8. Interhemispheric coherence (homologous areas)
   (a) Symmetry
   (b) Synchrony

As the EEG measures the time course of potential differences between electrodes, a reference for this potential difference has to be chosen. The most used reference systems are bipolar reference, the Laplacian derivation, the average reference, and the linked-ears reference [62]. With an average reference, all potentials are displayed with respect to the average value of all electrodes. In linked-ears reference, the EEG is displayed with respect to the average of the potentials at the ear lobes (which should be ideally zero). Both are good for visualizing widespread coherent waveforms. These waveforms occur with similar amplitude and phase. In bipolar and Laplacian montage, the shown EEG signals are obtained by subtracting neighboring electrode signals. These are best suited for viewing highly localised activity over a limited area of the scalp because the widespread waveforms are filtered out.

Frequency domain properties of the EEG

The frequency distribution is important when characterizing the EEG. Many EEG phenomena are described based on their frequency content. Different oscillations are the result of different underlying mechanisms. The EEG is commonly divided in 4 frequency bands as follows and illustrated in Fig. 2.5.

- Delta: $0.5 \leq f < 4$Hz;
- Theta: $4 \leq f < 8$Hz;
- Alpha: $8 \leq f < 13$Hz; and

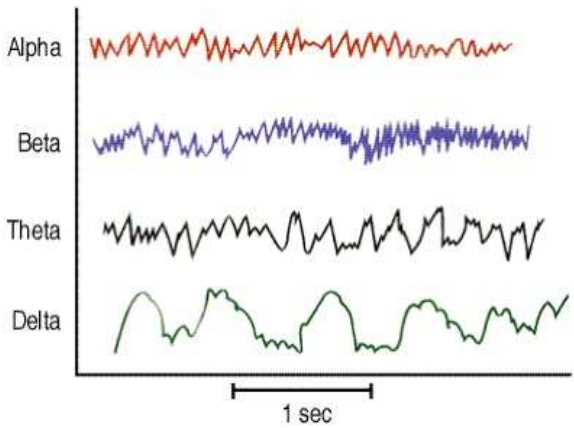

Figure 2.5: *Different brain traces, from bottom to top: examples of (1) delta rhythm (0.5-4Hz); (2) theta rhythm (4-8Hz); (3) beta rhythm (13-30Hz); (4) alpha rhythm (8-13Hz).*

- Beta: $13 \leq f < 30$Hz.

In many cases there is a strong relationship between the frequency content of the EEG and the behavioral state of the patient from being awake and alert to asleep. Note that in neonates, alpha and beta activity are not physiologically present. There are activities at the same frequency range, but their characteristics are different from older infants or adults.

- Delta waves occur in infants and during deep sleep or anaesthesia.
- Theta waves are most prominent in small children and during drowsiness or light sleep.
- Alpha waves occur in waking and resting state e.g. when a person is relaxed and inattentive. High amplitude when eyes are closed. Mostly sinusoidal in shape.
- Beta waves occur when a person is actively attending to events. They are often divided into two sub-bands. The lower frequencies are present during mental activty, while the higher frequencies are associated with tension and intense activation of the central nervous system.

Limitations of scalp measurement

An EEG registers the electrical activity between neurons using electrodes on the scalp. There are three important variables in determining whether cerebral potentials are recordable from the scalp [61, 174]. These are source area, source depth and source orientation. It takes a combined synchronous electrical activity of approximately 10^8 neurons in a cortical area of minimum 6 cm^2 to create visible EEG. These large cortical networks are activated via thalamo-cortical (th-cx) or cortico-cortical (cx-cx) connections [211]. Smaller regions are not visible due to the attenuating properties of the skull. Sometimes smaller sources can be detected by averaging multiple repetitive signals, such as evoked potentials in sensory stimuli. It is also known that the brain acts as a low-pass filter that averages out fast potentials [49]. Deeper brain sources are less well recorded, first of all, these are more attenuated by the different brain layers before reaching the scalp [66] and secondly, the number of cortical neurons is much larger than subcortical neurons. Therefore, scalp EEG is mainly a measure of the electrical activity of pyramidal cortical neurons. When adjacent cortical areas have the same orientation, their voltage fields combine as a linear sum. When the orientation is opposite, such as the two sides of a sulcus, cancellation occurs and no voltage can be measured on the scalp [51]. Thus voltage fields summate in relation to the geometry of their respective field vectors (Fig. 2.6).

Due to the limited amount of electrodes that can be fixed to the scalp, spatial resolution is poor. It is not possible to extract precise localizing information of interesting brain activity. Based on visual inspection one can lateralize activity or maybe define brain lobes of interest. Research also focused on EEG source localisation using mathematical models of the bio-electrical generators and the volume conductors within which they lie. This problem is called the forward problem and consists in modeling the scalp electromagnetic fields produced by a known source configuration. Modeling this requires knowledge of the complex geometry and the different conduction properties of the cerebral tissues, skull, cerebrospinal fluid and scalp. A simple model uses a three-layer spherical head model considering the head as a series of concentric spheres, each layer corresponding to a different tissue whose conductivity is assumed to be homogeneous. The three layers of this model are skin, skull, and an inner medium encompassing all intracranial content. In case a magnetic resonance image (MRI) is available, a realistic head model can be constructed [50]. These models are based on the segmentation of the MRI. The construction of these models relies on the ability of segmentation algorithms to separate the different tissues of the head. These models offer the advantage of taking into account the complex geometry as well as the significant inter-subject variability of the conductor volume.

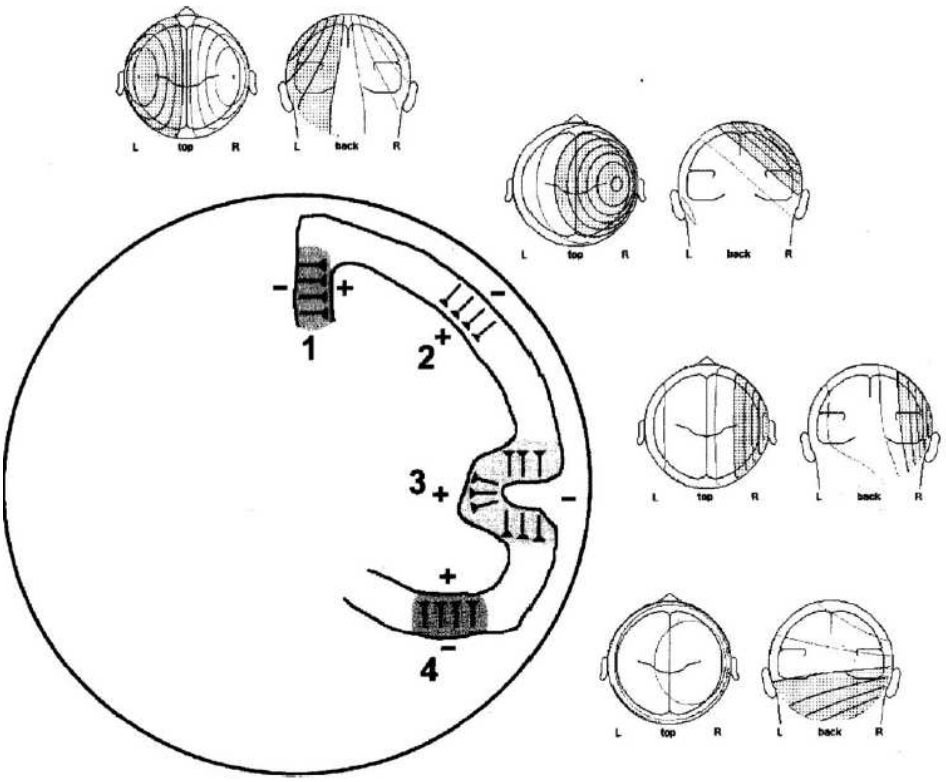

Figure 2.6: *Schematic brain cross-section representing a set of cortical EEG sources. The alignment of pyramidal cells is orthogonal to the orientation of the cortical surface. Sources 2 and 3 produce radial field, so the negative field is directly above them. Sources 1 and 4 produce tangential fields and both negative and positive voltage maxima are displaced to either side and no voltage is recorded directly above them. From [51].*

2.2.2 History of EEG

The Britisch scientist Richard Caton was the first to document electrical activity in the brain (1875) [33]. Caton had registered the existence of electric currents in the brain of monkeys and rabbits and later several other species.

Hans Berger (German, 1873-1941) is the discoverer of the human EEG [144]. In 14 reports, all with the title 'On the Electroencephalogram of man', he introduced EEG analysis of the human. His first report appeared in 1929 [72]. His studies of human EEG began in 1924 on patients with large skull bone defects (which were easy to find after WWI). He found that better quality EEG recordings could be obtained on subjects with intact skull and in the years between 1926 and 1929 he

obtained good records with alpha waves (Fig. 2.7). In the later years he published about fluctiations in consciousness, sleep recordings, effect of hypoxia, epileptic discharges, etc.



Figure 2.7: *Upper trace is the first recorded EEG of a human obtained by Hans Berger. The lower trace is a 10Hz timing signal. From [144].*

2.2.3 Practical applications of EEG

The main advantages of EEG is that it is non invasive, relatively simple to perform, relatively cheap and results are given in real time. EEG monitoring is used in several applications, mainly to detect abnormalities and changes in the function of the brain, understand motor and autonomic phenomena that mimick seizures and measure disease progress. The EEG is used routinely for diagnosis of epilepsy. It is used in anaesthesiology to assess depth of sedation [171]. Another application where the EEG is routinely used in combination with polygraphy is sleep research. A relatively new application is Brain Computer Interface (BCI). In BCI, mainly paralyzed, patients are able to control simple systems by consciously changing their brain waves.

2.3 The neonatal brain

2.3.1 Neonatal brain damage

In this thesis we measure the EEG of newborn neonates with brain damage. A major cause of neonatal brain damage is asphyxia or hypoxic-ischemic encephalopathy (HIE). Hypoxia refers to an inadequate supply of oxygen to the cells, ischemia refers to an inadequate supply of blood to the cells and encephalopathy refers to brain dysfunction. Brain injury is thought to result from the combination of hypoxia and ischemia. HIE is experienced by one to six infants per 1000 live term births [197, 44]. The underlying cause of HIE in infants is inadequate delivery of blood and oxygen to the brain. There are numerous problems during pregnancy, labor, delivery, and post-delivery that can cause HIE. If the cerebral blood flow is blocked or the blood oxygen content decreases, the affected neurons will get depleted of ATP and phosphocreatin

[100]. The brain is not able to switch to anaerobic metabolism because it does not have any long term energy stored. In the absence of biochemical energy, cells begin to lose the ability to maintain electrochemical gradients. With the loss of energy, the cell is unable to control its balance, hence there is an influx of intracellular sodium and chloride followed by water (cytotoxic edema) with an increase of extracellular potassium and excitatory neurotransmitters (e.g. glutamate) [160]. These events are accompanied by seizure activity and intracellular calcium (Ca^{2+}) accumulation, free radicals formation, that disrupt cell structure yielding permanent cell damage [37]. There are two major types of cell death, necrosis and apoptosis. Necrosis occurs when cells are exposed to extreme variance from physiological conditions which may result in damage to the plasma membrane. Due to the ultimate breakdown of the plasma membrane, the cell content is released into the extracellular fluid leading to an inflammatory response. Apoptosis is also called programmed cell death and is basically suicide of the cell. Apoptosis is a protective strategy of the human body in which cells that are damaged or pose a threat to the integrity of the organism are destroyed in a controlled, regulated fashion (in contrast to necrosis). Apoptosis does not happen instantly, it takes some time (a few hours) until the cell dies and damage to the brain is permanent. This delay between the trigger that activates apoptosis and the ultimate cell death is called the *window of intervention*. It is believed that during this time protective strategies can be done to save brain cells by interrupting apoptosis.

2.3.2 EEG monitoring of the neonate

Respiration rate, heart rate, oxygen saturation and blood pressure are all routine measures on newborns admitted to the Neonatal Intensive Care Unit (NICU). Only recently it is considered important, and possible, to continuously monitor brain function using EEG [44]. As EEG is a direct measurement of the electrical activity of the brain, it is a very sensitive indicator in real time of the functional state of the brain. The interruption of blood flow for twenty seconds results in significant changes of electrical activity [170]. Thus, as HIE has an immediate impact on this functional activity, EEG is a suitable modality for monitoring infants suffering from HIE. The severity of EEG abnormalities is often clearly correlated with immediate and longterm outcome, especially in HIE or in neonatal seizures [111]. Reliable early prediction of neurological outcome in these infants not only allows appropriate advice for parents, but may also indentify infants who may benefit from immediate neuroprotective treatment [213].

An EEG of the neonate is often done for the following indication [161]:

- assess the severity of brain dysfunction

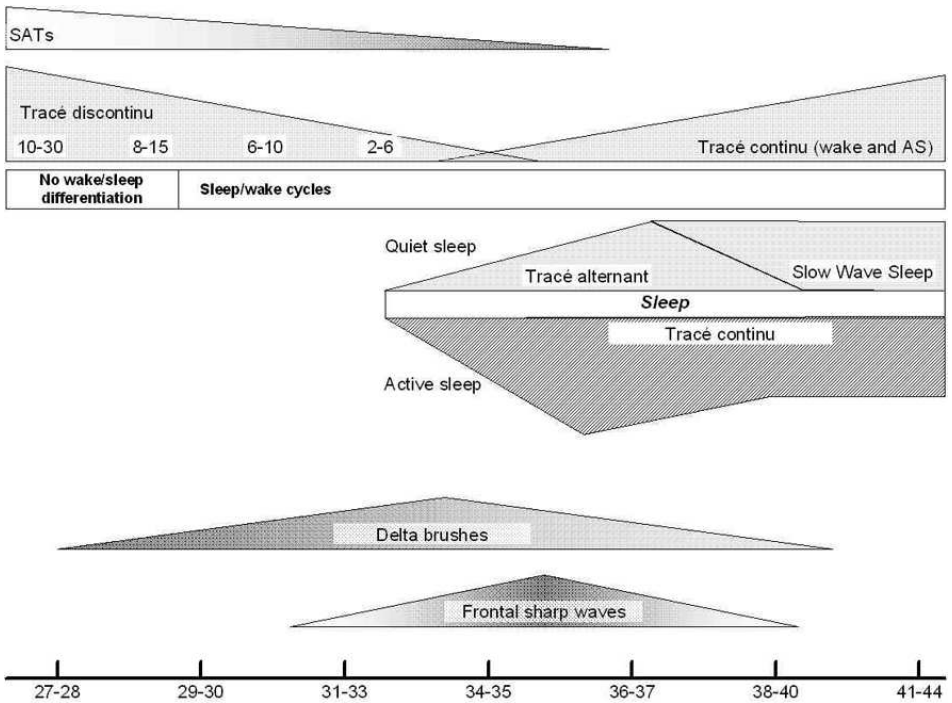

Figure 2.8: *Scheme illustrating important maturational changes in the neonatal EEG, Tracé discontinu: duration of discontinuity is given in seconds. At the bottom, conceptional age in weeks. From [161].*

- detect (sub-clinical) seizures
- assess cerebral maturation
- determine prognosis

Neonatal EEG interpretation and abnormalities

To interpret the EEG, the neurologist needs to be aware of the exact age of the neonate. Maturational changes happen fairly fast in the 25 to 48 week period of conceptional age (an overview of EEG features according to conceptional age is given in Fig. 2.8). Normal EEG patterns at one age can be abnormal only a few weeks later and vice versa. Discrepancy in age-related findings of more than 2 weeks is abnormal.

Normal neonatal EEG

Healthy full term neonates have clear sleep-wake cycles. Fig. 2.9 shows an example of the EEG of an awake healthy newborn and Fig. 2.10 of the same newborn during quiet sleep. Another type of sleep is active sleep. The morphology of active sleep is similar to that of awake EEG, but differences can be seen in the polygraphy. For instance, in the electro-oculogram (EOG), rapid eye movements (REM) can be seen during active sleep.

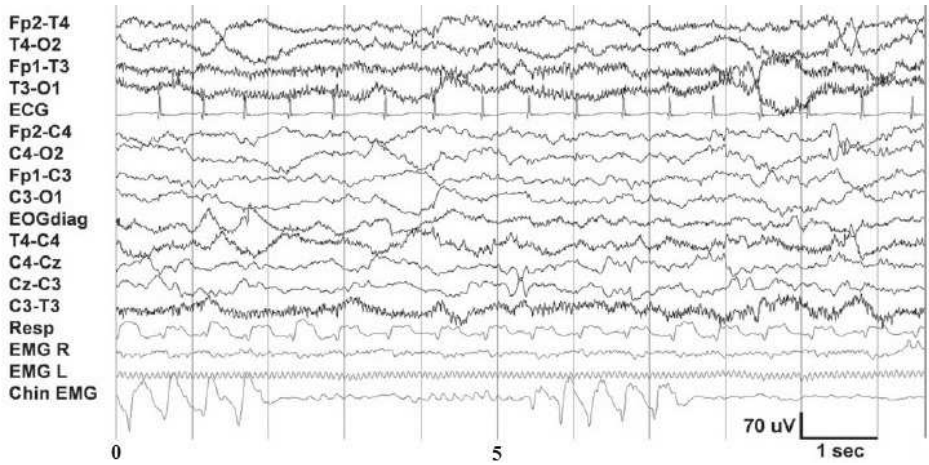

Figure 2.9: *Awake EEG at term. Shows theta and delta activity with normal voltage (20-70 μV). The faster frequencies (> 50 Hz) seen in the temporal channels are due to muscle artifacts. Chin EMG shows rhythmic artifacts produced by sucking. From [161].*

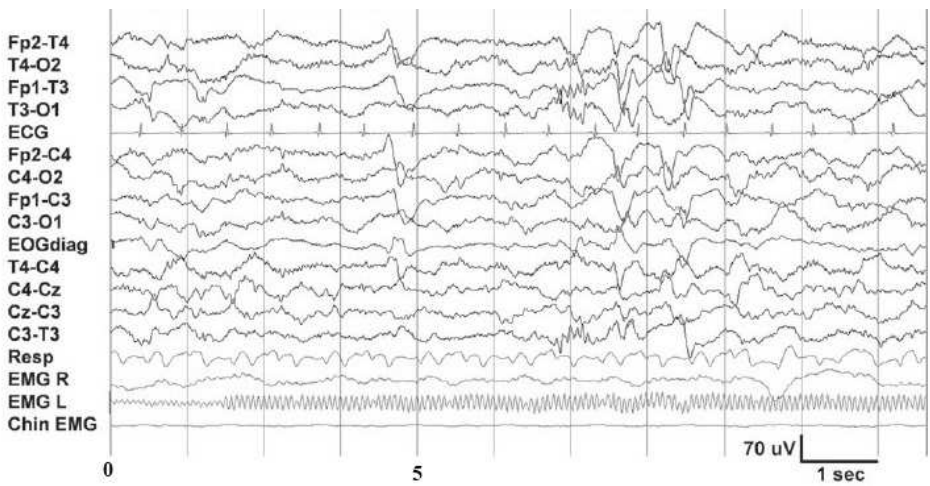

Figure 2.10: *Normal quiet sleep in the neonate in Fig. 2.9. Tracé alternant with lower voltage during 2-5 s, and higher voltage in the next 3 s. Frontal sharp waves (encoches frontales) are seen at 4 s and brush-like activity between 6 and 7 s, T3-O1. Compared to Fig. 2.9, amplitude is higher and there is less muscle activity. From [161].*

Abnormal neonatal EEG

One of the earliest abnormalities is an abnormal or absent sleep-wake-cycling [218]. Conversely, the presence of sleep wake cycling is a good prognostic sign. Voltage of the background EEG and the level of (dis)continuity of the voltage are important factors in interpretation of neonatal EEG. Abnormalities of the voltage of background EEG can be ordered in increasing severity [161]:

- discontinuous EEG (Fig. 2.11)
- burst suppression pattern (Fig. 2.12)
- continuous low voltage EEG (voltage $< 10\ \mu$V).
- isoelectric EEG (voltage $< 2\ \mu$V)

Discontinuous EEG in neonates with HIE is comparable to the tracé discontinu seen in prematures. The longer the discontinuous periods [10] and the lower the voltage ($< 10\ \mu$V), the greater the brain dysfunction and both are an indication of poor prognosis ([119, 162, 129, 192]). Burst suppression (BS) EEG is a more severe form of discontinuous EEG and typically associated with poor outcome [129, 138]. A pattern is called BS when episodes of electrical quiescence (suppression) alternate with episodes of high frequency and high amplitude electrical activity (bursts). BS-EEG shows suppression periods of more than 10 s (Voltage $< 5\ \mu$V). Bursts typically have an amplitude of over 50 μV with abnormal sharper content and less low frequency activity. Continuous low voltage and isoelectric EEG are generally associated with major sequelae or death [168].

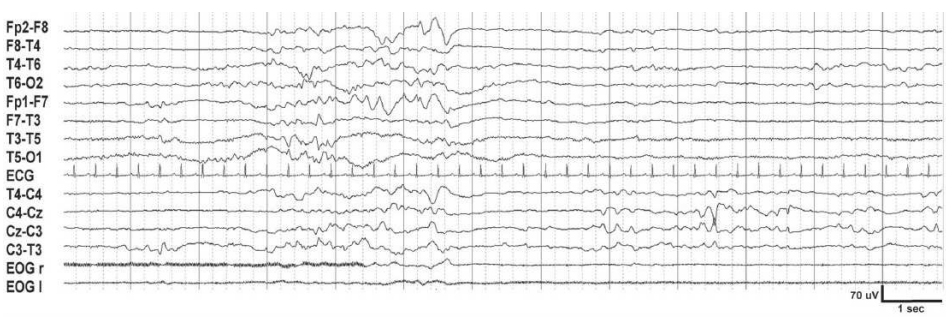

Figure 2.11: *Tracé discontinu in a neonate with moderately severe HIE. Background activity is of low voltage ($< 20\ \mu V$). The discontinuous periods, with a mean voltage of 10 μV, are interrupted by bursts of EEG activity of 2-3 s duration. From [161].*

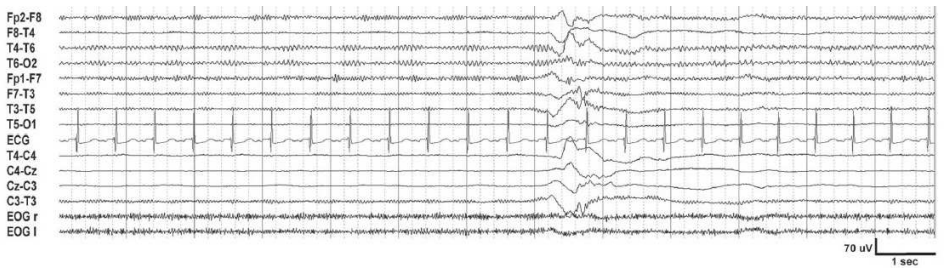

Figure 2.12: *Burst suppression (BS) pattern in severe birth asphyxia. Severely suppressed background activity (< 5 μV) with intermittent bursts of 50 μV. As opposed to tracé discontinu (Fig. 2.11), no EEG activity is discernible during the discontinuous periods. From [161].*

EEG is accurate to predict normal and severe neurological disablities but the sensibility to predict moderate or mild deficits is low [168, 118, 138]. Long or serial EEG recordings improve sensibility for defining prognosis. For instance, good outcome can be associated to infants with poor background activity that recover within 12 h after birth [168]. This uncertainty on the prognosis of mildly abnormal EEG's might be partly due to lumping together of various etiological groups in the same study [218]. In those cases, the extent of the structural lesion on MRI is a better predictor [130]. Problematic for MRI is that it gives structural information about the brain and it takes at least 3 days before the structurial damage becomes visible. It is known that neuroprotective therapies must be administered to newborn neonates with HIE within the first few hours of birth (to interupt apoptosis) and that the EEG can identify those neonates that are most suitable for treatment [107] while MRI cannot. Therefore, MRI is not suitable to obtain information within hours of delivery for early diagnosis, intervention and prognosis of infants suffering from HIE, even with the use of diffusion weighted imaging [194, 175, 176].

2.3.3 Neonatal seizures

A seizure is a paroxysmal depolarisation of a group of neurons. When clinical signs, like abnormal motor activity, can be observed it is called a *clinical* seizure. For many years, neonatal seizures (example Fig. 2.13) are known to be common in neurologically abnormal neonates [82, 135, 29, 38, 219, 17], are associated with neurodevelopmental deficits [38, 32, 28, 114, 182, 18] and have been recognized as an important sign of encephalopathy [215, 114, 127]. Seizures may disrupt the processes of cell division, migration, myelination, stabilization of synapses, ... each of which contributes to degrees of neurologic sequelae [181]. It has been shown that seizures are not the benign manifestation of existing brain injury [217, 88].

Therefore early identification of children at risk for seizures is a very important factor for predicting outcome [118, 28, 54, 87, 152, 101]. It was suggested that EEG background is more important to determine prognosis than epileptic activity [138] as there is controversy wether neonatal seizures cause brain injury [181, 57]. It has been shown that the etiology of neonatal seizures is an important factor for general prognosis [200]. Nevertheless, when the clinical picture is analyzed in conjunction with neurophysiological aspects, such as abnormal background activity and the presence of electrographic seizures, a more accurate outcome will be predicted [114, 38, 89]. Thus both seizures and background EEG are of great importance.

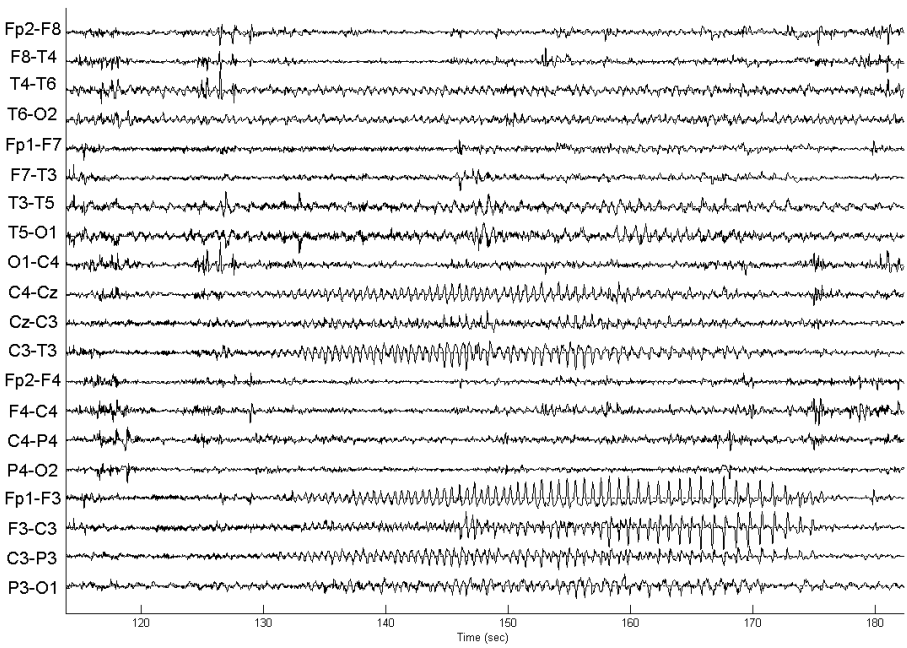

Figure 2.13: *Example of a typical neonatal seizure. The seizure is predominantly present on channels C4-Cz, C3-T3, Fp1-F3 and C3-P3.*

Visual detection of seizures is based on clinical criteria [133, 199] and electrographic confirmation is required [136, 180]. The EEG, rather than clinical signs, is the best diagnostic method by which a seizure onset and offset can be assigned [125]. The majority of the seizures occurring in neonates admitted to the NICU are subclinical, being detected only by EEG monitoring [82, 140]. The reason for that is that cerebral cortical organisation, synaptogenesis, and myelination of cortical efferent pathways are poorly developed in neonates, leading to weakly propagated, fragmentary seizures [57]. It is adviced to only choose pharmacologic treatment (typically antiepileptic drugs) in case of electrographic seizures to avoid misclassification of nonepileptic paroxysmal behaviour [181].

2.3.4 Neonatal EEG at the bedside

The problem for application of bedside EEG analysis in the NICU is that it requires particular skills which are not always present round the clock. Even if those skills are present it is laborsome to manually analyse many hours of EEG. The lack of time and skill are the main reasons why EEG is not widely used in the NICU although it is the only modality to assess electrical brain function at the bedside. It is believed that EEG can and should be available in the NICU [13, 55]. Hence there is scope for an automated system that reliably analyses the EEG and detects neonatal seizures [209].

The current most widely accepted technique for use in clinical practice is a single channel amplitude integrated EEG (aEEG) or Cerebral Function Monitor (CFM) [126, 81]. CFM is a method for continuous monitoring of brain function that filters and compresses EEG so that long-term changes and trends in background activity can be found through simple pattern recoginition [83, 79, 81]. The CFM algorithm consists of five main steps:

- band-pass filtering
- rectifying
- amplitude compression
- smoothing filtering
- down-sampling to 10Hz

The band-pass filter as defined by Prior and Maynard [169] together with a practical implementation of the filter is shown in Fig. 2.14.

The CFM signal gives a continuous trend recording of the EEG amplitude in a time compressed form (Fig. 2.15). Originally, CFM was designed for monitoring of adult patients during anaesthesia and in intensive care after cardiac arrest, during status epilepticus, and after heart surgery [44]. For the newborn, CFM can provide information about the background EEG and generalized seizure activity [203]. Especially in long term recordings, the CFM signal is due to its compressed form very useful in evaluation of changes in background pattern over time (e.g. sleep wake cycling [151]) and effect of medication [78]. Despite its intrinsic value for amplitude monitoring, CFM has many disadvantages and pitfalls, especially for unexperienced users [173]. Focal, low amplitude and short periods of seizure discharges can be missed by CFM leading to underestimation of the number of seizures and thus undertreatment [203]. Some artifacts (like ECG spikes and respiration) may present themselves in the CFM trace as seizures and may lead to overestimation of the number of seizures and thus overtreatment. In the literature,

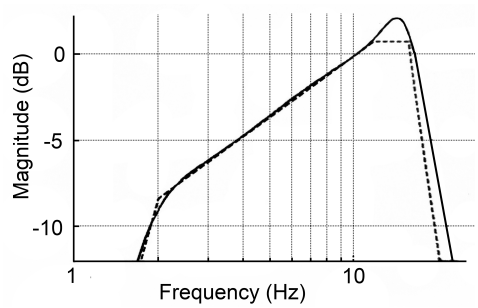

Figure 2.14: *Frequency respons of the CFM band-pass filter defined by Prior and Maynard [169] (dashed) and the frequency response of a typical implementation (solid).*

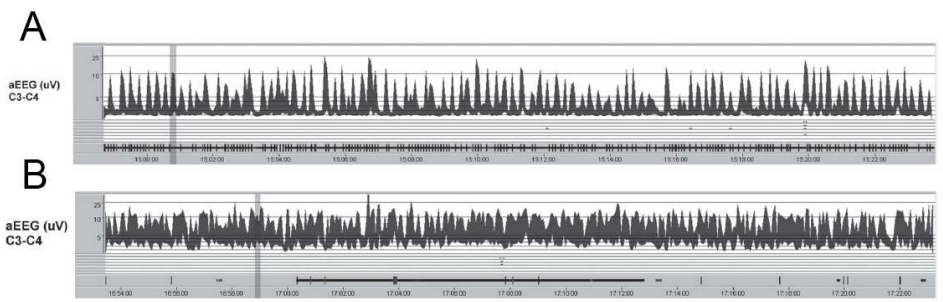

Figure 2.15: *Two examples of typical CFM traces. A: CFM trend of 30 min shows BS and absent variability. B: CFM trend covering 30 min of a patient with tracé discontinu, absence of sleep wake cycling. From [161].*

it is recommended to use CFM as a monitoring device complementary to standard EEG [80]. Standard EEG is needed whenever there is any doubt about the classification of the CFM (e.g. when seizures are suspected) [203].

2.3.5 Artifacts in the neonatal EEG

EEG potentials are extremely small (10-100 μV). Thus sensitive amplifiers are needed to be able to record these small potentials, which makes them susceptible for artifacts. Unfortunately, there are many other sources of electrical activity in the human body and monitoring environment. All electrical sources that are not

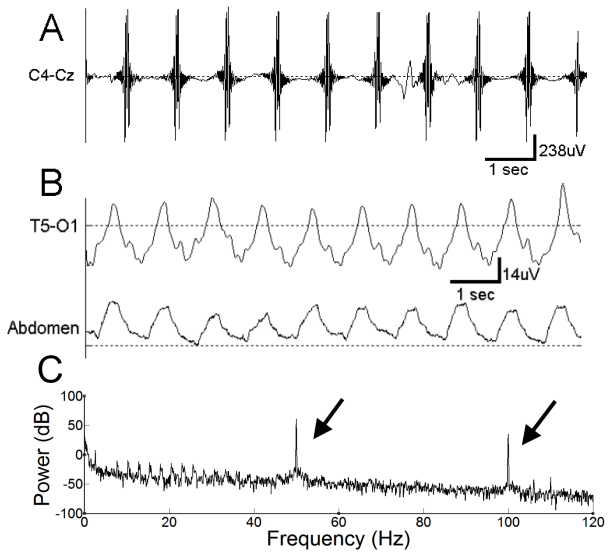

Figure 2.16: *Examples of common non-biological artifacts in the NICU. A: Incubator artifact due to heating of the bed. B: Mechanical ventilation artifact, as shown by the high correlation with a sensor on the abdomen. C: Frequency plot of an EEG signal with 50 Hz powerline and 100Hz fluorescent light artifacts (peaks in the frequency content marked by arrows).*

generated by the brain are called artifacts. There are artifacts of biological and non-biological origin.

non-biological artifacts

In the NICU typical examples are incubator artifacts (heating of the bed), 50 Hz power line artifacts, 100 Hz fluorescent light artifacts or electrical malfunction of the recording system itself (e.g. detached electrodes). Most non-biological artifacts are relatively easy to recognize as they often have morphological characteristics that cannot be generated by biological tissue. Fig. 2.16 gives an overview of some of these artifacts.

biological artifacts

Artifacts are called biological when they are caused by other parts in the body than the brain. We can distinguish artifacts caused by

- movements of the head, body or scalp, e.g. during tremor or respiration,
- moving electrical potentials within the body, e.g. heart muscle contraction,
- changes in skin resistance, e.g. due to sweating,
- active muscle cells, e.g. during frowning, chewing,
- movements of the eye ball, e.g. during eye movements and blinking.

Figures 2.17, 2.18 and 2.19 give an overview of some of the most common biological artifacts in neonatal EEG. Most of these artifacts can be recognized in the EEG based on additional polygraphy signals like ECG, respiration, movement sensors, etc. Polysomnography signals help the neurophysiologist in recognizing the artifacts and are the golden standard while recording neonatal EEG.

2.3.6 Treatment options

Prolonged or poorly controlled neonatal seizures have been associated with worse outcome than infrequent or readily controlled seizures [114, 128]. The most widely used treatment for seizure control is pharmacological by giving anticonvulsants (like phenobarbitone, clonazepam, ...) until the seizures are suppressed. The amount of anticonvulsants administered should be limited as many cause respiratory depression and impair myocardial function [57].

A relatively new possibility for treatment of patients with HIE is hypothermia. With hypothermia, body temperature of the neonate is reduced either through whole body cooling or just brain cooling. The protective mechanism of brain hypothermia is not totally elucidated, it seems that it interrupts the biochemical cascades leading to delayed cerebral damage (apoptosis). Researchers are proceeding with caution in applying hypothermia, due to concern of possible side effects: cardiac arrhythmias [148], blood viscosity effects [207, 25], pancreatic disorders [139], hypoglycemia [96], sepsis [53, 31, 191]. Despite these possible side effects, results are promising and favourable [37, 5, 71, 67, 185].

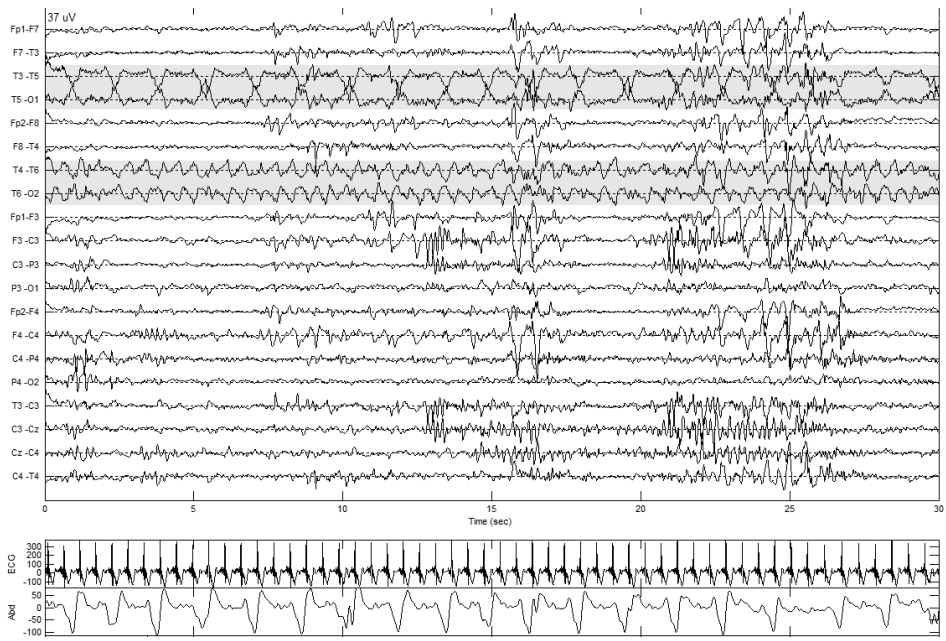

Figure 2.17: *Illustration of a respiration and ECG pulsation artifact present in a 30 s long EEG signal. The respiration artifact can be seen on channels T3-T5, T5-O1 (marked in grey) and be verified by comparison with a sensor on the abdomen ('Abs' signal below EEG). The ECG pulsation artifact can be seen on channels T4-T6, T6-O2 (marked in grey). The repetition frequency of the oscillation in the EEG is the same as the heart rate which can be verified by comparison with the ECG sensor ('ECG' signal below EEG).*

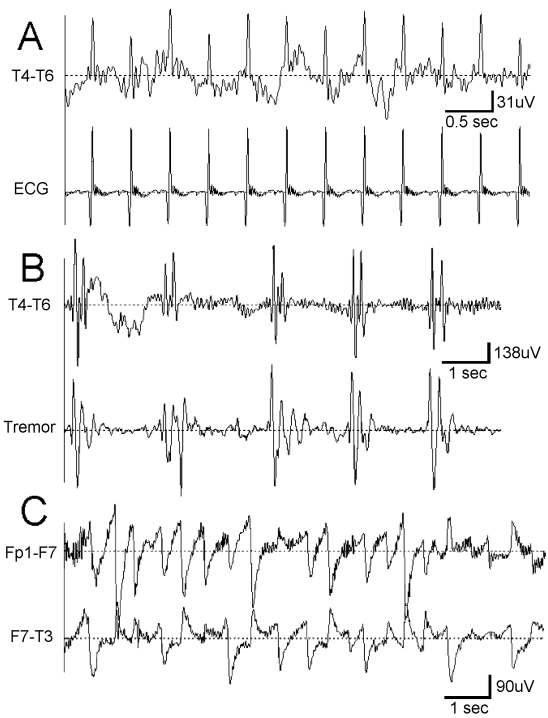

Figure 2.18: *Examples of typical neonatal EEG artifacts of biological origin. A: ECG spike artifact (correlation with ECG sensor), B: tremor artifact (correlation with movement sensor), C: pathological fast eye movements (nystagmus) present on the frontal EEG channels.*

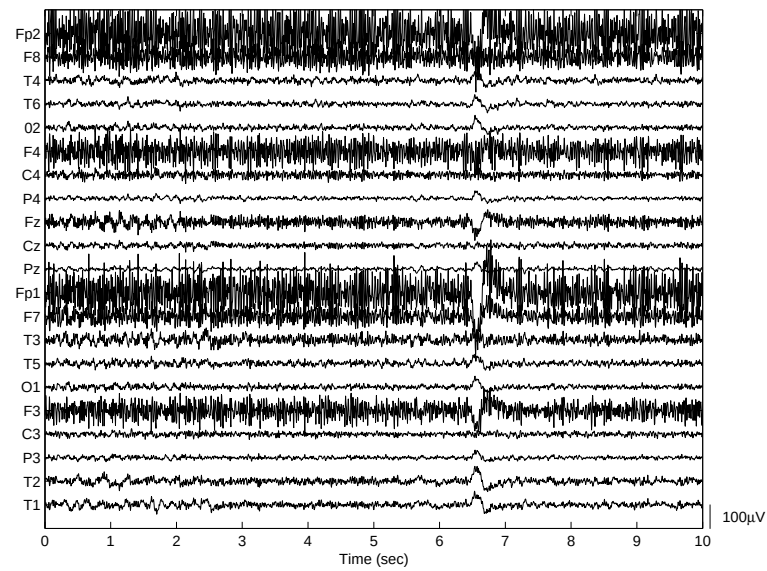

Figure 2.19: *EEG recording contaminated with muscle artifact, strongly visible on the frontal electrodes. An average reference montage was used.*

Chapter 3

Background: Mathematical techniques

In this chapter an introduction is given to the mathematical background used throughout this thesis. A wide range of mathematical techniques are discussed. The introduction provides some basic definitions. Then, the most important matrix/tensor decompositions are discussed. Afterwards, frequency and time-frequency analysis is introduced. Finally, techniques to analyse the energy and entropy of a signal are discussed.

3.1 Introduction

Stacking data

A 1 dimensional signal with J number of elements can be stored in a vector $\mathbf{s} \in \mathbb{R}^{1\times J}$. EEG is a 2 dimensional signal with dimensions time and channel location. Such a 2 dimensional signal can be stored in a matrix $\mathbf{X} \in \mathbb{R}^{I\times J}$. The channels of the EEG can be stored in the rows of matrix $\mathbf{X}$, the time samples of each channel in the columns. Data can be more than 2 dimensional. In that case data is stored in a higher-order tensor $\mathcal{A} \in \mathbb{R}^{I_1\times I_2\times \ldots \times I_n}$. In this thesis data structures of maximum 3 dimensions or third-order tensors will be used.

For tensors, a mode-n vector of a tensor $\mathcal{A} \in \mathbb{R}^{I_1\times I_2\times I_3}$ is the I_n-dimensional vector obtained from $\mathcal{A}$ by varying the index i_n and keeping the other indices fixed [102]. Alternatively, the mode-n vectors of a third-order tensor can be called columns, rows and tubes as illustrated in Fig. 3.1. By fixing only 1 mode, a matrix or a tensor slice is obtained, as shown in Fig. 3.2.

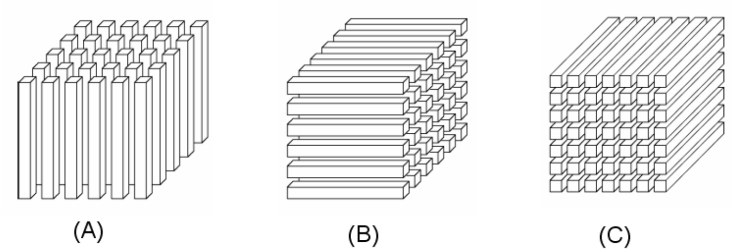

Figure 3.1: *(A) Columns, (B) rows and (C) tubes in a third-order tensor.*

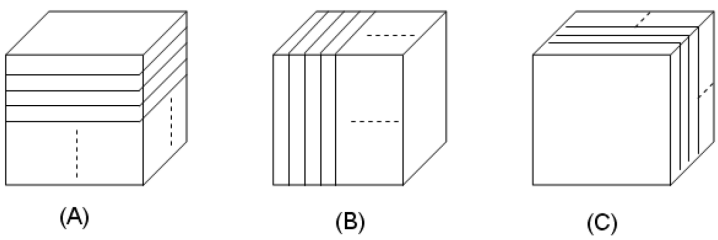

Figure 3.2: *(A) Horizontal, (B) vertical and (C) frontal slices.*

3.2 Rank of a matrix and the Singular Value Decomposition (SVD)

Rank of a matrix

Consider a matrix $\mathbf{X} \in \mathbb{R}^{I \times J}$. The row rank of matrix $\mathbf{X}$ is the number of linearly independent rows and the column rank is the number of linearly independent columns. For every matrix the row rank is equal to the column rank and is called *the* rank of the matrix [220]. The minimum rank for a matrix is 1. The rank of a matrix $\in \mathbb{R}^{I \times J}$ is at most $min(I, J)$. A matrix that has a rank as large as possible is said to have full rank; otherwise, the matrix is rank deficient.

SVD

Consider a matrix $\mathbf{X} \in \mathbb{R}^{I \times J}$, the SVD is defined as

$$\mathbf{U} \cdot \Sigma \cdot \mathbf{V}^T \tag{3.1}$$

with $\mathbf{U} \in \mathbb{R}^{I \times I}$ and $\mathbf{V} \in \mathbb{R}^{J \times J}$ orthogonal matrices and Σ a non-negative diagonal matrix. The elements on the diagonal of Σ are called the singular values σ_{ii}. These singular values are sorted in decreasing order. The column vectors of matrix $\mathbf{U}$ are called the left eigenvectors, the column vectors of matrix $\mathbf{V}$ are called the right eigenvectors.

The SVD also enables us to write $\mathbf{X}$ as a sum of rank-1 terms:

$$\mathbf{X} = \sigma_1 \mathbf{u}_1 \mathbf{v}_1^T + \ldots + \sigma_R \mathbf{u}_R \mathbf{v}_\mathbf{R}^\mathbf{T} \tag{3.2}$$

with $\mathbf{u}_j$ and $\mathbf{v}_j$ the jth column of $\mathbf{U}$ and $\mathbf{V}$ respectively. We can also write the individual elements of $\mathbf{X}$ as:

$$x_{ij} = \sum_{r=1}^{R} u_{ir} \sigma_{rr} v_{jr} \tag{3.3}$$

This SVD decomposition, restricted to R components, is visualised in Fig. 3.3.

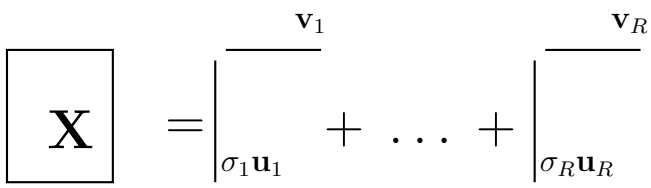

Figure 3.3: *Singular Value Decomposition of* $\boldsymbol{X}$ *restricted to* R *components.*

Theorem of Eckart-Young

Define the truncated SVD as the SVD restricted to the first ρ components. Let the rank-ρ matrix $\mathbf{Y}$ with $\rho \leqslant R$ be given by the truncated SVD of $\mathbf{X}$ (of rank R), then $\mathbf{Y}$ is the best rank-ρ approximation of $\mathbf{X}$ in the least-squares sense, *i.e.*, $||\mathbf{X} - \mathbf{Y}||^2$ is minimal [52].

3.3 Principal Component Analysis (PCA)

PCA is mathematically defined as an orthogonal linear transformation that transforms the data to a new coordinate system such that the greatest variance by any projection of the data lies along along the first coordinate (called the first principal component), the second greatest variance on the second coordinate, and so on (example see Fig. 3.4) [97, 159, 52].

PCA [159, 52] of a matrix $\mathbf{X} \in \mathbb{R}^{I \times J}$ with rank R computes orthogonal matrices $\mathbf{A} \in \mathbb{R}^{I \times R}$ and $\mathbf{B} \in \mathbb{R}^{J \times R}$ as

$$\mathbf{X} = \mathbf{A}\mathbf{B}^T \text{ for which } \|\mathbf{X} - \mathbf{A}\mathbf{B}^T\|^2 \text{ is minimal.} \tag{3.4}$$

The columns of $\mathbf{A} \in \mathbb{R}^{I \times R}$ are called the factors and the columns of $\mathbf{B} \in \mathbb{R}^{J \times R}$ the loadings. The factors are linear combinations of the measurements and are uncorrelated. Alternatively, we can write:

$$x_{ij} = \sum_{r=1}^{R} a_{ir} b_{jr}. \tag{3.5}$$

It has been derived that a PCA solution can be obtained as the truncated SVD of $\mathbf{X}$. However, a PCA solution is not unique [216]:

$$\mathbf{A} \cdot \mathbf{B}^T = (\mathbf{A}\mathbf{Q}) \cdot (\mathbf{Q}^T\mathbf{B}^T) \text{ for } \mathbf{Q} \text{ with } \mathbf{Q}\mathbf{Q}^T = \mathbf{Q}^T\mathbf{Q} = \mathbf{I}_R \tag{3.6}$$

gives an equivalent solution of the minimisation problem (3.4). So every orthogonal rotation $\mathbf{Q}$ gives a different basis for the factor space spanned by the columns of $\mathbf{A}$. If the rotation $\mathbf{Q}$ yields a simple structure in the loadings matrix $(\mathbf{Q}^T\mathbf{B}^T)$, then the factors are easier to interpret. PCA and SVD are closely related: they both provide the decomposition in orthogonal components.

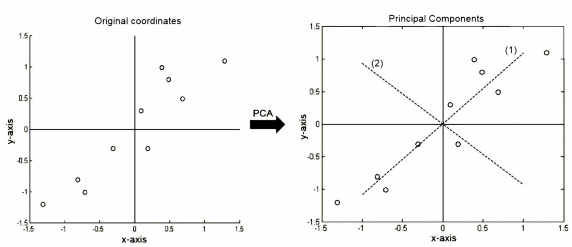

Figure 3.4: *Illustration of Principal Component Analysis (PCA). The principal components (1) and (2) form an orthogonal and uncorrelated basis.*

3.4 Blind Source Separation (BSS)

3.4.1 The cocktail party problem

Blind Source Separation refers to methods that allow the separation of a set of source signals from a set of mixed signals without information about the nature of the source signals. This problem can be illustrated with the cocktail party problem

(Fig. 3.5). Imagine three people are talking to each other in a room producing the source signals $s(t)$. Several microphones, located at different places in the room, are simultaneously recording the conversations (signals $x(t)$). Each microphone measures a linear mixture of the conversations. This mixture can be represented by mixing matrix $\mathbf{A}$. Thus, the basic linear statistical model is:

$$\mathbf{X} = \mathbf{A} \cdot \mathbf{S} \tag{3.7}$$

where $\mathbf{X}$ is called the observation matrix and $\mathbf{S}$ the source matrix. We are not really interested in the observation matrix, we prefer to hear the individual conversations. As we have no information about the individual conversations, we will need to estimate them. The objective of BSS is to find an unmixing matrix $\mathbf{W}$ allowing to recover the original source signals:

$$\mathbf{Y} = \mathbf{W} \cdot \mathbf{X} \tag{3.8}$$

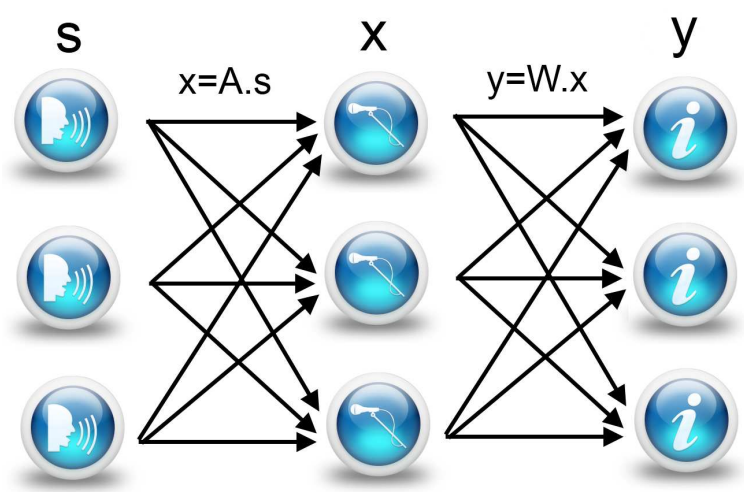

Figure 3.5: *Illustration of the cocktail party problem. The signals measured at the microphones consist of a linear mixture of the different conversations. The objective of BSS is to recover the original source signals.*

3.4.2 Independent Component Analysis (ICA)

In order to solve the BSS problem, the hypothesis that the sources are mutually statistically independent is often made [20]. Statistically independency between sources is a stronger requirement than the uncorrelatedness between sources. This can be illustrated using a simple example. Imagine X is the value of an honest

dice after a first throw and Y is the value after a second throw. These variables are independent and have the same distribution: $cov(X,Y) = 0$ and $var(X) = var(Y)$. Let us introduce 2 new variables, namely the variables $(X+Y)$ and $(X-Y)$. These new variables are uncorrelated:

$$\begin{aligned} cov(X+Y, X-Y) &= cov(X,X) + cov(X,-Y) \\ &\quad + cov(Y,X) + cov(Y,-Y) \\ &= var(X) - cov(X,Y) \\ &\quad + cov(Y,X) - var(Y) \\ &= 0 \end{aligned}$$

But they are not independent. To be independent $P(X+Y|X-Y) = P(X+Y)$, with P the probability. Imagine:

$$P(X+Y=12) = \frac{1}{36}$$

But:

$$\begin{aligned} P(X+Y=12|X-Y=5) &= P(X+Y=12|X=6,Y=1) \\ &= 0 \\ &\neq \frac{1}{36} \end{aligned}$$

Thus $(X+Y)$ and $(X-Y)$ are uncorrelated, but they are not independent.

Statistical independence can be obtained by estimating components that are maximally non-gaussian. According to the central limit theorem (CLT) we know that any mixture of two source signals will be more gaussian than the original source signals. Thus to recover the original sources from the mixture, it makes sense to strive to maximal non-gaussian sources. With this hypothesis, sources with gaussian distributions cannot be estimated [39]. It is possible to solve the ICA problem using only higher-order statistics, an overview of practical algorithms is given in [92, 41].

ICA applied to brain signals

Because of volume conduction through cerebrospinal (CSF) fluid, skull and scalp, EEG signals collected from the scalp are a mixture of neuronal and artifactual activities from multiple brain or extra-brain sources (Fig. 3.6). All these sources

have overlapping scalp projections, time courses and spectra. Therefore their distinctive features cannot be separated by simple averaging or spectral filtering and more advanced techniques like ICA need to be used.

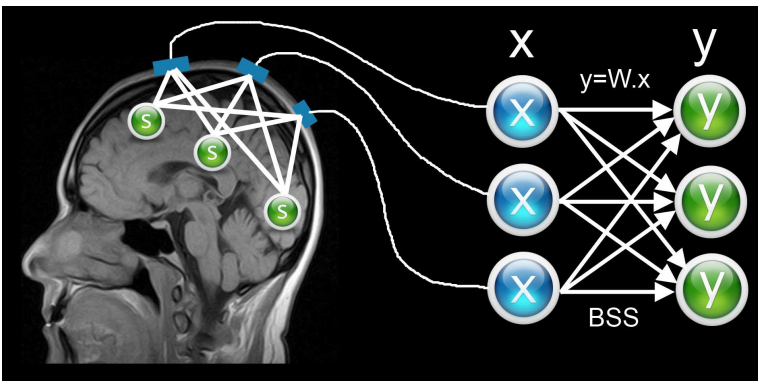

Figure 3.6: *Illustration of the application of Blind Source Separation (BSS) to EEG. The EEG measures a mixture of the brain sources at the scalp. BSS estimates demixing matrix* $\boldsymbol{W}$ *to reconstruct the original sources.*

Several assumptions need to be fullfilled before ICA can be applied to EEG [206, 94].

1. the summation of different source signals at the sensors is linear,
2. the propagation delays in the mixing medium are negligible,
3. the sources are statistically independent,
4. the number of independent sources is the same or less as the number of sensors.
5. the mixing matrix is stationary

The first assumption is valid as the EEG mixing process is linear, although the process generating it may be highly nonlinear. The second assumption is assured by the biophysics of volume conduction at EEG frequencies [146]. The third assumption of independence is compatible with physiological models for the generation of EEG [177]. It is the assumption that EEG dynamics can be modelled by weakly linked and therefore statistical independent brain processes. Recent findings about the presence of phase synchrony as an explanation of how brain areas interact might weaken this third assumption [154]. But for neonates, phase synchrony is not an issue an the third assumption is valid. Assumption four is questionable, since we don't know the number of statistically independent sources.

Through simulations [141] it was proven that when training data consists of fewer large source components than channels and many more additional small source components, the large components are accurately separated. In actual EEG data, a similar situation can be expected. Assumption five is met as the assumption of stationary mixing can be interpreted as the fixed biophysical structure of the brain itself whilst the sources distributed within this structure change their intensity over time [94]. Nevertheless, there are types of EEG sources, such as sleep spindle activity and epileptic seizures, that are known to spread and migrate across brain regions and thus have no stationary localization [150]. Two main approaches to ICA have been proposed to date [225]. The independent components can be extracted jointly or simultaneously [36, 34, 21] and on the other hand one after another [48]. It is generally acknowledged that due to error accumulation throughout successive deflation stages that joint algorithms outperform deflationary algorithms but at a higher computational load.

fastICA / robustICA

FastICA is described as a computationally efficient method for performing the estimation of ICA [92] and is popular in neuroscience [91]. It uses a so-called fixed-point iteration scheme that has been proven to be 10-100 times faster than conventional gradient descent methods. The sources are extracted one-by-one based on their kurtosis to make the distributions of the sources as non-gaussian as possible. RobustICA is the same as FastICA but with a small optimization, as described in [225].

Second Order Blind Identification (SOBI)

SOBI [9] uses second order statistics to decompose the measurements and is employed in numerous EEG studies (e.g., [198, 210]). It is based on a joint diagonalization of correlation matrices. SOBI is most appropriate for sources that are individually correlated in time, but mutually uncorrelated. SOBI considers the relationship between component values at different time lags and insists that these values be decorrelated as much as possible. Thus, SOBI uses correlations across times in performing the signal separation. This means that SOBI can isolate highly temporally correlated sources, something that most ICA algorithms cannot do [98]. Furthermore, it exploits non-stationarity, which is typical for EEG data. In a recent study of Klemm et al. [104], SOBI proved to be among the best methods for separating EEG data.

3.5 Canonical / Parallel factor Analysis (CPA)

The trilinear Candecomp [22], also known as Parallel Factor Analysis (Parafac) [77, 110, 193], or referred to as CPA (**C**andecomp/**P**arafac Analysis) is a generalisation

of the SVD to third order [85, 84, 23].
It is defined for a three-way array $\mathcal{X} \in \mathbb{R}^{I \times J \times K}$ as:

$$x_{ijk} = \sum_{r=1}^{R} a_{ir} b_{jr} c_{kr} + e_{ijk} \tag{3.9}$$

where R is the number of components used in CPA and e_{ijk} are the residuals containing the unexplained variation. A pictorial representation of CPA is given in Fig. 3.7. CPA is a trilinear model: fixing the parameters in two modes, x_{ijk} is expressed as a linear function of the remaining parameters. Although the definition can be seen as a generalisation of the SVD, its properties cannot. The vectors in the different modes are not necessarily orthogonal, the different components are not ordered and computing CPA with different number of rank-one terms will in general give different sets of rank-one terms.

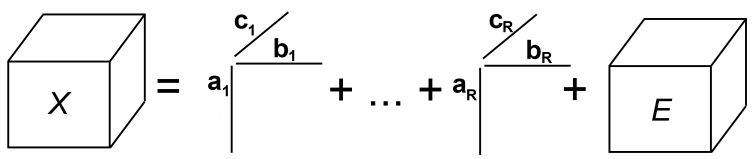

Figure 3.7: *Pictorial representation of the CP decomposition of a 3-dimensional tensor with R atoms.*

The CP decomposition was originally computed by means of an Alternating Least Squares (ALS) algorithm [193]. This means that the least-squares cost function

$$f(\mathbf{A}, \mathbf{B}, \mathbf{C}) = \left\| X - \sum_{r=1}^{R} \mathbf{a_r} \circ \mathbf{b_r} \circ \mathbf{c_r} \right\|^2 \tag{3.10}$$

is minimized by means of alternating updates of one of its matrix arguments, keeping the other two matrices fixed. Because the CP decomposition is a multilinear decomposition, each update just amounts to solving a classical linear least-squares problem [193].

Applications of CPA.

Since 1970, CPA has slowly found its way in various disciplines such as Chemometrics and food technology [193], exploratory data analysis [110], wireless communications and array processing [190, 189], blind source separation [35, 113, 59], web link analysis [6]. Also neuroscience provided multi-way datasets and neuroscientists quickly discovered CPA for analysing them [137, 60, 56].

3.6 Fourier transform (FT)

In EEG analysis many EEG phenomena are described based on their frequency content (e.g. alfa waves). The most well known technique to analyse the frequency content of a time domain signal like EEG is the Fourier transform. The Fourier transform describes the original time domain signal $x(t)$ as an integration of oscillatory functions (sinusoids) of frequency f.

$$X(f) = \int_{-\infty}^{+\infty} x(t)e^{-i2\pi ft}dt \tag{3.11}$$

$X(f)$ is then the frequency domain representation of the time domain signal $x(t)$. On discrete sampled signals the formula becomes

$$\mathbf{X}(\mathbf{f}) = \sum_{n=0}^{N-1} x(n)e^{-i2\pi kn/N}, k = 0, 1, ..., N-1 \tag{3.12}$$

where n is the sample index, N is the number of samples and k is the index in the Fourier transform.

The most important limitation of Fourier analysis is that it can only describe the time domain signal with fixed frequency basis elements $e^{-i2\pi ft}$ with time support from $-\infty$ to $+\infty$. This has 2 important consequences (illustrated in Fig. 3.9). First of all, Fourier analysis on finite-length signals leads to spectral leakage in the frequency domain. The use of a finite-length time window corresponds to a multiplication of the time domain signal with a rectangular window. Multiplication in the time domain corresponds to a convolution in the frequency domain. The frequency response of a rectangular window is the sinc function (Fig. 3.8).

$$sinc(x) = \frac{sin(x)}{x} \tag{3.13}$$

Thus the finite-length time window leads to a convolution of the original spectrum with a sinc function. As the sinc function has a main lobe and side lobes, it appears as if some energy has leaked out of the original signal spectrum into other frequencies. This effect is illustrated in Fig. 3.9A. In this figure the Fourier transform of a pure sine wave is shown. One would expect the spectrum to be an impulse at the frequency of the sine wave and zero everywhere else. Due to the convolution of the spectrum with the sinc function, this is not the case and spectral leaking can be observed.

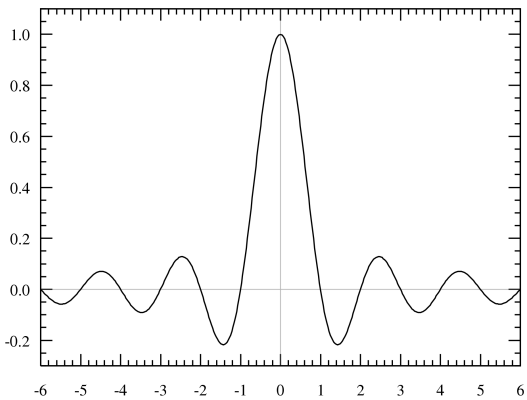

Figure 3.8: *Illustration of the sinc function. The sinc function is the Fourier transform of a rectangular window. The main lobe and side lobes lead to the spectral leaking observed in Fig. 3.9.*

But the most important drawback of Fourier analysis is that instantaneous frequency components can not be modelled by the Fourier transform. The Fourier transform expects a stationary signal. A stationary signal is a signal with constant (or periodic) frequency content during the whole window of analysis. EEG is a highly non-stationary signal as the frequency content of the EEG is constantly changing in time. Fig. 3.9B shows the effect of a Fourier analysis on a sine wave with a small perturbation in the time signal. From the frequency content it can be seen that the short perturbations lead to spurious frequency components to simulate the non-stationarities in the data.

The conclusion is that one must be careful when applying the Fourier transform on highly non-stationary signals such as EEG and be aware of its limitations. To analyse the frequency content of EEG we have to use techniques that are able to deal with the non-stationarity. The Fourier transform contains no temporal information. To circumvent this problem, the Fourier transform can be performed on successive EEG segments defined by a windowing function which is also called the Short Time Fourier Transform (STFT). This procedure allows the extraction of both time and frequency domain information. The size of the window width is critical and a compromise must be made between time and frequency resolution (Fig. 3.10) according to Heisenbergs Uncertainty Principle [106]. This principle states that a function cannot be arbitrarily defined both in time and frequency and that the product of both variances is constant.

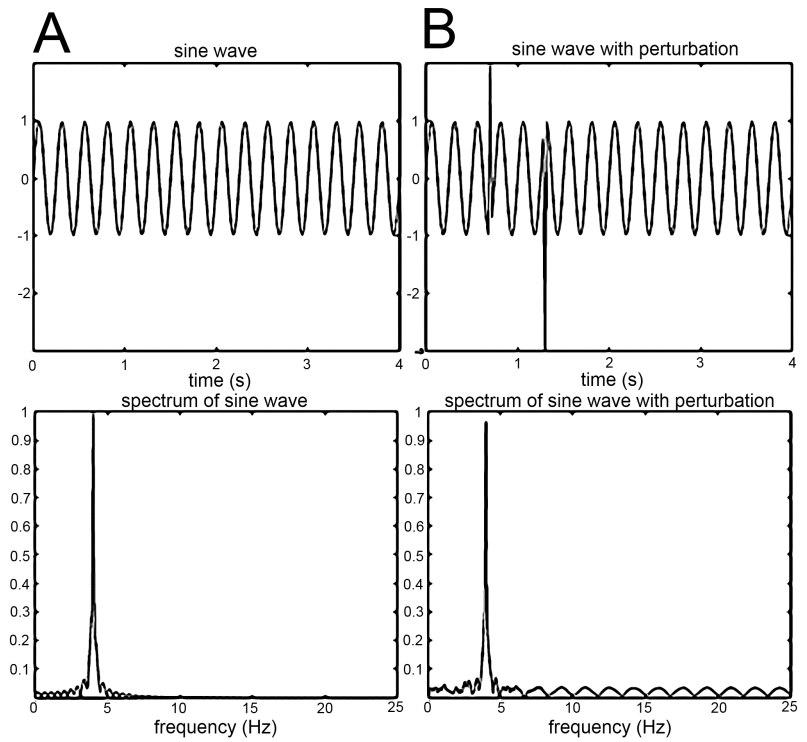

Figure 3.9: *Limitations of the Fourier transform. A: The use of finite-length time windows leads to spectral leaking. B: Small perturbations in the time signal lead to spurious components in the spectrum.*

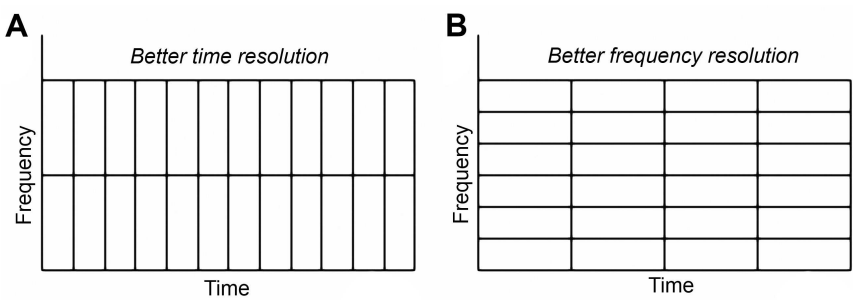

Figure 3.10: *Illustration of the effect of the window-size of the STFT. Fig. 3.10A has a better time resolution while Fig. 3.10B has better frequency resolution.*

3.7 Wavelet transform (WT)

In EEG spectrum analysis we are not just interested in which frequency components are present in the EEG. We also want to know at what time instance each frequency is present. Thus we need a time-frequency representation of the time signal very similar to a stave in music on which the notes to be played are well defined in time and frequency. STFT can be used to segment the EEG in pseudo-stationary segments to obtain a time-frequency representation, but has the drawback of a fixed window length. Wavelets can also be used to obtain such a time-frequency representation but can resolve a few of the limitations of Fourier analysis and STFT described in the previous section. Instead of decomposing the original time signal in a sum of sine waves with time support from $-\infty$ to $+\infty$, wavelets use signals that are highly localized in time. Therefore, wavelets can be applied to non-stationary signals like EEG. Wavelets can be described as 'brief oscillations' to which usually a frequency range (or center frequency) can be assigned. The continuous wavelet is defined by:

$$C(b,a) = \int_{-\infty}^{\infty} x(t)\phi(\frac{t-b}{a})dt \tag{3.14}$$

with ϕ the chosen wavelet. There are many types of wavelets, each with their own specific properties and applications. Wavelet ϕ has two parameters: scale a and shift b. The shift parameter b corresponds to the convolution of the wavelet with the original time signal and gives us the time information in the time frequency plane (Fig 3.11A). The scale parameter a defines the center frequency of the wavelet and gives us the frequency information in the time-frequency plane. Low values for the scale parameter correspond to high frequencies, high values to high frequencies (Fig. 3.11B). From the scale a of the wavelet, the frequency f of the signal can be estimated as:

$$f = \frac{f_c}{a\triangle t} \tag{3.15}$$

with f_c the center frequency of the wavelet and $\triangle t$ the sampling period. Heisenbergs Uncertainty Principle states that a function cannot be arbitrarily defined both in time and frequency and that the product of both variances is constant. If the variance of the function is increased in the time-domain (by dilating the wavelet), its variance in the frequency-domain is proportionally reduced. The time and frequency variances of the wavelet define the time and frequency resolution of the wavelet transform. By adapting the window width in function of the frequency, wavelet analysis offers thus an optimal compromise for time-frequency resolution (Fig. 3.11C). Although the wavelet's estimate of the frequency at a given time isn't exact and the whole analysis is slightly influenced by the choice of the wavelet, wavelet analysis is considered a very powerful tool in the analysis of the temporal development of the frequency of the EEG.

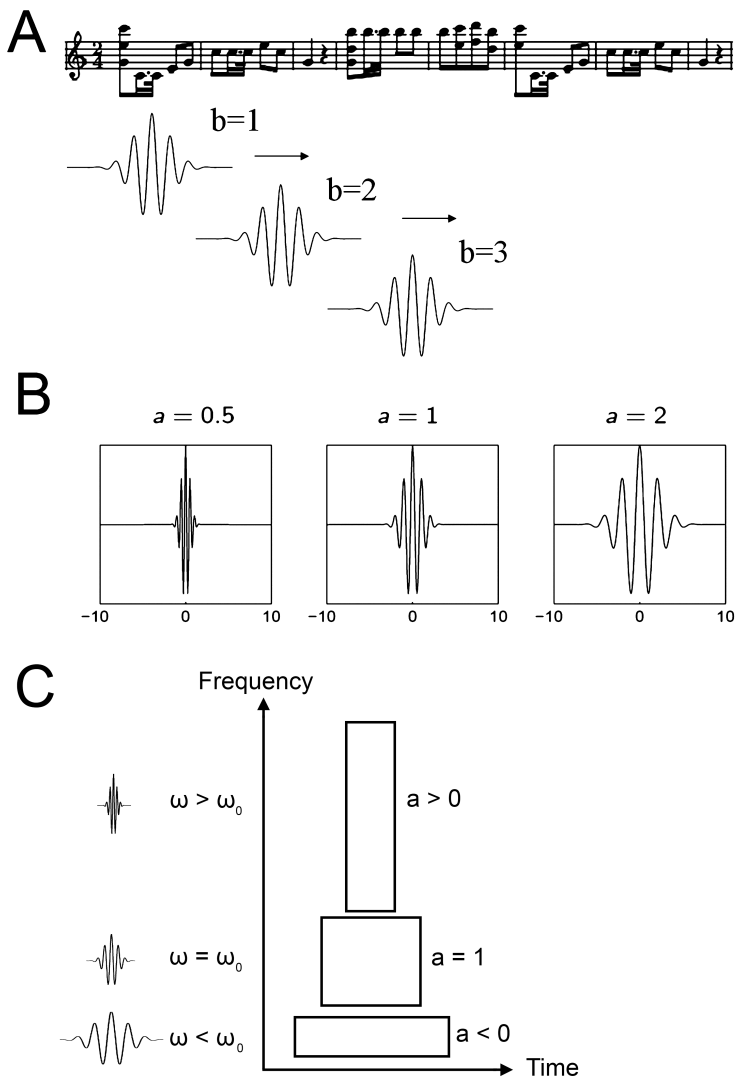

Figure 3.11: *Illustration of the parameters of the wavelet transform. Both parameters a and b together construct the time-frequency plane. A: The shift parameter b shifts the wavelet through the signal in time. B: The scale parameter a defines the center frequency of the wavelet. C: By adapting the window width in function of the frequency, wavelet analysis offers an optimal compromise for time-frequency resolution in contrast to the Fourier transform with fixed window width (see Fig. 3.10).*

Discrete wavelet transform (DWT)

If we are dealing with digitized signals, then to reduce the number of redundant wavelet coefficients, scale parameter a and shift parameter b must be discretized. The DWT attains this by sampling a and b along the dyadic sequence: $a = 2j$ and $b = k^2 j$, where $j, k \in Z$ and represent the discrete dilation and translation numbers, respectively [206].

3.8 Signal properties

3.8.1 Energy of a signal

The energy of a signal is usually associated to the square of the amplitude. Total energy of a sequence x is then defined as the Root Mean Square (RMS) value:

$$RMSx = \sqrt{\frac{1}{N}\sum_{n=1}^{N} x[n]^2} \tag{3.16}$$

with N the number of samples of the sequence. Thus two signals with the same RMS value have the same energy content regardless of their frequency content.

Another way to define energy, is to Fourier transform the signal, and use the absolute squared value of the different frequency bands as a measure for the energy level of the respective bands. In the discrete case, we can say that if

$$S[n] = DFT(x) \tag{3.17}$$

then $|S[n]|^2$ determines how much energy the signal contains at frequency band n. DFT is the Discrete Fourier Transform operator:

$$X(f) = \sum_{n=0}^{N-1} x(n) e^{-i2\pi kn/N}, k = 0, 1, ..., N-1 \tag{3.18}$$

This means that a signal of 10Hz with amplitude 1 and another signal of 1000 Hz and amplitude of 1 will contain the same energy (but in different bands) using this model.

Both former energy definitions based on amplitude and frequency are rather odd. The energy needed to generate a simple sinusoidal signal is dependent on both amplitude and frequency. This observation led Kaiser to the derivation of the Teager Energy Operator also called Non-Linear Energy Operator (NLEO) [99].

Kaiser used the following differential equation as a starting point for the operator:

$$\frac{d^2x}{dt^2} + \frac{k}{m}x = 0 \tag{3.19}$$

This second order differential equation describes an object with mass m suspended by a string with constant k. The solution of this differential equation is

$$x(t) = A\cos(\omega t + \phi) \tag{3.20}$$

where $x(t)$ is the position of the object at time t, A is the amplitude of the oscillation, $\omega = \sqrt{\frac{k}{m}}$ is the frequency of the oscillation, and ϕ is the initial phase.

The total energy of the object is in physics given as the sum of the potential energy of the spring and the kinetic energy of the object, given by:

$$E = \frac{1}{2}kx^2 + \frac{1}{2}mv^2 \tag{3.21}$$

By substituting $v = dx/dt$, and $x = Acos(\omega t + \phi)$, we get

$$E = \frac{1}{2}m\omega^2 A^2 \tag{3.22}$$

From this, we immediately see that the energy of the object is proportional to both A and ω.

Kaiser defined the NLEO, in its discrete form, as:

$$\psi_{kaiser}[x_{(n)}] = x_{(n)}^2 - x_{(n-1)}.x_{(n+1)} \tag{3.23}$$

With $x_{(n)}$ denoting the current sample of signal x, $x_{(n-1)}$ the first sample before sample n, etc. It can be proven that this simple formula has a quadratic relationship to both the amplitude A and frequency ω of the signal $x(n)$ by taking the following signals [222]:

$$x(n) = A.\cos(\omega_0 n + \phi) \tag{3.24}$$

With A the amplitude, ω_0 the angular frequency and ϕ the phase,

$$x(n+1) = A.\cos[\omega_0(n+1) + \phi] \tag{3.25}$$

$$x(n-1) = A.\cos[\omega_0(n-1) + \phi] \tag{3.26}$$

Using the following trigonometric identities:

$$\cos(\alpha+\beta)\cos(\alpha-\beta) = \frac{1}{2}[\cos(2\alpha) + \cos(2\beta)] \tag{3.27}$$

$$\cos(2\alpha) = 2\cos^2\alpha - 1 = 1 - 2\sin^2(\alpha) \tag{3.28}$$

Yields:

$$\psi_{kaiser}[x_{(n)}] = A^2\sin^2(\omega_0 n) \tag{3.29}$$

This formula indicates that the output of the NLEO is proportional to the square of both the amplitude and the frequency ($\sin(\omega_0) \approx \omega_0$ for small ω_0). Fig. 3.12 illustrates this behavior.

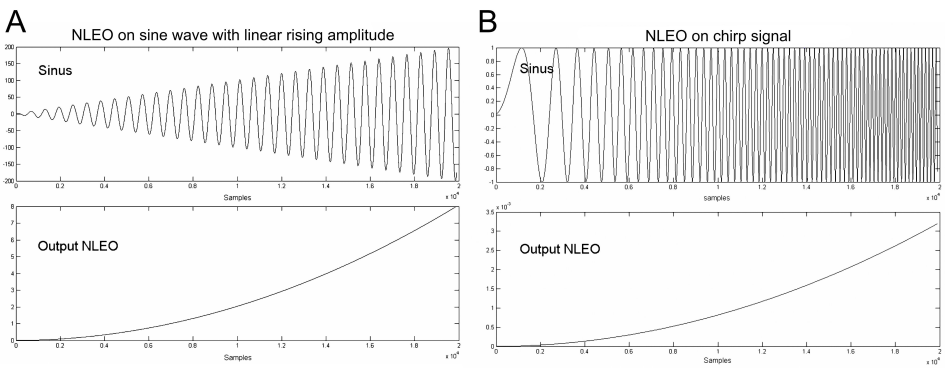

Figure 3.12: *Illustration of the quadratic relationship of the NLEO with frequency and amplitude. (A): Output of the NLEO on a sine wave with fixed frequency and linearly increasing amplitude, (B): Output of the NLEO on a chirp signal.*

In this regard, the NLEO may be considered superior to other energy estimators that simply use the square of the signal or fourier transform and are independent of frequency and amplitude respectively. A generalized version, which is more robust to noise, is given by Plotkin et al. [166]:

$$\psi_{kaiser}[x_{(n)}] = x_{(n-l)}.x_{(n-p)} - x_{(n-q)}.x_{(n-s)} \tag{3.30}$$

$$l + p = q + s \tag{3.31}$$

An ideal energy operator would be one based on the energy needed by the biological brain tissue for signal generation instead of mechanical energy as the NLEO does. But to this date, there are no good estimates of the energy used by the brain to generate a certain EEG signal.

3.8.2 Entropy of a signal

There are many types of entropy measures for a signal. In this thesis we will only make use of the most common entropy measure, namely 'Shannon entropy' [186]. Shannon entropy (SE) was originally developed to describe the capacity of a communication channel and is the foundation for other entropy measures introduced later. The Shannon entropy of a continuous random variable with

density function $p(x)$ is defined as:

$$SE = -\int_{-\infty}^{\infty} p(x)log(p(x))dx \tag{3.32}$$

The entropy of a discrete random variable with probabilities $p_1, \ldots, p_n$ is defined as:

$$SE = -\sum_i p_i log(p_i) \tag{3.33}$$

The SE can be interpreted as a measure of randomness. Lower values of Shannon entropy are associated with reduced uncertainty or increased predictability.

As discussed earlier, the EEG is a highly non-stationary signal. This non-stationarity can be regarded as an increased uncertainty of the frequency content in time. Therefore, SE can be used to quantify the non-stationarities at specific frequencies [205, 201]. Imagine we obtain a time-frequency distribution tfr, (for instance using the continuous wavelet transform). Define $tfr(\omega_i)$ as:

$$tfr(\omega_i) = \frac{1}{N}\sum_{n=1}^{N} tfr(\omega_i, n\Delta t) \tag{3.34}$$

thus $tfr(\omega_i)$ is the sum of all values of the time frequency representation at one specific frequency. In a stationary signal $tfr(\omega_i, n\Delta t)$ is a constant value as the frequency content at ω_i does not change in time. As EEG is a non-stationary signal, $tfr(\omega_i, n\Delta t)$ does change in time and this can be quantified using SE. We can define the probabilities $p_{\omega_i, n\Delta t}$ to calculate SE as:

$$p_{\omega_i, n\Delta t} = \frac{tfr(\omega_i, n\Delta t)}{tfr(\omega_i)} \tag{3.35}$$

Then the SE at frequency ω_i can then be calculated according to equation 3.33:

$$SE(\omega_i) = -\sum_{n=1}^{N} p_{\omega_i, n\Delta t}.log(p_{\omega_i, n\Delta t}) \tag{3.36}$$

When $SE(\omega_i)$ is calculated for a whole set of frequencies we are able to compare the amount of non-stationarities of the EEG for different frequencies.

Chapter 4

Automated neonatal seizure detection

This chapter describes the development of an automated neonatal seizure detector mimicking the human observer. First, an overview is given of the challenges in neonatal seizure detection and what can be found in literature. In our own detection strategy, we divide the seizures into two dominant morphological types. For each type, a separate detection strategy is developed and described. We validate the algorithm on a large dataset scored by an experienced clinical neurophysiologist. We conclude the chapter with a discussion of the results and possible problems.

4.1 Introduction

Automated neonatal seizure detection is a challenging problem. Neonatal seizures have an extremely variable morphology, frequency, and topography, even within the same patient [120, 187]. The performance criteria for an automated seizure detection system to be usable in practice are extremely high. Sensitivity needs to be high as no seizures should be missed (especially in patients with a low number of seizures). Specificity must also be high to limit the number of false positive detections. Only a few percent of all measured EEG data is actual seizure data. Thus we need an algorithm that detects rare events with high sensitivity and specificity. To meet these criteria, features must be found that are exclusively associated to seizures and not to other non-seizure EEG patterns. Considering the large variability among seizures these are hard to find. Another problem is the absence of a real gold standard. There is no full agreement among experts about what is a seizure and what is not. We established that the inter-

rater agreement between two experienced clinical neurophysiologists in scoring the number of seizures in 1-h segments of EEGs from 10 patients was 73%. This indicates that neonatal seizure definition and classification is still a developing field.

In the literature, many seizure detection algorithms have been described. The best known methods are based on computing a running autocorrelation function [116], rhythmic discharges detection [68], modeling and complexity analysis [24], and wave-sequence analysis [143]. Others are based on the extraction of features using entropy, wavelets, frequency content, etc., and then training a classifier [69, 224, 1] on these features to correctly categorize the EEG. Our approach to the detection of neonatal seizures is to develop an algorithm which mimics a human observer reading EEG, as it is essentially the human observer we are trying to replace. We identified two major characteristics of neonatal seizures which lead to their detection by a human observer. The first characteristic is that all seizures represent a clear change relative to the background EEG. The second and most important characteristic is the repetitiveness of the signal, because nearly all seizures display some kind of recurrent pattern. We aimed to develop an algorithm based on these two characteristics using time domain signal processing, as this is the most straightforward way to mimic the human observer. The implementation is based on several concepts already introduced in the literature, but we combined and improved these and added some of our own concepts.

4.2 Detection methods

4.2.1 Detection strategy

When analyzing the neonatal seizures, we identified two major seizure types. The first type is what we call the spike train seizure type (Fig. 4.1A); the second is what we call the oscillatory seizure type (Fig. 4.1B). Nearly all neonatal seizures can be classified uniquely into one of these types or as a combination of the two types (Fig. 4.1C). In our dataset, roughly 50% of all seizures consisted of a combination of the two types, 35% were purely consisting of spikes and the remaining 15% were pure oscillatory seizures.

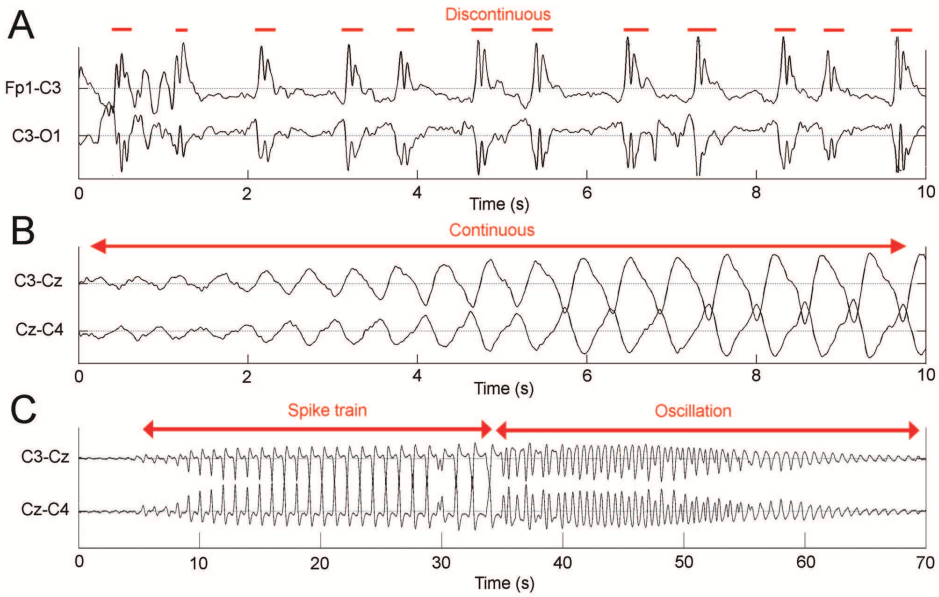

Figure 4.1: *(A) Example of a spike train type seizure, (B) example of an oscillatory type seizure, (C) example of a seizure consisting of both morphologies. The seizure starts with a spike train and ends with an oscillation.*

The major difference between the two types is that the oscillatory type is a fluent, continuous seizure, whereas the spike train type consists of isolated spikes appearing on a background of lower voltage EEG. This means that the oscillatory type has a continuous kind of repetitiveness while the spike train type has a discontinuous kind. Another difference is that the oscillatory activity generally has lower frequency content than the high-frequency spikes. We need to stress that this categorization into two seizure types is not based on any physiological interpretation, but was adopted purely from a signal processing point of view. A detection algorithm was developed for each seizure type separately. During analysis, both algorithms run in parallel and detection occurs if one or both of the algorithms detects a seizure. The two algorithms are calculated on each EEG-channel separately. When detection occurs in one channel, the complete EEG at that time instance is regarded as seizure activity, independent of the detection result on the other channels. Although the two algorithms differ completely in their implementation, they are closely related and matched to each other. Fig. 4.2 gives an overview of the complete detection strategy and implementation. The scheme serves as a guide through the explanation of the seizure detection in this chapter and each block will be explained in the following sections. We will first explain the spike train type detection and then the oscillatory type detection.

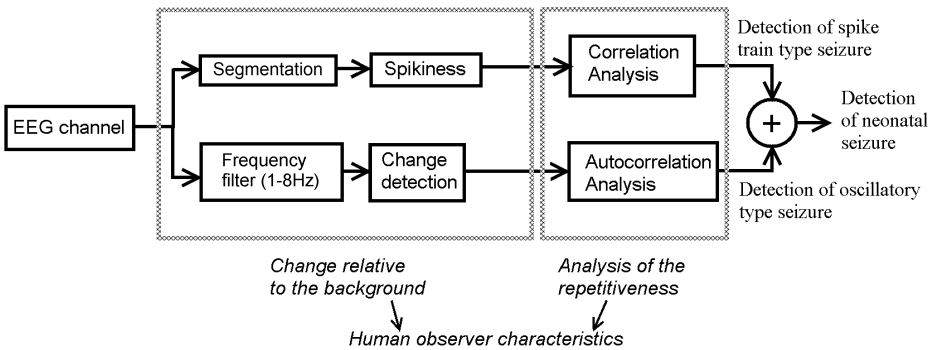

Figure 4.2: *Schematic overview of the complete seizure detection algorithm. The upper row shows the steps of the spike train detection, the lower row, the sequences of the oscillatory type detection. The complete seizure detection algorithm consists of the sum of the two detection algorithms.*

4.2.2 Spike train type seizure detection

Our human observer approach indicated that the spike train algorithm must detect a repetitive train of isolated spike like segments of EEG. Accordingly, the algorithm consists of two steps. The first step isolates the spike-like segments or transients and the second will analyze the similarity between these isolated segments.

Segmentation of the transients in the EEG

This first step is critical as the subsequent steps in the algorithm rely on the proper segmentation of the transients. Fig. 4.3 displays a schematic overview of the segmentation process. Each block will be explained in the next paragraphs. All of these steps are applied on single channel EEG windows of 5 s in duration. There is an overlap of 4 s between subsequent windows under analysis.

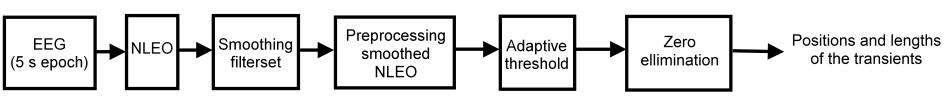

Figure 4.3: *Schematic overview of the segmentation step of the spike train detection. The segmentation is performed on 5 s long windows of EEG. For each EEG window, the output are the positions and lengths of the transients in the EEG.*

The non linear energy operator (NLEO)

To detect the local presence of high frequency activity, we use a non-linear energy operator (NLEO) as proposed by Kaiser [99].

$$\psi_{kaiser}[x_{(n)}] = x_{(n)}^2 - x_{(n-1)}.x_{(n+1)} \tag{4.1}$$

With basic properties:

$$\psi_{kaiser}[x_{(n)}] = A^2 \sin^2(\omega_0 n) \tag{4.2}$$

This formula indicates that the output of the NLEO is proportional to the square of both the amplitude and the frequency. When applied to spike train type seizure EEG, the effect is that it will amplify the high-frequency spikes relative to the background EEG. Thus the NLEO accentuates the spikes. In this thesis we used the version defined by Plotkin et al. [166] which is more robust to noise.

$$\psi_{kaiser}[x_{(n)}] = x_{(n-l)}.x_{(n-p)} - x_{(n-q)}.x_{(n-s)} \tag{4.3}$$

$$l + p = q + s \tag{4.4}$$

As parameter settings, we used l=1, p=2, q=0, and s=3 [3] to calculate the energy as locally as possible. Fig. 4.6B shows the effect of the NLEO on the EEG plotted in Fig. 4.6A.

Smoothing of the NLEO

The NLEO calculates the energy of the signal based on only a few samples and thus very local in time. The spikes of a neonatal spike train type seizure vary somewhere between 50 ms and 500 ms. In order to match the sensitivity of the NLEO to the duration of the spikes, the NLEO output needs to be smoothed. As the variation in duration of the spikes is large (50-500 ms) it is not possible to find one smoothing filter length that is adequate for both short and long spikes. This problem was solved by using a smoothing filter bank with 6 Moving Average (MA) filters with filter lengths of 2-4-8-16-32 and 64 samples. Using a sampling frequency of 256Hz, this leads to a set of filters in the order of ms up to 250 ms. The output of one filter is the input of the filter with next increasing MA filter length. The output of the filter bank is the summation of the outputs of each filter (see Fig. 4.4).

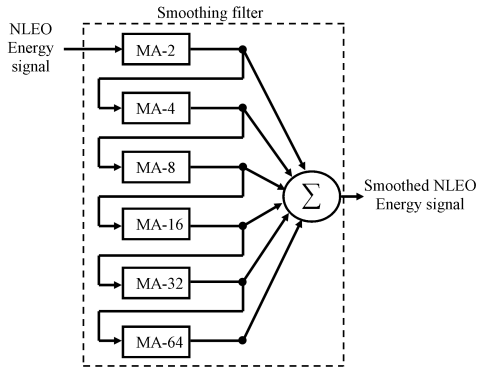

Figure 4.4: *Schematic of the smoothing filter applied on the NLEO energy signal. MA stands for Moving Average filter, the number is the length of the filter. The input of each filter is the output of the previous filter with smaller filter length. The output of each filter is then summed and normalized to form the smoothed NLEO energy signal.*

The resulting smoothing of the NLEO output leads to a smooth signal in which short as well as long spikes can easily be discriminated due to the varying lengths of the smoothing filters. Fig. 4.6C displays the smoothing effect on a spike train type seizure with long spikes (>500 ms). The arrows on Fig. 4.6B and C indicate that short peaks in the NLEO output are conserved after the smoothing. Only variations on a large time scale of the NLEO output are smoothed out. This is exactly the behavior needed to be sensitive for both short and long spikes.

preprocessing the smoothed NLEO output before thresholding

Two preprocessing steps are performed before thresholding the smoothed NLEO output:

- The smoothed NLEO energy is normalized to values between 0 and 1.
- A negative offset is applied to the normalized NLEO energy equal to the area under the curve. When the normalized NLEO energy is strongly peaked, this negative offset is small. When the normalized NLEO energy is more uniform the offset is larger. To understand why this is a good behavior the next step must be explained first.

Adaptive thresholding

The goal of this step is to find a suitable threshold to discriminate between high and low energetic energy. After thresholding, the high energetic parts of the signal are transformed to isolated segments of high energy with a certain position and length. The threshold must be at a level to detect the transients in the EEG

without segmenting small, insignificant variations in the energy signal. To do that, segmentation is performed for a set of thresholds between 0 and 1 with a step size of 0.02. For each threshold the number of segments above the threshold is counted (see Fig. 4.5 with 2 thresholds leading to 4 respectively 9 segments). The threshold that leads to the maximum number of segments is kept as the definitive threshold. For example in Fig. 4.5, the definitive threshold leads to 9 isolated segments. Consider the second energy peak just after second 1 in Fig. 4.5. The energy of this second peak is much smaller than the surrounding peaks, making it difficult to segment. Our approach of a varying threshold with maximum segment number has no problem of detecting it.

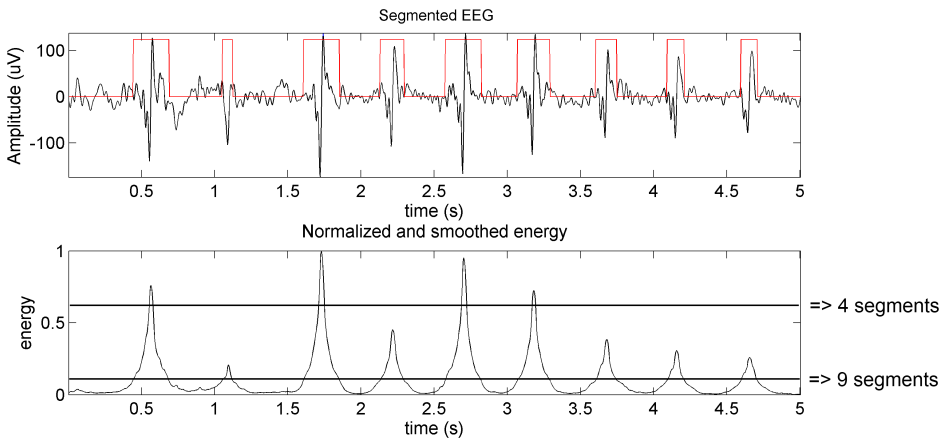

Figure 4.5: *Illustration of the determination of the threshold on the smoothed NLEO output. The threshold is varied between 0 and 1 and for each threshold the number of segments above the threshold is counted. The threshold leading to the most segments is used for the final segmentation as this provides maximum sensitivity.*

In the previous preprocessing step a negative offset is applied corresponding to the area under the curve. This negative offset prevents the insignificant energy variations from being segmented as these are now below the zero level. When the energy signal is strongly peaked, the area under the curve is (due to the normalization) relatively small leading to a small offset. When the energy signal is more uniform, the area under the curve is larger leading to a larger negative offset. This is good behavior as a uniform energy signal is less likely to contain interesting energy peaks. Because of the negative offset, the most uninteresting peaks are under the zero level and thus ignored in the segmentation.

Zero elimination

So far, all steps of the spike train detection algorithm performed are dedicated to maximum sensitivity to segment transients in the EEG. From now on all remaining

steps of the algorithm are aimed at lowering the number of segments as in the end only those segments that are part of a spike train type seizure should be kept. This elimination of segments starts with the process of zero elimination.

The previous segmentation step searches for the threshold leading to the maximum number of isolated high energetic segments. Therefore it might happen that a small dip in the smoothed energy signal leads to a spike being segmented into two (or even more) isolated segments (see Fig. 4.6D). To correct this false segmentation, isolated low energetic zero segments shorter than 100 ms are removed and combined with the high energetic segments surrounding it (see Fig. 4.6E). This zero elimination may not be set too long, to avoid that separate spikes close to each other are grouped into a single spike.

Spikyness

The human observer approach requires the spikes to be 'isolated' from the background activity. We implemented this requirement by calculating the spikyness of each high-energetic segment using:

$$spikyness = \frac{max(segment)}{mean(background)} \tag{4.5}$$

The background is defined as the EEG with the length of the considered segment just before and after the spike (see Fig. 4.7). Only segments with a minimum length of 50 ms and a spikyness higher than 3 are kept. In this way, the spikyness requirement works as a data reduction step and removes insignificant transients in the EEG.

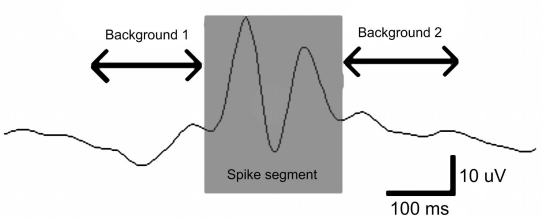

Figure 4.7: *Illustration of the calculation of the spikyness of the detected segments.*

Grouping multiple detections

Segmentation is done on overlapping windows of 5 s duration with an overlap of 4 s. This implies that the transients in the EEG are likely to be segmented multiple times. These multiple segmentations of the same transients must be grouped into

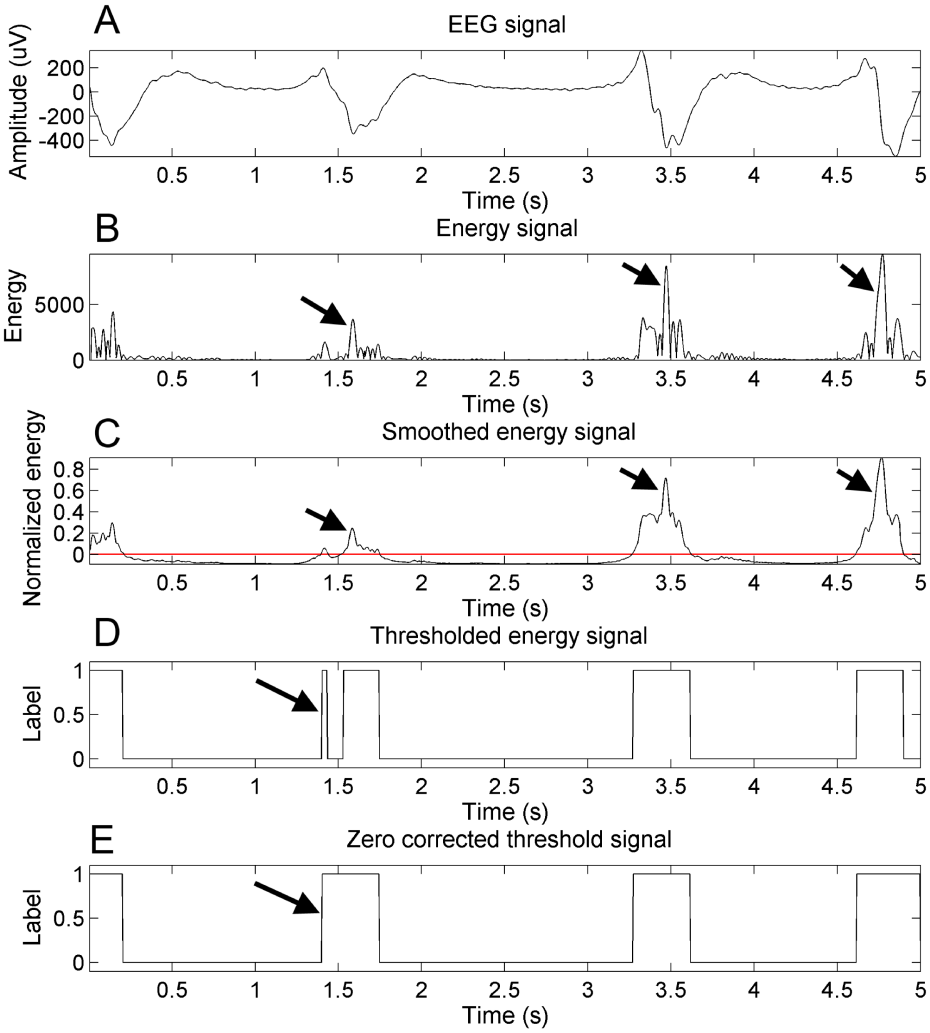

Figure 4.6: *Illustration of the subsequent steps of the segmentation process (see Fig. 4.3). (A): 5 s of spike train type seizure EEG. (B): Output of the NLEO. (C): Output of the smoothed NLEO. Note the negative offset of the smoothed energy signal compared to the raw energy signal in Fig. 4.6B, the zero level is marked with a light grey line. Everything that is under the zero level can not be segmented. (D) Output after segmentation of the smoothed NLEO output. (E) Output after eliminating short zero segments in between ones.*

a single segment. Therefore the following grouping rules were defined (see Fig. 4.8).

- If there is a partial overlap between 2 segments, the resulting segment gets the mean position between the 2 beginnings and endings.
- If there is a complete overlap between 2 segments, the resulting segment is equal to the largest segment and thus the smallest segment is ignored.
- If there is no overlap between segments, both are treated as segmentations of different transients and thus both are kept for further analysis.

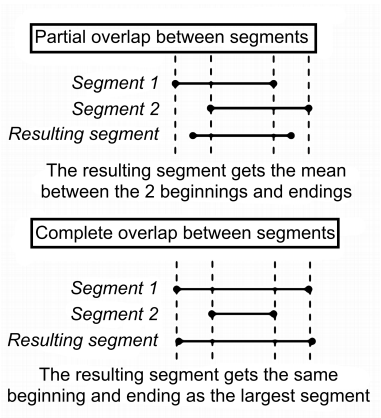

Figure 4.8: *Grouping rules for multiple segmentations of the same transients in the EEG. Segments that are partially overlapping and completely overlapping are treated differently.*

To summarize the segmentation, first those segments which are high-energetic with respect to the complete epoch are detected and next, the spikyness further reduces the number of segments to those which are high-energetic on a very local scale (isolated by comparatively low-energetic EEG). Finally, overlapping segments are grouped into a single segment.

Analysis of the correlation

Following our human observer's approach, we now have to deal with the repetitive character of the seizures. In time domain processing, repetitiveness (or in this case: similarity between segments) can be estimated using correlation analysis. To detect the occurrence of a repetitive pattern of segments, we developed a correlation scheme able to detect a discontinuous repeating pattern of transients by

growing a set of highly correlated segments (Fig. 4.9). Such a set starts with just one segment and every detected segment of the segmentation step will be used as a starting point for the correlation scheme. In the first step, the cross-correlation of the first segment with the previous segment is calculated. If the maximum value of that cross-correlation is >0.87, that previous segment is added to the set. Next, the preceding segment is selected and the cross-correlation with the two segments of the set is calculated (step 2). If the mean of those two maximum cross-correlations is >0.87, that new segment is also added to set. In case of a repetitive signal, repetition of this process (step 3 etc.) leads to a set of segments which are highly correlated with each other.

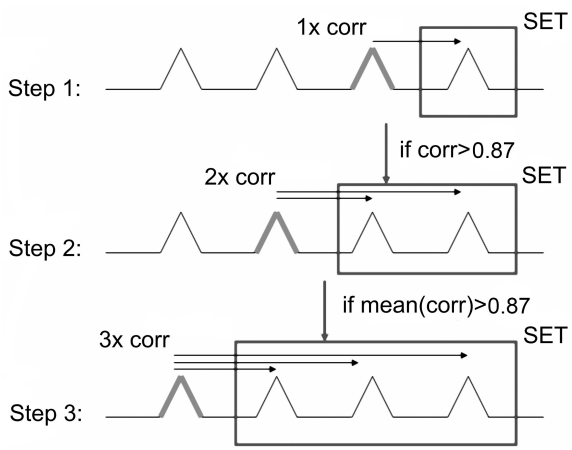

Figure 4.9: *Analysis of the correlation between the segments. In case of a repetitive pattern, a set of highly correlated segments is grown. A spike train seizure is detected when at least 6 correlated segments are found.*

An important parameter is when to stop the process as it is not efficient to search back for correlated segments indefinitely. This maximum time lag is dependent on the length of the first segment the process started with. Only segments which occur with a time lag less than 30 times the length of the first segment are checked. By restricting the time lag based on the length of the first segment, the search is adapted to the length of the correlated segments the algorithm is searching for and thus adapted to the patient's EEG. In case the first segment is longer than 0.5 s, the maximum search back length is limited to 20 s. Due to this flexibility, the sensitivity of finding correlated spikes is the same for short as for longer segments (up to 0.5 s). As this search for correlated segments is calculated for every segment detected in the segmentation step, several (possibly overlapping) sets of correlated spikes will be found in case of a spike-train type seizure. When the spikes of these sets are less than 20 s apart, they are grouped into a single detection.

The above process allows for some variation in the morphology of the spikes. The initial correlation must exceed 0.87, which implies a strong similarity. However, when a set starts growing, the similarity may occasionally become less, as only the mean of the correlation with all segments of the set is used. Fig. 4.10 shows the results of this algorithm. The grey shaded spikes are those that are detected as being part of a spike train type seizure. The segments with a rectangle around them are also detected by the segmentation step, but removed by the spikyness and correlation analysis and thus are not detected as being part of a spike train type seizure.

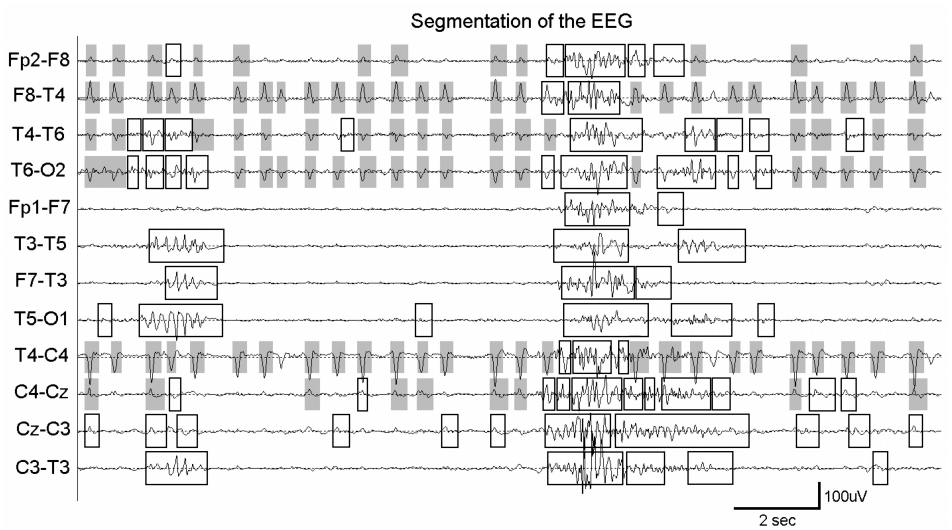

Figure 4.10: *Example of spike train detection. All marked segments (grey-shade + delimited by rectangle) are detected by the segmentation step. After applying the spikyness operator and correlation analysis, only the shaded segments remain. Only these segments having a high correlation with previous segments (shaded) are detected as being part of a spike train type seizure.*

4.2.3 Oscillatory type seizure detection

A human observer seems to detect oscillatory type seizures as continuous repetitive activity that represents an increase of low frequency activity relative to the background. In time domain processing, the autocorrelation function is useful for finding a repeating pattern in a signal and, thus, for handling the repetitiveness of oscillator-type seizures. The autocorrelation is the cross-correlation of a signal with a delayed version of itself. Liu et al. [116] suggested a method based on the autocorrelation function to detect rhythmic discharges in the neonatal EEG.

Navakatikyan et al. [143] have shown that Liu's method displays a high sensitivity but also a high number of false positives. We therefore aimed to develop an autocorrelation-based analysis with a very low false positive rate. This algorithm consists of 2 steps. The first step detects an increase of low-frequency activity and the second analyzes the autocorrelation function of these increases.

Detection of an increase in low frequency content

Every EEG channel is band pass filtered between 1 and 8 Hz using 2 FIR filters with a 256 sample length. To detect significant increases in the resulting signal, a window with a length of 3 s is moved along the signal. The threshold for detecting an increase is adaptive and defined as follows.

$$newThreshold = 0.5 * currentBackground + 0.5 * oldThreshold \tag{4.6}$$

A new threshold is based on 50% of the previous value of the threshold and 50% made adaptive to the current background. The current background is calculated using 30 s of EEG before the current window under analysis. The threshold is initialized to 0 at the start of the seizure detection. Thus it takes a few iterations before the threshold is at its nominal level due to the dependency on the previous values of the threshold. If a window is detected, this activity is considered potential oscillatory seizure activity. All EEG data that is not detected in this step is removed from further analysis.

Autocorrelation analysis

At this point, we have detected significant changes of activity in the frequency band of 1-8 Hz. What remains is the analysis of the repetitive aspect of the signal. As described above, our goal is to detect repetitive signals by means of the autocorrelation function. The detected windows in step 1 are divided into 9 s epochs (8 s overlap between epochs) and the autocorrelation function of the epochs is calculated. Fig. 4.11 shows two examples of epochs with their autocorrelation functions.

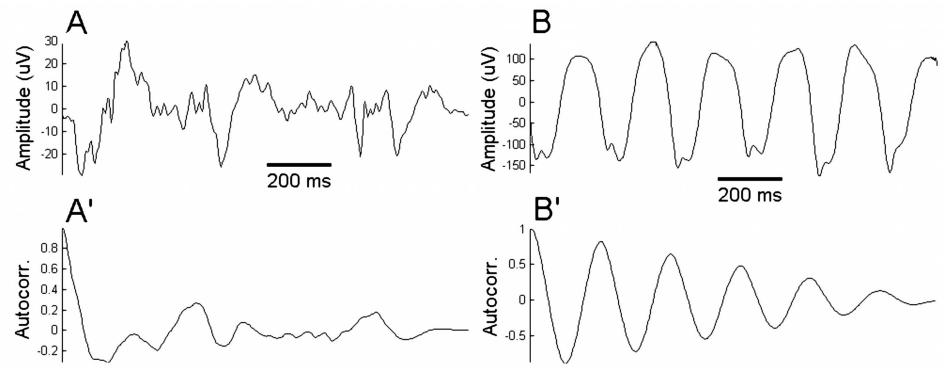

Figure 4.11: *Difference between the autocorrelation functions (A' and B') of a non-repetitive (A) and repetitive signal (B).*

To distinguish between repetitive and non-repetitive signals, 3 features of the autocorrelation function are extracted.

- Regularity of the distances between the zero crossings (Fig. 4.12A) defined as 'errorZeros'.
- Regularity of the distances between the peaks (Fig. 4.12B) defined as 'errorPeaks'.
- Regularity of the normalized RMS values of the peaks which are delimited by the zero crossings (Fig. 4.12C) defined as 'errorRMS'.

Regularity is measured by a pair wise comparison (percentage difference) of all distances or RMS values involved. All pair wise comparisons are grouped in one vector. The thresholds on the features are defined as:

- median([errorZeros,errorPeaks])<7%
- median(errorRMS)<10%

The comparisons for the zero crossings and the distances between the peaks can be grouped together as both are distance measures. The comparisons for the RMS values are treated separately. All signals with properties below these thresholds are considered to be part of an oscillatory seizure.

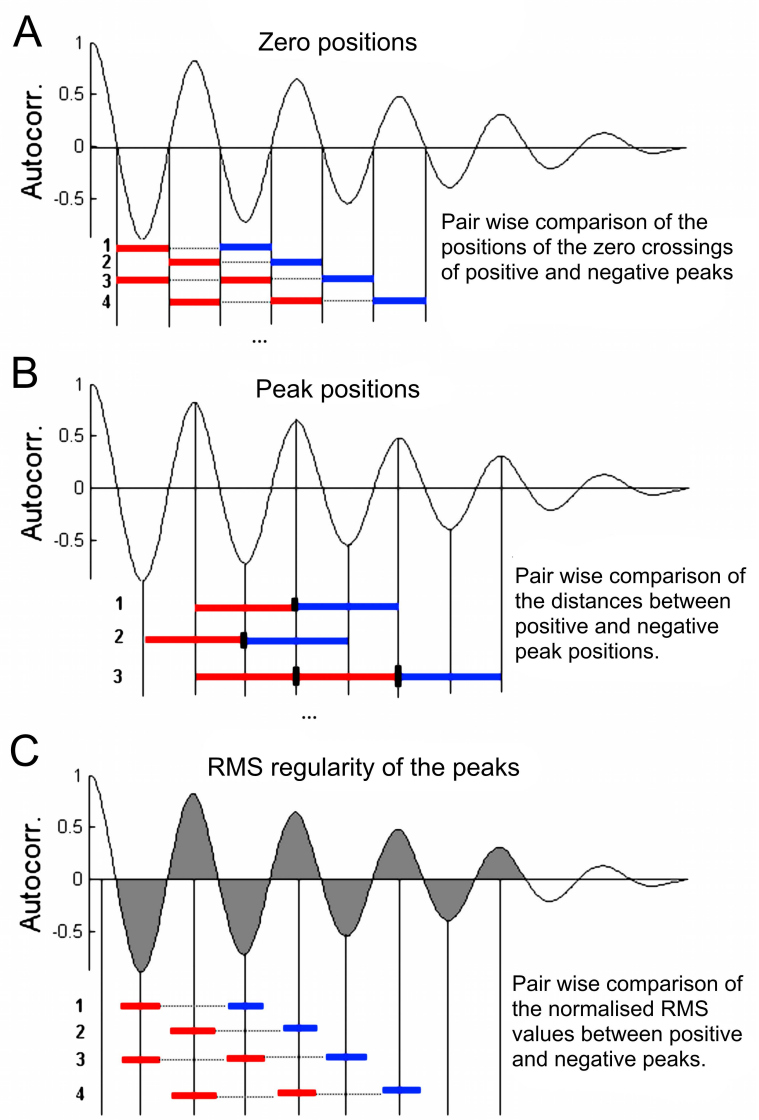

Figure 4.12: *Illustration of the extracted features of the autocorrelation. (A): The regularity of the zero crossings of negative and positive peaks, (B): The regularity of the distance between positive and negative peak positions, (C): The regularity of the normalized RMS values of the positive and negative peaks.*

It is important for each of these features that positive peaks are compared to other positive peaks and negative peaks to other negative peaks. This is necessary as it might be that oscillatory seizure EEG is not symmetric in shape for positive amplitudes compared to the shape of negative amplitudes (see Fig 4.13). The resulting autocorrelation function for this type of signal is also asymmetric for positive and negative values of the autocorrelation function. These type of signals are continuously repetitive as a whole, but are also discontinuously repetitive for positive and negative amplitudes. This effectively puts them at the boundary between being a spike train type seizure and an oscillatory type seizure. The stronger the asymmetry, the more it is a spike train, the stronger the symmetry, the more it is a pure oscillation. As there is an overlap between the two seizure types it is possible for seizures to be detected by both algorithms. Fig. 4.14 shows the detection result of both algorithms on a seizure with such properties. The seizure starts and ends as a pure oscillation and is accordingly only detected by the oscillation detection. But in the middle part, the seizure becomes sharper in the positive and more flattened in the negative amplitude resulting in detection by the spike train detection. But as the seizure is still continuously repetitive, also the oscillation detection is able to detect it.

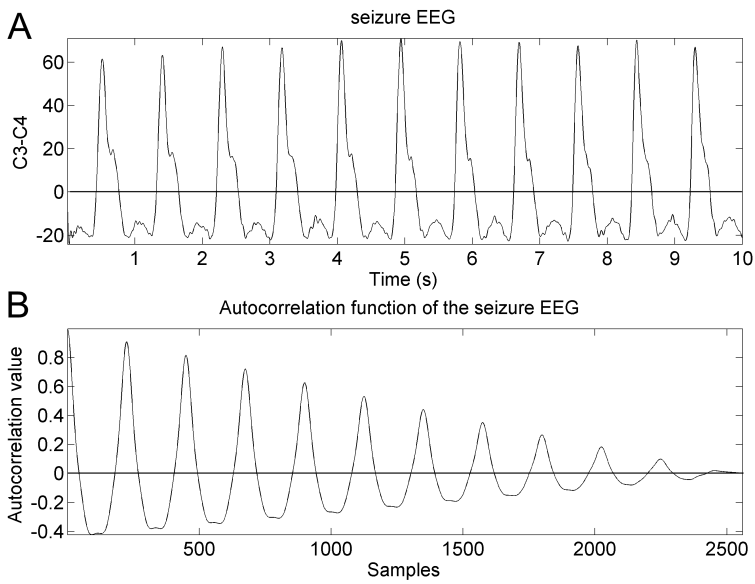

Figure 4.13: *A: Illustration of a seizure pattern with a different shape for the positive and negative amplitude. This seizure pattern is continuously repetitive as a whole, but is discontinuously repetitive for positive and negative amplitudes. Thus, this seizure pattern can be considered both oscillatory and spike train type. B: Autocorrelation function of the seizure pattern. This figure illustrates the need to treat the negative and positive peaks of the autocorrelation independently.*

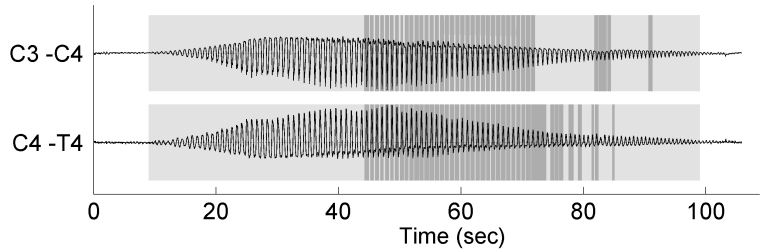

Figure 4.14: *Illustration of a seizure that is detected by both detection algorithms. The beginning and end is pure oscillatory and accordingly only detected by the oscillation detection (marked in light gray). The middle part of the seizure is sharper but still continuously repetitive and thus detected by both detection algorithms (detected spikes are marked in dark gray).*

4.2.4 Performance measures

Presenting the performance of a seizure detection algorithm is not straightforward. Different ways to measure the performance of an algorithm have been reported in the literature, leading to varying results, which cannot be easily compared. In addition, all these algorithms were tested on different datasets, which makes a comparison even more difficult. We chose to present all types of measurements one can think of to measure the performance of the detector:

We defined the sensitivity per patient ($SensPP$) as the percentage of the number of seizures marked by the neurologist that are detected.

$$SensPP = \frac{SZdetPP}{SZtotPP}.100 \tag{4.7}$$

with $SZtotPP$ the number of seizures marked by the neurophysiologist for a patient, and $SZdetPP$ the number detected by the algorithm for that patient. A seizure was considered as detected when there was a temporal overlap between the marked seizure and the detection. The total sensitivity for all patients is calculated using 2 methods. The first method simply averages all sensitivities per patient ($SensT_PP$). The second method ($SensT$) measures the percentage of seizures detected of all seizures present in the complete dataset. So, $SensT_PP$ measures the expected sensitivity at the patient level and SensT at the seizure level. The importance of the difference is that in $SensT_PP$, a patient with only a few seizures is considered to be equally important as a patient with many seizures. $SensT$, on the other hand, regards all seizures as equally important regardless of the patient they occurred in. Occasionally, a single seizure was detected several times by the algorithm. All such events were combined into a single $EVsz$ detection.

We use two types of Positive Predictive Value (PPV). PPV_num is defined as the percentage of detected events that match seizures.

$$PPV_num = \frac{EVsz}{EVtot}.100 \tag{4.8}$$

with $EVtot$ the total number of detected events and $EVsz$ the total number of detected seizures. In practical terms, the PPV_num gives the chance the detector has detected a true seizure for each detection. PPV_num is event based, which means that the duration of the event is not taken into account. The PPV_num is dependent of the a priori likelihood of seizures in the dataset.
The second PPV measurement is PPV_dur and it is defined as the percentage of time the detector is detecting a true seizure compared to the time it is detecting a false positive. PPV_dur is duration based (in seconds), which means that the actual number of true and false positive events does not matter, only their duration is important. The PPV_dur is dependent of the a priori seizure burden (SB) in the dataset. SB is the total duration of seizure activity in the dataset.
Both PPV_num and PPV_dur are dependent on a priori seizure information in the dataset, which makes it difficult to compare different datasets. But nevertheless it is an interesting measure for the performance of the detector. When both measures are given, a good insight can be obtained into the reliability of the detector as we get event- and time based information of the balance between true and false detections.

Another useful measure of performance is the number of False Positive detections per hour (FP/h). This measure represents an important indicator of the practical usability of the algorithm, because each FP implies that somebody in the NICU will have to check the patient and the raw EEG recording unnecessarily.

We also quantified the sensitivity to detect the Seizure Burden (SB), with $SBtot$ being the total time in seconds marked by the neurophysiologist that the patient is experiencing seizures during the measurement. $SBdet$ is the percentage of $SBtot$ that is detected by the seizure detector. The total sensitivity to detect the seizure burden for all patients is calculated using 2 methods. The first method simply averages all $SBdet$ values per patient ($SBdet_PP$). The second method ($SBdet_Tot$) measures the percentage of seizure burden detected of all seizure burden present in the complete dataset. So, $SBdet_PP$ measures the expected seizure burden sensitivity at the patient level and $SBdet_Tot$ at the dataset level. The importance of the difference is that in $SBdet_PP$, a patient with only a small seizure burden is considered to be equally important as a patient with a large seizure burden. $SBdet_Tot$, on the other hand, regards each second of seizure burden in the complete dataset as equally important regardless of the patient it occurred in.

4.3 Evaluation of the algorithm

4.3.1 Dataset

The used dataset consists of 21 patients with continuous EEG measurements of 8 h (168 h in total). All patients are term neonates with perinatal asphyxia experiencing electrographic seizures. Each measurement started within 24 h of birth. 10 of the 21 patients had the full set of 17 EEG electrodes (Fp1,2, F3,4, C3,4, Cz, P3,4, F7,8, T3,4, T5,6, O1,2) while 11 had a reduced set (P3,4 and F3,4 missing). Inter-rater agreement between two experienced clinical neurophysiologists in scoring the number of seizures in 1-h segments of EEGs from 10 patients was 73%. Subsequently, the data were reviewed jointly by both, and the scored seizures were agreed upon by consensus. The 8 h segments of EEGs were then scored for seizure activity by one of the raters. Seizures were scored when they showed clear variation from the background EEG activity lasting for at least 10 s and showed evolution in time and/or change in amplitude and frequency. The dataset consisted of EEGs with a wide variety of background activity, ranging from low voltage, to burst suppression and normal background activity. No selection has been made regarding artifacts present in the EEG. Before analysis, the data was filtered between 0.3 and 30 Hz.

4.3.2 Results

The results run on the full set of channels are given in Table 4.2. The $SensT_PP$ was 88.3%, $SensT$ was 91.1%, as the algorithms detected 338 of 361 seizures present in the dataset. The PPV_num was 84.9% and the PPV_dur was 92.7%. There were 96 false positive detections, or 0.58 FP/h. The $SBdet_PP$ was 68.6% while the $SBdet_Tot$ was 67.1%.

Fig. 5.8 displays box-whisker plots of the $SensPP$, $SBdef$, PPV_num and PPV_dur measurements. These plots help to identify the dispersion in the results and spot outliers.

The algorithm was also run on several electrode configurations. In the ideal case 17 electrodes are fixed on the scalp of the neonate. In practice it takes quite some time to fix that many electrodes. To be usable in practice many centers will want to attach less electrodes. Therefore we also investigated the impact on the detection performance of a reduced electrode set. We choose to use 6 electrodes (C3-4, T3-4, O1-2) as a trade-off between good spatial resolution and time needed to fix them on the scalp. We choose this selection as the central, temporal and occipital brain regions seem to be the most sensitive for seizure activity. Currently in clinical practice, the CFM monitor is in use in many centers in Europe. This system uses only 2 electrodes, which are mainly fixed as P3-4 or C3-4. To compare the

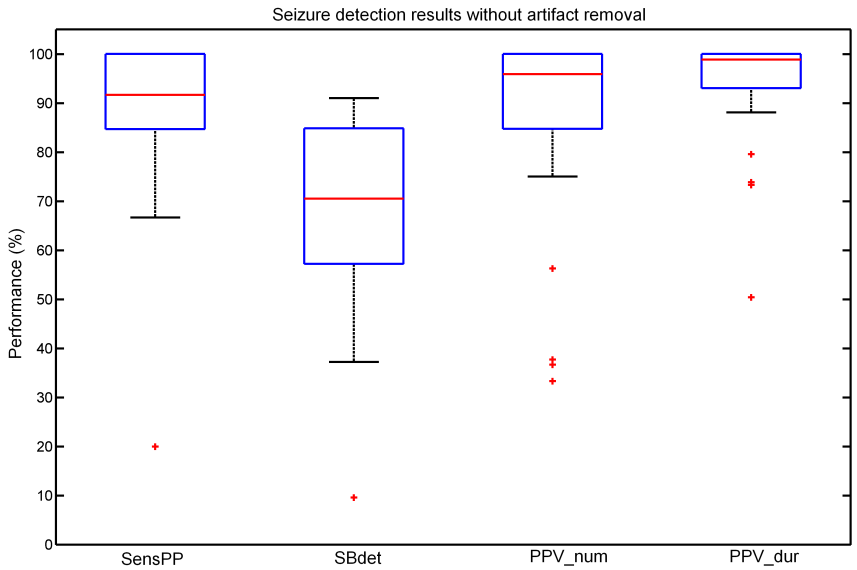

Figure 4.15: *Boxplot results of the SensPP, SBdet, PPV_num and PPV_dur performance measurements.*

	SensT	**FP/h**	**PPV_num**
Full EEG	91.1%	0.58	84.9
6 Channel	70.9%	0.097	91.6
C3-4	54.9%	0.021	95.5
C3-4 CFM	67.8%	0.440	73.0
P3-P4	48.6%	0	100

Table 4.1: *Seizure detection results on different electrode configurations.*

performance of the algorithm with CFM, these 2-channels electrode configurations have also been tested. The results are given in Table 4.1. The results shown on line 'C3-4 CFM' are the results for visual analysis of the CFM trace, scored by experienced neonatologists. All other results shown are automated analysis.

	Seizure detection sensitivity			FP measurements			PPV measurements		Seizure burden sensitivity	
Patient	**SZtotPP**	**SZdetPP**	**SensPP (%)**	**FP_num**	**FP/h**	**FP_dur (s)**	**PPV_num (%)**	**PPV_dur (%)**	**SBtot (s)**	**SBdet (%)**
1	26	26	100	43	5.375	1208	37.7	50.4	1349	91.0
2	67	60	89.6	1	0.125	28	98.4	98.9	3076	85.7
3	24	22	91.7	3	0.375	78	88.0	96.5	2853	76.0
4	5	4	80	8	1	182	33.3	79.6	807	88.2
5	3	3	100	0	0	0	100	100	240	56.7
6	15	15	100	0	0.25	47	88.2	95	1257	70.5
7	31	27	87.1	3	0.375	163	90.0	88.1	1421	84.6
8	17	17	100	0	0	0	100	100	2497	69.0
9	4	3	75	0	0	0	100	100	328	55.8
10	9	9	100	0	0	0	100	100	6961	90.7
11	24	24	100	8	1	144	75.0	94.7	3380	75.9
12	5	1	20	0	0	0	100	100	145	37.2
13	11	11	100	19	2.375	447	36.7	73.9	1416	89.3
14	7	6	85.7	0	0	0	100	100	7390	9.6
15	11	9	81.8	7	0.875	136	56.3	73.3	659	56.6
16	12	12	100	1	0.125	23	92.3	98.8	3080	62.4
17	11	11	100	1	0.125	27	91.7	98.9	3406	72.3
18	20	18	90.0	0	0	0	100	100	2255	60.1
19	54	47	87.0	2	0.25	22	95.9	99.4	4309	82.4
20	3	2	66.7	0	0	0	100	100	835	70.2
21	2	2	100	0	0	0	100	100	678	57.4
		91.1% SensT	**88.3% SensT_PP**		**0.58 FP/h**		**84.9% PPV_num**	**92.7% PPV_dur**	**67.1% SBdet_Tot**	**68.6% SBdet_PP**

Table 4.2: *Seizure detection results.*

4.4 Discussion

In this chapter, we introduce a new approach to detecting neonatal seizures. Our approach is based on two major characteristics of seizures (repetitiveness and a change relative to the background) that a human observer seems to employ. Although all seizures share these properties, their appearance can be very different (continuous versus discontinuous, low versus high frequency). Close observation, however, led to the identification of two types and, consequently, the development of two detection algorithms. For this purpose, we use several concepts that were previously introduced in the literature (autocorrelation, NLEO), but we improve and combine them, while adding some of our own concepts. For example, just like Liu et al. [116], we make use of the autocorrelation - but we only use it to detect seizures with a continuous type of repetitiveness. Furthermore, instead of analyzing the autocorrelation of the complete EEG, we limit the analysis to those parts of the signal that represent an important increase of low-frequency activity relative to the background. The combination of these improvements results in a lower false positive rate compared to previously published algorithms without altering the sensitivity. A novel property of the spike train detection algorithm is its ability to detect repetitive segments of EEG even when two neighboring seizure segments are interrupted by other EEG activity (Fig. 4.10). This adaptive, segmentation-based detection is much more flexible than analyzing a fixed epoch of EEG (like classifier-based approaches do). It is known that neonatal seizures are extremely variable in morphology and frequency ([120, 187]), which makes it very difficult to develop a patient-independent algorithm. To deal with this variability, it is important to develop a data-driven algorithm that either derives its thresholds from the data or uses parameters that are independent of the variability. For instance, in our approach, the thresholds for the segmentation of the EEG in the spike train detection are derived from the data (by adaptive thresholding). Similarly, in the oscillation detection, the algorithm references to the background EEG. The remaining fixed thresholds are the correlation between the segments and the features derived from the autocorrelation. However, these parameters are independent of the variability of the seizures, because they only exploit the repetitiveness of the seizures and are independent of the actual seizure shape.

The sensitivity of the combined algorithms was good ($SensT_PP$ 88.3%, $SensT$ 91.1%) at a practically acceptable false positive rate of 0.58 FP/h and PPV_num of 84.9% and PPV_dur of 92.7%. The fact that PPV_dur is higher than PPV_num means that the false positive detections are in average much shorter than the true positive detections. The results for the seizure burden are with $SBdet_PP$ equal to 68.6% and $SBdet_Tot$ equal to 67.1% reasonably good. While this value might seem considerably lower compared to the other performance measurements, in fact this is not the case. As some seizures are missed (almost 10%), the seizure burden due to these is missed completely, which has a big impact on the seizure burden sensitivity. Of the seizures that are detected it is impossible

to get 100% seizure burden detection. The algorithms are focussed to detect those parts of the seizures that are most repetitive. Yet, not every second of the seizure burden is repetitive. For many seizures the very beginning and end are more buried in the background EEG and therefore more diffult to detect.

For comparison, the algorithm by Navakatikyan et al. [143] reported sensitivities of 83-95%. PPV_num of 48-77% and 2 FP/h. The algorithms of Gotman [68] and Liu were also evaluated by Navakatikyan et al. In their evaluation, the sensitivity of the Gotman algorithm ranged between 39.3 and 87.9%, and for the Liu algorithm between 97.9 and 99.2%. However, the false positive rate for the Gotman algorithm ranged from 7.4 to 10.4 FP/h, and an even higher 15.7 FP/h for the Liu algorithm. Faul et al. [58] have also evaluated the performance of the Liu and Gotman algorithms. They reported a sensitivity of 62.5% for the Gotman algorithm and 42.9% for the Liu algorithm. Unfortunately, no FP/h measure was given.

When the 6 channel electrode configuration is used, the $SensT$ is equal to 70.9%. Note that this is actually an unfair comparison as the performance of the algorithm on 6 channels is compared to the analysis of the human observer with 17 channels available. The drop in sensitivity to 17 channels is roughly 20%, which is a good results considering 11 channels were dropped. More importantly is the drop in FP detections. Only 0.097 FP/h compared to 0.58 for the full EEG. This large drop makes the system very reliable as it gives only 1 Fp detection every 10 hours. The main reason for this improvement is that the frontal electrodes are not used and therefore eye movement artifacts (especially nystagmus) do not lead to false positives.

When the automated detection system has only 2 channels available (C3-4 or P3-P4) the sensitivity drops to respectively 55% and 49%. The FP/h score is extremely low or even zero. Thus the system has almost 100% reliability when running on these 2 channel configurations. We can also compare these results to the sensitivity of CFM analysis on channels C3-C4. Note that the CFM analysis is still a manual analysis in which the CFM trace is analysed by an experienced neonatalogist. The neontalogist analysing the CFM trace obtains a sensitivity of 68% which is considerably higher than the 55% of the automated system. But, the FP rate of the human observer is very high, namely 0.44 FP/h compared to 0.02 FP/h of the automated system. The automated system has no inter/intra observer variability, is fully automated, very robust and can give an alarm at the moment the seizure is occuring. Therefore we think that the drop in sensitivity is largely outweighted by these advantages.

In general, for both algorithms, long, high-amplitude seizures are rarely missed. The algorithms sensitivity is lowest for subtle, short seizures which lack repetitiveness (arrhythmic) (Fig. 4.16). Finally, Figs. 2.16, 2.17 and 2.18 in Chapter 2 illustrate the most important non-biological and biological artifacts in neonatal EEG leading to false positives.

During validation of our methodology, we regularly encountered rhythmic activity in the EEG, detected by the algorithm. The origin of that EEG activity was not always clear, even for the neurologist, by only using the information from the scalp electrodes. In those cases, additional information from the simultaneously recorded polygraphic channels of ECG, respiration, movement sensor or even video were needed to establish that the activity present in the EEG was cerebral in nature or caused by an extra-cerebral source. The polygraphic information can be used to automatically detect or remove artifacts in the EEG. The next chapter will deal with these artifacts by removing them before the actual seizure detection is run.

The present parameter settings are for offline analysis and to obtain maximum sensitivity at an acceptable false positive rate. These values are based on expert estimation and trial and error. It is nearly impossible to estimate the parameters in a more systematic approach (e.g. using ROC-curves). Because there are many parameters, which are dependent of each other, we would need an almost infinite amount of ROC-curves to define the optimum parameter values. This optimum would also only be optimal for this particular dataset. We think our approach proves the robustness of the algorithm as it is able to perform without extreme optimization of the parameters. In a monitoring environment and recording with a large amount of EEG channels, it might be desirable to obtain a lower false positive rate at the cost of a lower sensitivity. For the spike train type detection algorithm this can be achieved by increasing the threshold on the correlation between the detected segments. For the oscillatory type detection, the thresholds on the autocorrelation may be changed. By tuning these parameters we believe the algorithm to be suitable for online monitoring with sufficient sensitivity and practical false positive rate.

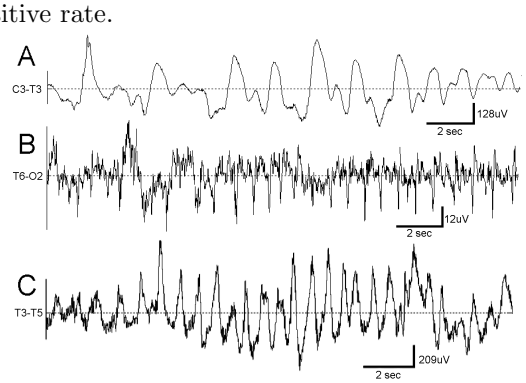

Figure 4.16: *Examples of missed seizures. (A) High-amplitude, arrhythmic oscillatory seizure, (B) short, low-amplitude spike train (complete seizure is shown), (C) hort, focal, high-amplitude seizure (complete seizure is shown).*

Chapter 5

Automated removal of artifacts in the neonatal EEG

In this chapter we introduce the basic frequency filters used in EEG analysis to limit the signal to its most interesting frequency band and suppress power line artifacts. Next we illustrate the decomposition of the EEG using blind source separation for artifact removal. Many neonatal artifacts have similar morphological features as neonatal seizures. This leads to false positive detections by the seizure detector. By removing the disturbing artifacts before the seizure detection is run, we are able to lower the number of false positive detections and thus improve performance. The artifact removal is able to remove the three most dominant types of artifacts that lead to false positives. These are ECG spike artifacts, blood vessel pulsation artifacts and respiration artifacts. We validate the improvement by comparing the seizure detection result on a set of patients with and without artifact removal.

5.1 Frequency filters

5.1.1 Notch Filters

The 50 Hz power line and 100 Hz fluorescent light artifacts can significantly corrupt neonatal EEG. A good feature of these artifacts is that they are very stable in frequency as the power grid is always operating at 50 Hz. Therefore, notch filters can be used to suppress them. Notch filters are frequency filters designed to suppress one specific frequency in the spectrum and thus suitable for this application. Fig. 5.1 shows an example of the effect of the notch filters on the

spectrum of an EEG signal with a 50 Hz and 100 Hz artifact. After application of the notch filters, the artifacts are strongly suppressed.

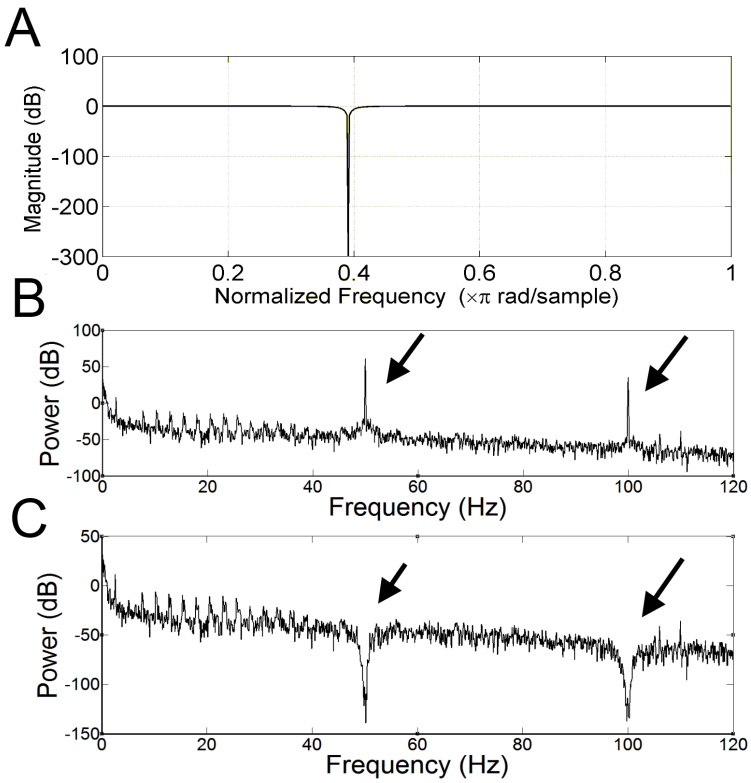

Figure 5.1: *Illustration of the effect of the notch filters. A: Frequency response of the notchfilter at 50 Hz. B: FFT of an EEG signal with 50Hz powerline interference and 100Hz fluorescent light interference. C: FFT of the EEG signal after application of an 50 Hz and 100 Hz notch filter. Both artifacts are now strongly suppressed.*

5.1.2 Finite Impulse Response (FIR) filter

The frequency content of EEG is mainly in between 1 Hz and 30 Hz. Therefore, it is common in EEG analysis to use a highpass and lowpass filter at these frequencies. There are many types of frequency filters available. In this work we choose to use an FIR filter with filter length of 256 samples. The filter is normalized so that the magnitude response of the filter at the frequencies of the passband is 0 dB. This type of filter has good properties for EEG analysis. FIR filters are linear phase and thus do not distort the phase information in the EEG. FIR filters have

no feedback loop and are therefore always stable. The delay of an FIR can be calculated as follows:

$$delay = \frac{(N-1)}{(2 * Fs)} \tag{5.1}$$

with N the length of the filter and Fs the sampling frequency. In our application, N is equal to 256 and Fs is 256 Hz, therefore the filter delay is equal to 0.5 s. In EEG analysis, this filter delay is not so important and does not pose any problems.

5.2 BSS for artifact removal

5.2.1 Introduction

The neonatal seizure detector developed in chapter 4 is (just like any other published seizure detection algorithm) strongly hindered by artifacts in the EEG. This results in false positive detections (Fig. 5.2). To improve the seizure detection and come to a usable and reliable algorithm at the bedside, these artifacts have to be taken into account.
In this work, we focus on the automated removal of artifacts to lower the number of false positive detections of the previously developed neonatal seizure detector without lowering the sensitivity. We will not deal with all types of artifacts as there are far too many and a lot of them are unique to the specific environment in which the EEG is recorded (e.g. artifacts of nearby equipment). We will address the three types of biological artifacts that are, in our experience, the most disturbing ones for automated seizure detection and that are relatively independent of the specific monitoring environment: ECG spikes and blood vessel pulsation and respiration artifacts. These artifacts often lead to false positive detections due to their similar morphology to seizures and repetitive nature (see Fig 5.2). In the classical visual assessment of the neonatal EEG, additional polygraphy signals such as ECG, respiration, movement sensors, etc., are recorded to support the neurophysiologist in recognizing the artifacts. In fact, these combined registrations are the golden standard while recording neonatal EEG [161]. The human observer is able to recognize the artifacts by comparing the EEG to the simultaneously recorded polygraphy signals. In designing our artifact rejection algorithms for the automated processing of the neonatal EEG, we aimed to mimic this behavior.

Because of volume conduction through cerebrospinal fluid, skull, and scalp, EEG signals collected from the scalp are a mixture of neuronal and artifactual activities from multiple brain or extra-brain sources. All these sources have overlapping scalp projections, time courses, and spectra. Therefore, their distinctive features cannot be separated by simple averaging or spectral filtering, and more advanced techniques need to be used. Our strategy for artifact removal is based on Blind

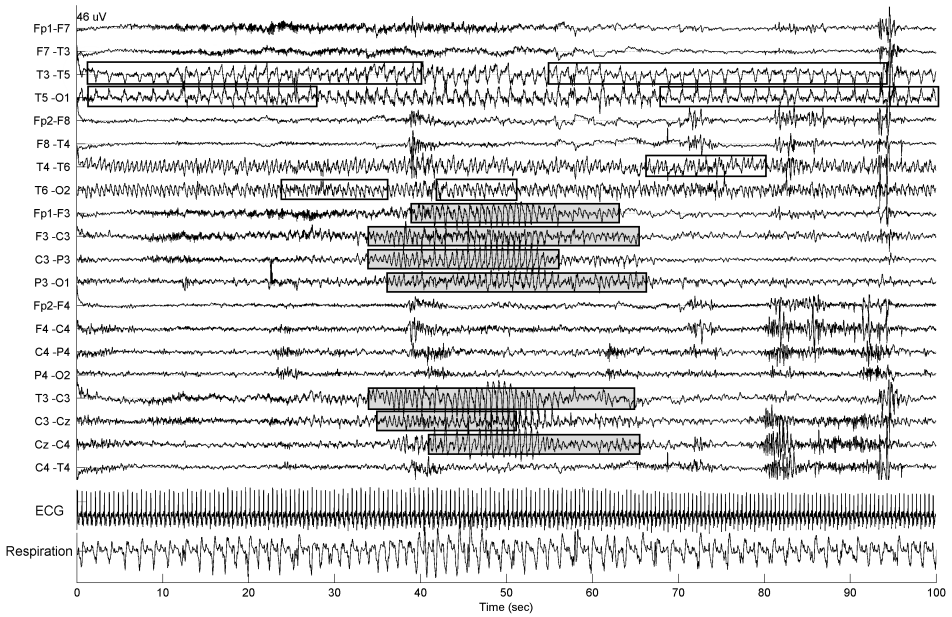

Figure 5.2: *The areas of the EEG delimited by a rectangle are those parts of the signal detected by the seizure detection without artifact removal. Part of the respiration (on channels T3-T5, T5-O1) and pulsation (on channels T4-T6 and T6-O2) artifact is falsely detected as a seizure. The grey shaded areas are true seizure activity. The non-shaded areas illustrate the need for artifact processing in seizure detection.*

Source Separation (BSS) of the complete EEG. The idea of BSS is to decompose the scalp data into the underlying components to capture the independent processes that contribute to the scalp recording. Chapter 3 discusses BSS in greater detail. BSS consists of several subclasses of methods of which Independent Component Analysis (ICA) is probably the most well known. ICA finds an unmixing matrix $\mathbf{W}$ that decomposes or linearly unmixes the multichannel scalp data into a sum of temporally independent and spatially fixed components. ICA does so utilizing higher-order statistical measures. In literature, ICA has shown good results for artifact removal in the EEG [27, 142]. Another BSS method is Canonical Correlation Analysis (CCA) which has proven to be useful to remove muscle artifacts contaminating adult seizure EEG [40]. CCA solves the BBS problem by assuming mutually uncorrelated sources which are maximally autocorrelated [63, 90]. Muscle artifacts have lower autocorrelation in comparison with brain activity allowing good separation. Yet another well known BSS-ICA method is Second Order Blind Inference (SOBI; [9]). SOBI solves the BSS problem using decorrelation across several time points as its basic computational step. This method has proven to be powerful in separating EEG from EOG sources [98].

We start by introducing a general strategy for artifact removal in the EEG using BSS. In the succeeding sections, we modify this general strategy to the specific needs for the removal of each type of artifact, beginning with the ECG spike train removal, followed by the blood vessel pulsation removal and finally the respiration removal algorithm. Finally, we validate the methods by comparing the results of the seizure detection with and without the artifact removal.

5.2.2 Methods

The EEG is first decomposed using an appropriate BSS method into its underlying source components (Fig. 5.3). One or more of these source components may represent an artifact source and needs to be identified. For this purpose, each source component is compared with the simultaneously recorded polygraphy signal that is releveant for the artifact (e.g., the respiration signal for the respiration artifact detection). Correct identification of the artifact component is crucial. If this comparison is too sensitive, too many sources may be omitted resulting in data loss and even missed seizures. If it is not sensitive enough, artifacts may remain in the EEG resulting in false positive seizure detections. An important problem for this identification is that the shape of the BSS source artifact can be remarkably different than the shape of the signal in the polygraphy measurement [196]. Therefore, direct comparison with the polygraphy signals is not possible. For instance, in case of an ECG spike artifact, the QRS complex of the ECG measurement might only be a small bump in the amplitude of the EEG and thus have a very different morphology. To overcome this problem, we add an additional processing step to the sources before the comparison with the polygraphy signal. This step transforms the sources and the polygraphy signal in order to enhance the similar characteristics between them (Fig. 5.3). Once the artifact components are correctly identified, the EEG can be recombined without them, leading to an artifact free EEG.

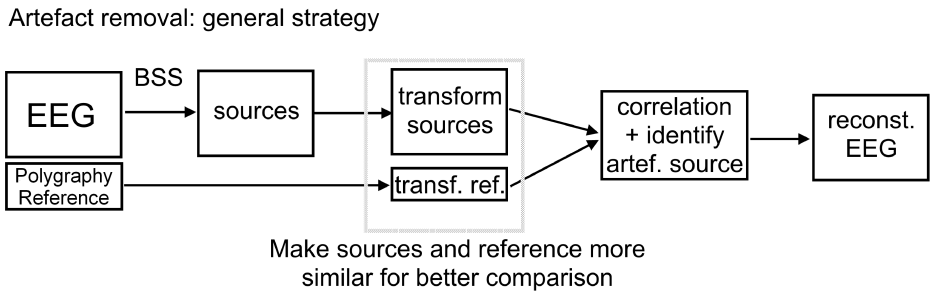

Figure 5.3: *Schematic overview of the artifact removal strategy. BSS estimates the underlying sources in the EEG. The sources and the polygraphy reference are transformed to enhance the similar characteristics between them. The artifact source is then identified. Finally, the EEG is reconstructed without that source.*

ECG spike artifact removal

As a first step toward removal of the ECG spike artifact, we needed to select an appropriate BSS algorithm. It is difficult to evaluate the quality of various BSS algorithms because we have no direct measurement of the source signals at hand that formed the EEG. As selection criterion, we therefore decided to use the BSS algorithm whose assumptions most closely fit that of the artifact to remove. Hence, for the ECG spike artifact, we chose RobustICA. RobustICA is based on the normalized kurtosis contrast function, which is optimized by a computationally efficient gradient-descent technique [225]. It extracts the components one after the other using the deflation approach. The assumption of the robustICA algorithm is that the components are statistically independent at each time point, an approach works especially well to separate non-Gaussian sources. Considering that the ECG artifact is strongly non-Gaussian due to its spiky nature, application of robustICA is justified.

Calculating the direct correlation between the ICA-components and the simultaneously recorded ECG is not optimal as the morphology of the ECG artifact is different from the morphology of the measured ECG. To address this problem, we calculated the correlation between the thresholded energy of the ECG with the thresholded energy of the ICA components. For this purpose, we used a non-linear energy operator (NLEO) as proposed by [99]. The key property of this operator is:

$$\psi[A\cos(\omega_0 n + \phi)] = \frac{1}{2}\omega^2 A^2 \tag{5.2}$$

This indicates that the output ψ of this operator is proportional to the square of both the amplitude A and the frequency ω_0 of the signal. The result is that the

QRS complex of the ECG and the ECG artifact will be amplified relative to the background EEG (Fig. 5.4). Subsequently, the correlation between every energy transformed ICA-component and ECG is calculated. If this correlation coefficient is higher than 0.6, this component was removed from the mixing matrix. Finally, the EEG was reconstructed. Fig. 5.5 shows an example of ECG spike train artifact removal. On Fig. 5.5B can be seen that the artifact removal does not alter the other sharp activity in the EEG.

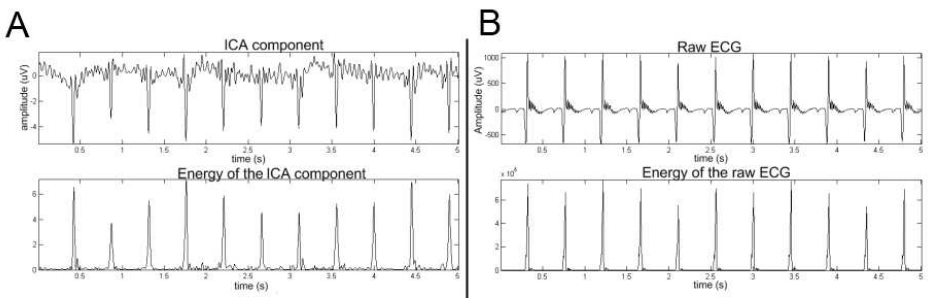

Figure 5.4: *Illustration of the application of the NLEO on the ECG and ICA components. After applying the NLEO, both signals are strongly correlated and the differences related to the morphology of the spikes are removed.*

Blood vessel pulsation removal

RobustICA is not an adequate BSS algorithm for removal of the blood vessel pulsation artifact. A pulsation artifact is a continuous oscillatory type of artifact, which is highly correlated in time but uncorrelated to the other activity in the EEG, and more Gaussian than the spike train of the ECG spike artifact. The strategy of statistical independence based on higher order moments as used by robustICA does not consider relationships across time. Therefore we have used SOBI as BSS algorithm for the problem of pulsation artifact removal. The blood vessel pulsation artifact is an oscillatory artifact strongly correlated with itself and is uncorrelated to the other activity in the EEG. As SOBI separates the data based on its time structure, it is particulary suited for extracting a sine-shaped pulsation artifact [104].

SOBI considers the relationship between component values at different time lags and insists that these values be decorrelated as much as possible. Thus, SOBI uses correlations across time in performing the signal separation. Mathematically, this means that not only the covariance matrix of the sources is diagonal, but also that the covariance matrices at different time lags t+τ are diagonal. As input parameters, SOBI needs the number of sources to be extracted and secondly it needs the maximum time lags for temporal correlations.

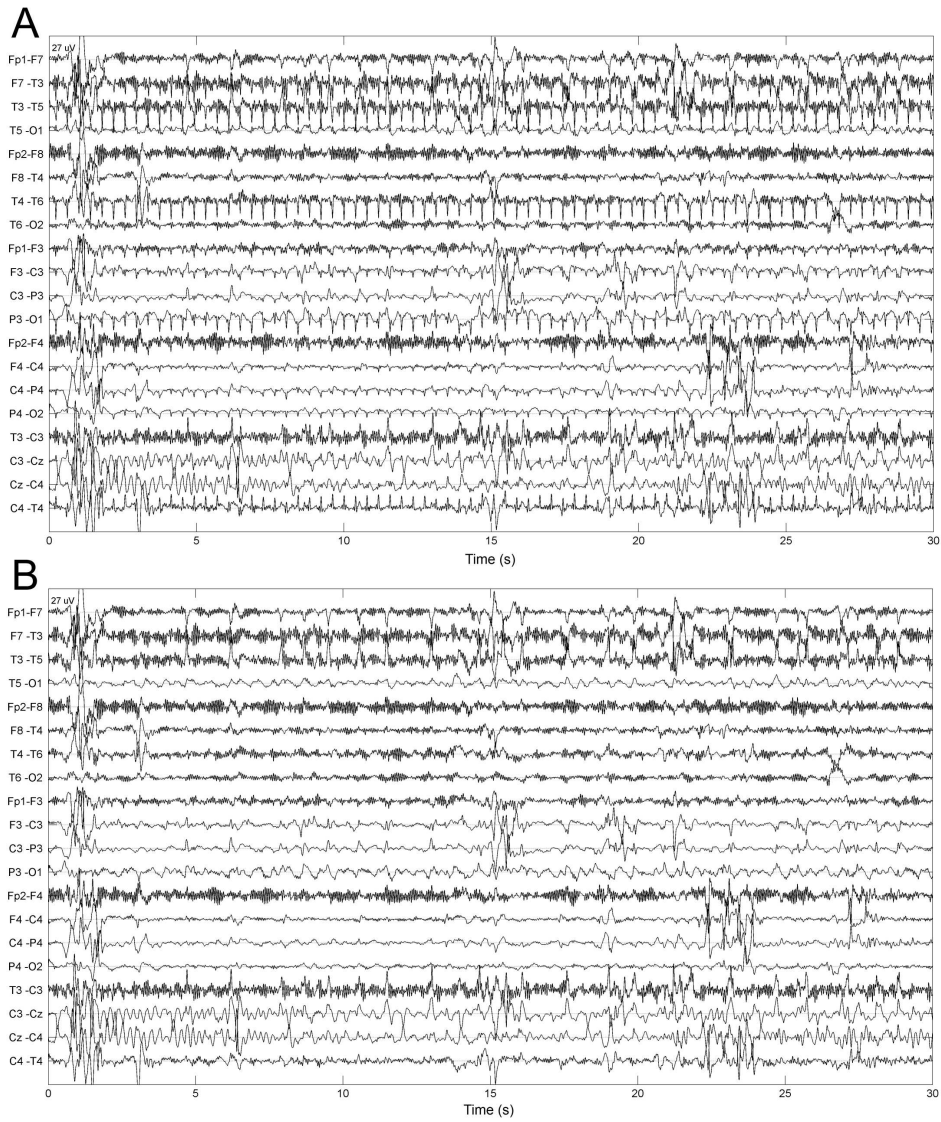

Figure 5.5: *Illustration of the application of the ECG spike train removal. A: EEG with clear ECG spike train artifact (especially on the temporal channels, e.g. T4-T6). B: Reconstructed EEG after ECG spike train removal. The artifact is completely removed without altering other sharp activity in the EEG.*

Because of their shared link to the heart's pump cycle, we may use the simultaneously recorded ECG signal to select which of the source signals is responsible for the pulsation artifact. However, the artifact is oscillatory and the ECG is a spike train signal, implying that we cannot correlate both without further processing. Therefore we filter the ECG signal with a low-pass filter at two times the frequency of the heart rate. The ECG signal now resembles the pulsation artifact much better (Fig. 5.6) enabling a direct correlation and identification of the artifact source. A problem for this approach is the time delay between the ECG and the pulsation artifact that is caused by the time it takes for the blood pressure wave to travel from the heart to the blood vessel causing the EEG artifact. To take this time delay into account, we determined the maximum value of the cross-correlation between the filtered ECG and the BSS-sources. If this correlation is higher than 0.4, the corresponding source was removed from the recombination of the EEG.

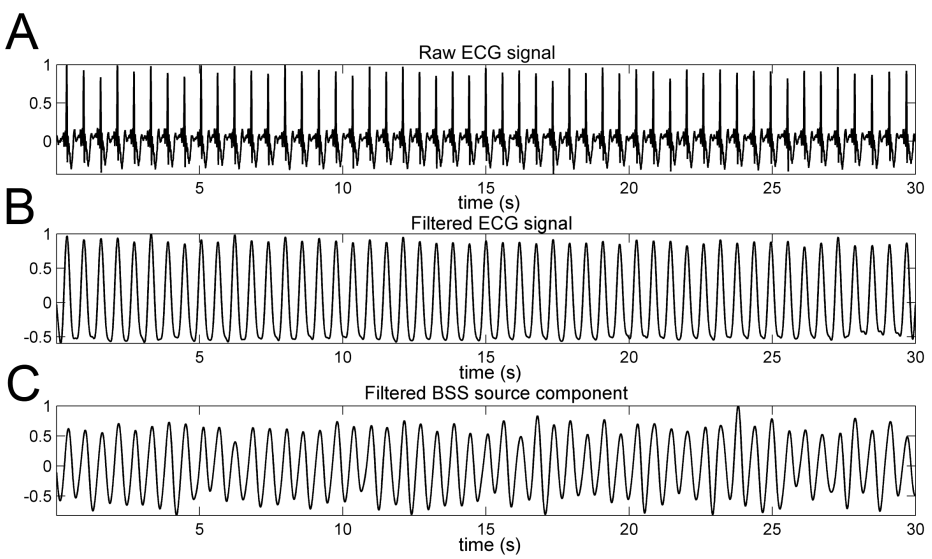

Figure 5.6: *The raw ECG signal is high pass filtered at 2 times the average heart rate of the interval to enhance the similarity with a pulsation artifact. The BSS source components are filtered at the same filter settings. The BSS source component shown in the figure is highly correlated with the filtered ECG signal and will be removed from the recombination.*

Respiration artifact removal

In the previous section about blood vessel pulsation removal we used SOBI as a tool to estimate the artifact source. The respiration artifact shares many morphological features with the blood vessel pulsation artifact as it is also an oscillatory signal

with high autocorrelation. Accordingly, SOBI is also adequate to extract this signal from the EEG. For respiration artifact removal, the estimated sources were compared to the signal generated by a movement sensor on the abdomen of the baby measuring the respiration. To enhance the similarity between the sources and the reference, both are low pass filtered to 9 Hz. If the correlation between the source and the reference is higher than 0.4, the source was removed from the recombination.

Fig. 5.7 illustrates the application of both the pulsation and respiration artifact removal on seizure EEG. Note that after artifact removal, the seizure activity is not affected even though the morphology of the seizure is similar to the artifacts.

Number of BSS components

As input parameters, SOBI needs the number of sources to be extracted and the maximum time lags for temporal correlations. Particularly the estimation of the number of sources is not straightforward, because we do not know how many of them are present in the EEG. Yet, this number is known to affect the quality the ICA solution. When more sources are estimated than there really are, ICA algorithms tend to 'overfit' which leads to distortions [92]. A generally accepted method to define the number of active sources is to make use of a PCA of the data covariance matrix of the EEG [94]. Then the number of dominant eigenvalues provides an estimate of the number of active sources in the EEG. More specifically, we defined that the number of eigenvalues that explain 95% of the variance is equal to the number of active sources and, hence, the number of sources SOBI must estimate. In this way, the number of sources to be extracted is automatically adapted to the complexity of the EEG and the number of EEG channels available.

Combination of artifact removal with the automated seizure detection

The previously developed automated seizure detector works on windows with a length of 30 s. The automated artifact removal presented in this chapter is applied to this 30 s window before the seizure detection is run. The number of time points of n-channel data used in the decomposition must be sufficient to learn the n^2 weights of the unmixing matrix. In literature, it is recommended to have at least some multiple k, of these n^2 number of data points [150]. For a 17 electrode EEG in a bipolar montage of 20 EEG channels and a complex EEG pattern, the absolute minimum number of samples ($k = 1$) is: $1 * 20^2 = 400$ samples. At a sampling frequency of 256 Hz, this leads to a minimum window size of 1.6 s. For complex EEG patterns, with many active sources, k can be as high as 20 leading to a minimum window duration of 30 s. In our application k should always be lower than 20, thus the 30 s long windows supply the BSS algorithms with sufficient

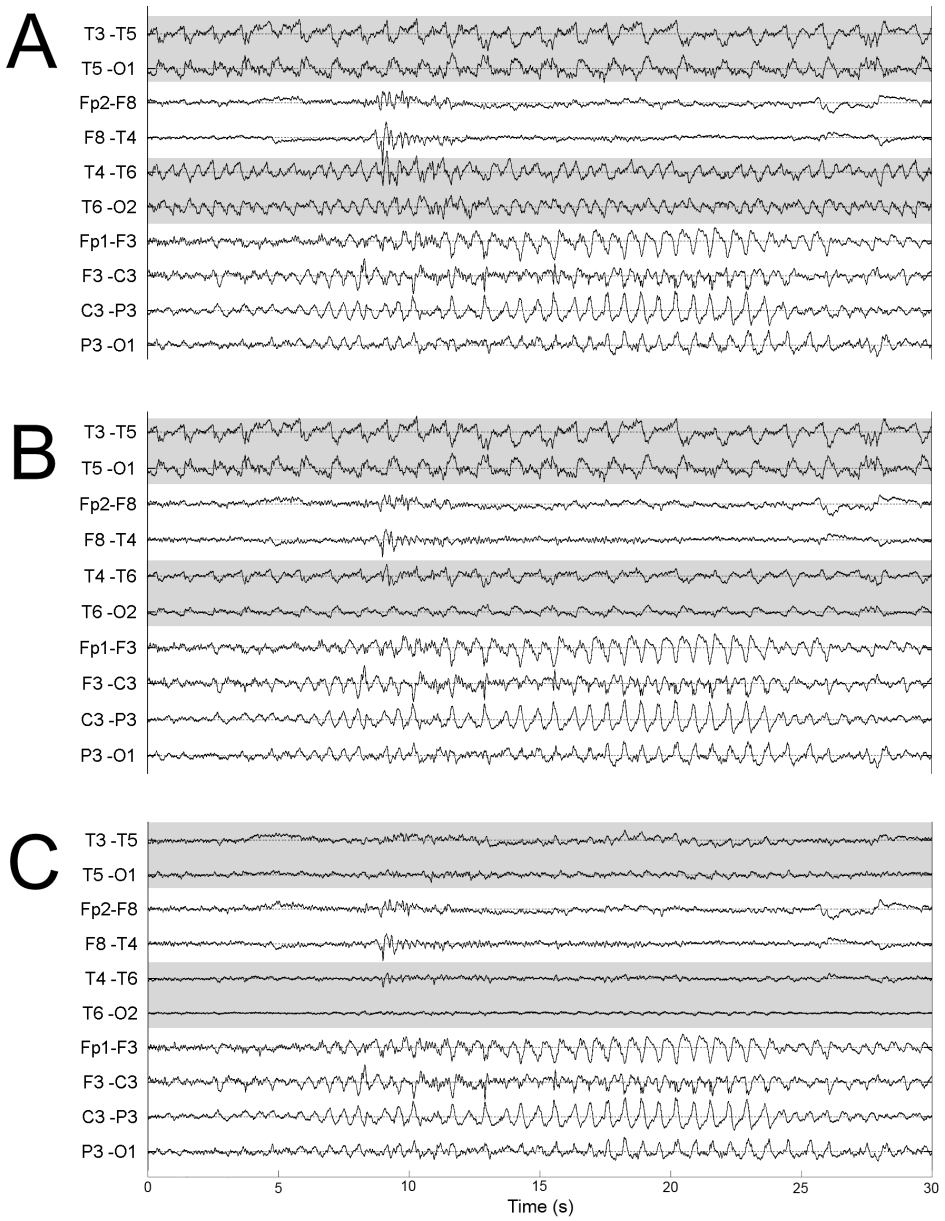

Figure 5.7: *Illustration of the application of the pulsation and respiration artifact removal on seizure EEG. A: Raw EEG with seizure activity on channels Fp1-F3, C3-P3 and P3-O1; respiration artifact on channels T3-T5, T5-O1 (marked in grey); pulsation artifact on channels T4-T6, T6-O2 (marked in grey). B: Reconstructed EEG after pulsation artifact removal. The pulsation artifact is completely removed, some additional respiration artifact becomes visible on channels T4-T6, T6-O2. C: Reconstructed EEG after respiration artifact removal. Both artifacts are now completely removed (compare with Fig. 5.7A) while the seizure activity is not affected.*

samples to reliably separate the artifact signal from the other concurrent EEG activity and are even adequate for a relatively slow signal such as the respiration.

Because we intend to use the automated seizure detector at the bedside, the artifact removal algorithm requires a real-time implementation. The computational requirements of the BSS algorithms are important and may be a limiting factor in the selection of the best BSS algorithm. At present, to ensure real-time operation, RobustICA was limited to 1000 iterations and for SOBI; the number of correlation matrices to be diagonalized was set to 256 samples (or 1 s with a 256 Hz sampling rate).

5.2.3 Results

The dataset used is exactly the same as the one used for testing the seizure detector in the previous chapter. The only difference here is that prior to seizure detection, the EEG is first preprocessed by the artifact removal algorithms. The results of the seizure detection with artifact removal enabled are shown in Table 5.2. These results can be compared to the seizure detection without artifact removal shown in Table 5.1. Table 5.1 is identical to Table 4.1 in Chapter 4 but repeated here for ease of comparison.

Figs. 5.8, 5.9, 5.10 display the box-whisker plots of the $SensPP$, $SBdef$, PPV_num, PPV_dur and FP/h measurements for the results with and without artifact removal. These plots help to identify the dispersion in the results and spot outliers.

	Seizure detection sensitivity			FP measurements			PPV measurements		Seizure burden sensitivity	
Patient	**SZtotPP**	**SZdetPP**	**SensPP (%)**	**FP_num**	**FP/h**	**FP_dur (s)**	**PPV_num (%)**	**PPV_dur (%)**	**SBtot (s)**	**SBdet (%)**
1	26	26	100	43	5.375	1208	37.7	50.4	1349	91.0
2	67	60	89.6	1	0.125	28	98.4	98.9	3076	85.7
3	24	22	91.7	3	0.375	78	88.0	96.5	2853	76.0
4	5	4	80	8	1	182	33.3	79.6	807	88.2
5	3	3	100	0	0	0	100	100	240	56.7
6	15	15	100	0	0.25	47	88.2	95	1257	70.5
7	31	27	87.1	3	0.375	163	90.0	88.1	1421	84.6
8	17	17	100	0	0	0	100	100	2497	69.0
9	4	3	75	0	0	0	100	100	328	55.8
10	9	9	100	0	0	0	100	100	6961	90.7
11	24	24	100	8	1	144	75.0	94.7	3380	75.9
12	5	1	20	0	0	0	100	100	145	37.2
13	11	11	100	19	2.375	447	36.7	73.9	1416	89.3
14	7	6	85.7	0	0	0	100	100	7390	9.6
15	11	9	81.8	7	0.875	136	56.3	73.3	659	56.6
16	12	12	100	1	0.125	23	92.3	98.8	3080	62.4
17	11	11	100	1	0.125	27	91.7	98.9	3406	72.3
18	20	18	90.0	0	0	0	100	100	2255	60.1
19	54	47	87.0	2	0.25	22	95.9	99.4	4309	82.4
20	3	2	66.7	0	0	0	100	100	835	70.2
21	2	2	100	0	0	0	100	100	678	57.4
		91.1% SensT	**88.3% SensT_PP**		**0.58 FP/h**		**84.9% PPV_num**	**92.7% PPV_dur**	**67.1% SBdet_Tot**	**68.6% SBdet_PP**

Table 5.1: *Seizure detection results without artifact removal.*

	Seizure detection sensitivity			FP measurements			PPV measurements		Seizure burden sensitivity	
Patient	**SZtotPP**	**SZdetPP**	**SensPP (%)**	**FP_num**	**FP/h**	**FP_dur (s)**	**PPV_num (%)**	**PPV_dur (%)**	**SBtot (s)**	**SBdet (%)**
1	26	26	100	0	0	0	100	100	1349	86.2
2	67	60	89.6	1	0.125	28	98.4	98.9	3076	85.0
3	24	22	91.7	3	0.375	78	88.0	96.5	2853	75.8
4	5	4	80	7	0.875	168	36.4	80.9	807	88.0
5	3	3	100	0	0	0	100	100	240	56.7
6	15	15	100	0	0	0	100	100	1257	65.1
7	31	28	90.3	0	0	0	100	100	1421	67.1
8	17	17	100	0	0	0	100	100	2497	70.6
9	4	3	75	0	0	0	100	100	328	45.4
10	9	9	100	0	0	0	100	100	6961	90.7
11	24	24	100	0	0	143	75.0	94.7	3380	75.8
12	5	1	20	0	0	0	100	100	145	37.2
13	11	11	100	15	1.875	442	42.3	73.5	1416	86.7
14	7	6	85.7	0	0	0	100	100	7390	10.0
15	11	10	90.9	4	0.5	98	71.4	80.2	659	60.4
16	12	12	100	2	0.25	38	85.7	97.8	3080	55.9
17	11	11	100	0	0	0	100	100	3406	71.0
18	20	18	90.0	0	0	0	100	100	2255	58.4
19	54	54	87.0	10	1.25	249	82.5	92.5	4309	71.2
20	3	2	66.7	0	0	0	100	100	835	72.3
21	3	2	100	0	0	0	100	100	678	52.9
		93.6% SensT	**88.9% SensT_PP**		**0.25 FP/h**		**89.5% PPV_num**	**96.0% PPV_dur**	**64.6% SBdet_Tot**	**65.8% SBdet_PP**

Table 5.2: *Seizure detection results with artifact removal.*

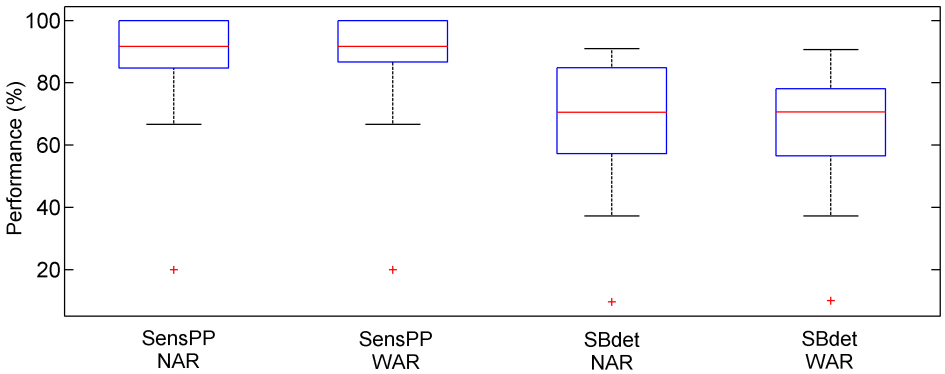

Figure 5.8: *Boxplot results of the SensPP and SBdet performance measurements of the seizure detection with (WAR) and without (NAR) artifact removal.*

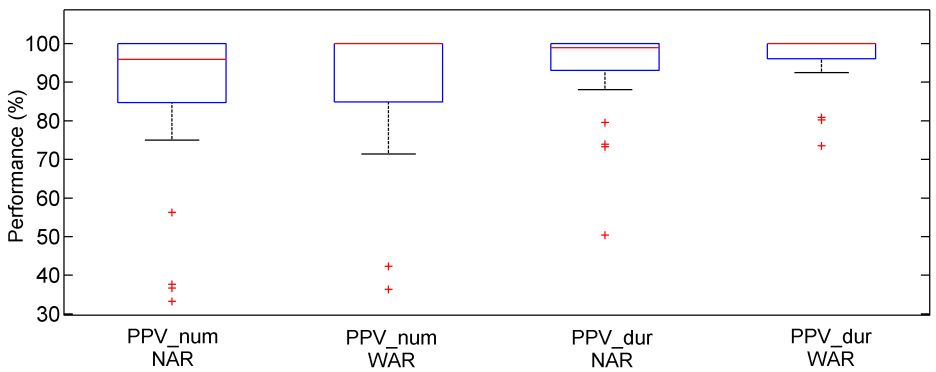

Figure 5.9: *Boxplot results of the PPV_num and PPV_dur performance measurements of the seizure detection with (WAR) and without (NAR) artifact removal.*

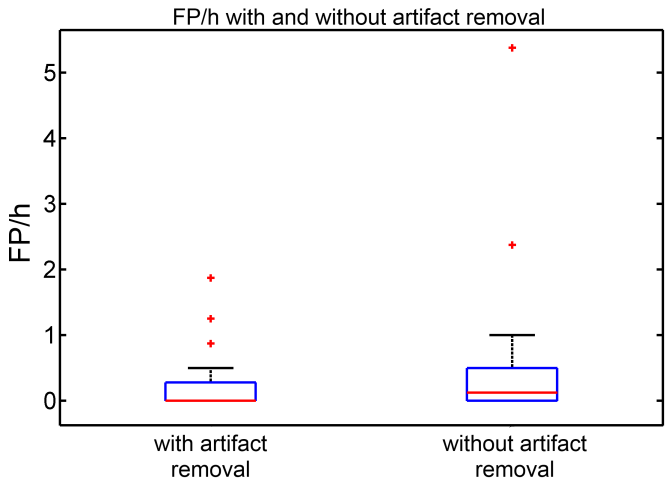

Figure 5.10: *Boxplot results of the number of FP/h for seizure detection with and without artifact removal.*

5.2.4 Discussion

In this chapter, we introduced an artifact removal strategy based on ICA-BSS to remove three types of artifacts from the neonatal EEG. These artifacts are ECG spikes, blood vessel pulsation and respiration activity. These hinder the automated seizure detector developed in chapter 4 and need to be removed. Our main goal was to reduce the number of false positive detections caused by these artifacts without lowering the sensitivity to detect the true seizures. This goal has been achieved. The number of FP/h has dropped dramatically (from 0.58 to 0.25 FP/h), a reduction that is important because it makes a big difference in a practical situation where a nurse needs to check the neonate every time an alarm sounds. The sensitivity to detect the neonatal seizures was not reduced; in fact, it improved slightly ($SensT$ from 91.1% to 93.6% and $SensT_PP$ from 88.3% to 88.9%). This can be explained by the fact that artifacts may mask seizure activity. In those cases, artifact removal facilitates the seizure detection.

Concomitant to the reduction in FP/h, the PPV values for number as well as duration improved (PPV_dur from 92.7% to 96.0% and PPV_num from 84.9% to 89.5%), but the sensitivity to detect the seizure burden was slightly reduced ($SBdet_Tot$ from 68.6% to 65.8% and $SBdet_PP$ from 68.6% to 64.6%). This indicates that some seizure activity has been incorrectly removed by the artifact removal process. The impact is small, however, and probably not significant in a practical situation. Furthermore, in our opinion this disadvantage is outweighed

by the increased sensitivity for seizures discussed above. For clinical purposes, it appears to be preferable to detect more seizures with less seizure burden than the other way around.

The artifact removal is a strong benefit for patients 1, 6, 7 and 11 as for these patients the number of FP's drops to zero. For patients 4, 13, 15 and 17 the artifact removal is a slight benefit as for these patients the number of FP's is slightly reduced. Unfortunately there are also 2 patients where the number of FP's rises, namely patients 16 and especialy 19. For the remaining 11 patients, the artifact removal has no effect on the number of FP's.

When an artifact is detected, we can inform the user of the monitor. Because it is possible to show on which channel the artifact occurred, this user is able to adjust the electrode configuration (e.g., when an electrode is close to a blood vessel) or reposition the neonate to eliminate the artifact.

There are more artifacts in the EEG than the ones we deal with in this chapter. The most important remaining artifacts are eye movements (mainly nystagmus or pathologically fast eye movements) and tremor artifacts. Eye movements are relatively easy to recognize as they are always strongest on the frontal EEG channels (see Fig. 5.11, , the spatial distribution shown is obtained using the SP-CP localization method described in the next chapter). If the EOG is simultaneously measured, identification is even easier. Tremor artifacts pose more of a problem. In our measurements, a movement sensor was fixed to one of the neonate's limbs. In case of a tremor artifact, this sensor's signal has a high correlation with the artifact in the EEG. Therefore, it can be used to identify and remove the tremor artifact with a similar strategy as used in this paper. The problem is that this strategy does not work when the seizure is clinical and the limb movements of the neonate are related to the seizure: in that case, the removal of the artifact would lead to the simultaneous deletion of the seizure activity.

In conclusion, we can say that the artifact removal as used in this paper is a beneficial addition to our automated seizure detector. For patients without artifacts, the artifact removal has no meaningful negative impact on the detector's performance. For patients with artifacts, the artifact removal halves the number of false positive detections, rendering the algorithms usable for continuous bed-side seizure monitoring. Yet, we must warn that in excpetional cases it may happen that the number of FP's rises due to the artifact removal. Therefore, we advice not to enable artifact removal as standard, but only enable it in the presence of corrupting artifacts.

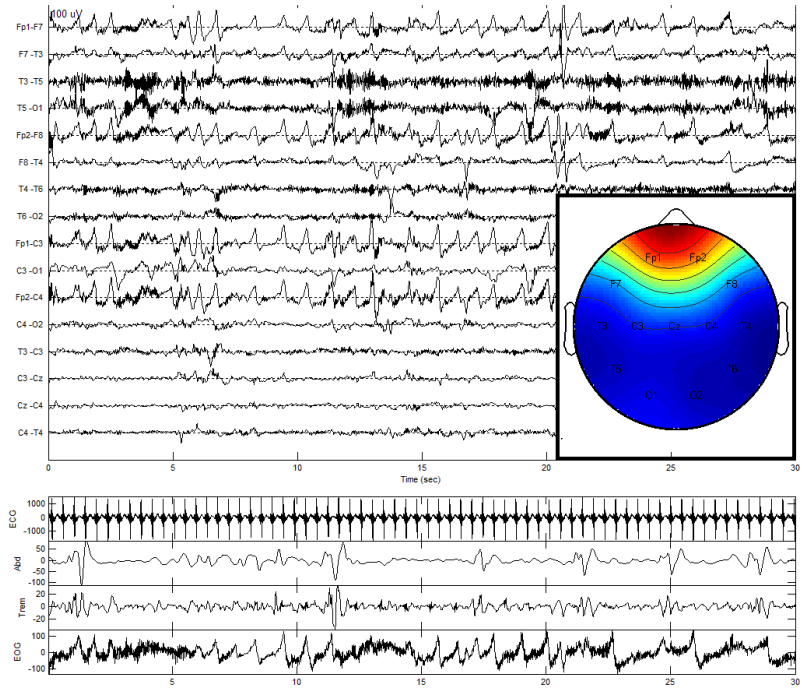

Figure 5.11: *Example of nystagmus eye artifacts, observe the correlation with the simultaneously recorded EOG at the bottom of the figure. The topographic plot shows the spatial distribution of the detected eye blinks on the scalp. The detected activity clearly localizes on the frontal electrodes, making identification as an artifact relatively easy.*

Chapter 6

CPA for neonatal seizure localization

This chapter describes the development of an automated neonatal seizure localization method based on CPA. A separate localization algorithm for the two types of neonatal seizures (spike train and oscillatory) is developed. Both algorithms are able to provide a spatial localization of the seizure on the scalp which can be visualized to the user using topographic plots.

6.1 Introduction

In this work, a robust and objective localization method for neonatal seizures was developed. The method is based on Canonical Decomposition (CANDECOMP), also known as Parallel Factor Analysis (PARAFAC), often referred to as the CP (CANDECOMP/PARAFAC) decomposition. Most decomposition methods applied to EEG, such as, PCA (Principal Component Analysis) [109], ICA (Independent Component Analysis) [157], and CCA (Canonical Correlation Analysis) [40], can only be applied to 2-dimensional data arrays. With CP-decomposition, it is possible to decompose higher dimensional data arrays or tensors [193].

The CP decomposition for EEG analysis was introduced fairly recently [134]. Subsequent work [2, 43] has shown that the CP decomposition can provide a reliable estimate of the epileptic seizure onset zone in the EEG of adults, even in the presence of disturbing artifacts. In the present paper, we propose two methods based on CP decomposition to localize the neonatal seizures. The first one is based

on previous work in the literature and used to localize the oscillatory seizures as detected by the seizure detector. For convenience, in the remainder of this paper, we will refer to this method as O-CP (Oscillatory CP). The second one is a new method specialized in localizing the spike train type of seizures. This method employs the output of the previously developed spike train detector [46] and will be referred to as SP-CP (SPike CP).

6.2 Methods

We start by introducing the CP decomposition (6.2.1). We then describe the O-CP (6.2.2) and the SP-CP methods (6.2.3) in detail. Next, we describe the existing spike triggered averaging method [8, 15] (6.2.4) and compare the performance of this method to the new SP-CP method. We illustrate the application of both methods to localize neonatal seizures (6.3.1 and 6.3.2). By means of simulations, we compare the robustness to noise of the SP-CP method with that of spike triggered averaging (6.3.3).

6.2.1 CP decomposition

CP decomposition models the variance in the tensor as well as possible with a predefined number of trilinear structures. As we would like each trilinear structure to represent a distinct brain source, it is important that the sources we want to extract from the tensor are adequately modeled with such a trilinear structure. Otherwise, the CP decomposition will not be able to separate them. Basically, the trilinear structure allows us to catch three aspects of seizure activity that differentiate it from background activity. In addition to the EEG channels involved (localization of the seizure) and the time (time course of the seizure), we use the third dimension to characterize the oscillatory (for O-CP) or repetitive (for SP-CP) nature of the seizure. The two methods presented in this paper differ in the construction of the third dimension of the tensor, as they need to extract a different type of activity (oscillations as opposed to spikes).

6.2.2 O-CP decomposition method

This method is designed to localize the oscillatory type of neonatal seizures. The seizure needs to be completely separated from all other concurrent EEG activity which might also be oscillatory. We will show that the way we construct the tensor makes the trilinear structure of the CP decomposition suitable for localizing oscillatory sources as reflected in the scalp EEG.

The third dimension of the tensor is constructed using the continuous wavelet transform of the ongoing EEG recording [134] (Fig. 6.1). Consequently, the tensor consists of the dimensions channels, time, and frequency. We computed the decomposition on the 'pure' wavelet-transformed EEG in contrast to previous studies, where the CP decomposition was calculated using the power (square) of the wavelet-transformed EEG.

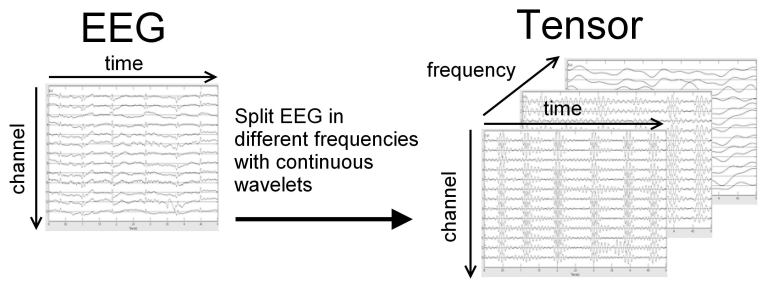

Figure 6.1: *Illustration of how the EEG is split up in to a set of frequency components to build the 3D tensor.*

The wavelet transform is chosen for its optimal time-frequency resolution. Wavelets resolve high frequency components within small time windows and low frequencies in larger time windows. The continuous wavelet ϕ at scale a and time t of a signal $x(t)$ is defined by

$$C(a, time) = \int_{-\infty}^{\infty} x(t)\phi(a, time, t)dt \tag{6.1}$$

with ϕ the chosen wavelet. In this study, we used a biorthogonal wavelet. The exact choice of the wavelet does not really affect the result. From the scale a of the wavelet, the frequency of the signal can be estimated as:

$$f = \frac{f_c}{a\Delta t} \tag{6.2}$$

with f_c the center frequency of the wavelet and Δt the sampling period. We took those frequency components that had a center frequency ranging from 1Hz up to 30 Hz with a step of 1 Hz. The corresponding wavelet scale a for each of these frequency components was calculated using Eq. 6.2. This means that the tensor was constructed using wavelet coefficients with a linear increase in center frequency instead of using coefficients with a linear increase in scale a. If we had chosen the frequency components to be linear in a, the tensor would have contained mainly low frequency components, resulting in an unwanted tendency to favor these components in the CP decomposition.

After construction of the tensor as described above, it was decomposed using an R-component CP decomposition. The suitable number of components was

determined by checking the Core Consistency Diagnostic [193]. We found the optimal number of components to be two. Thus, each decomposition led to two trilinear components (Fig. 6.2 for interpretation of the trilinear structure), i.e., two extracted time vectors ($\mathbf{b}_1$ and $\mathbf{b}_2$, see Fig. 6.3A), two spatial distribution vectors ($\mathbf{a}_1$ and $\mathbf{a}_2$) containing the spatial distribution of the extracted time series, and two frequency distribution vectors ($\mathbf{c}_1$ and $\mathbf{c}_2$) representing the frequency content of the extracted time series. For localization purposes, the **a**-components or the spatial vectors containing the distribution weights of the extracted activity over the EEG-channels were the most relevant ones. We visualized this vector using topographic plots that showed the distribution on the scalp.

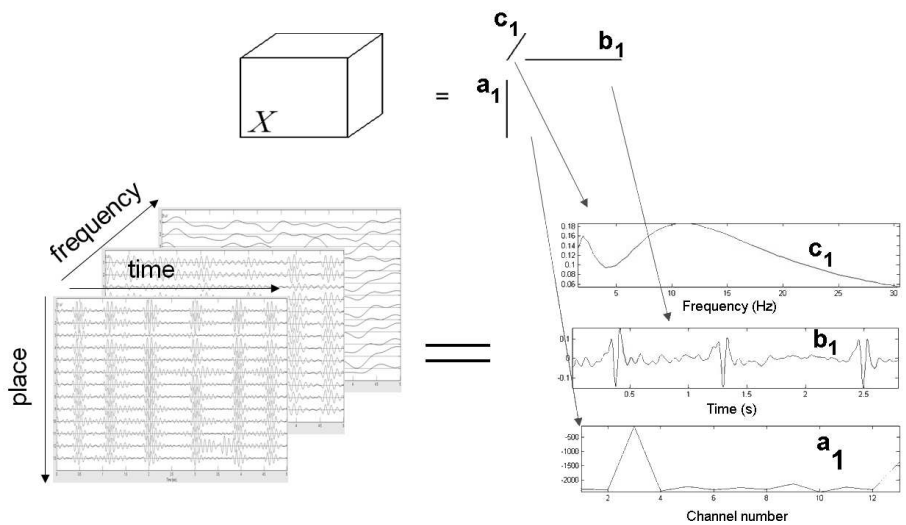

Figure 6.2: *Interpretation of the trilinear structure of the O-CP analysis. Vector* $\boldsymbol{a}_1$ *corresponds to the spatial distribution on the scalp of the activity modelled by the CP analysis. This activity can also be plotted as a topographic map for easier interpretation. Vector* $\boldsymbol{b}_1$ *corresponds to the extracted time information. Vector* $\boldsymbol{c}_1$ *corresponds to the frequency distribution of the extracted activity.*

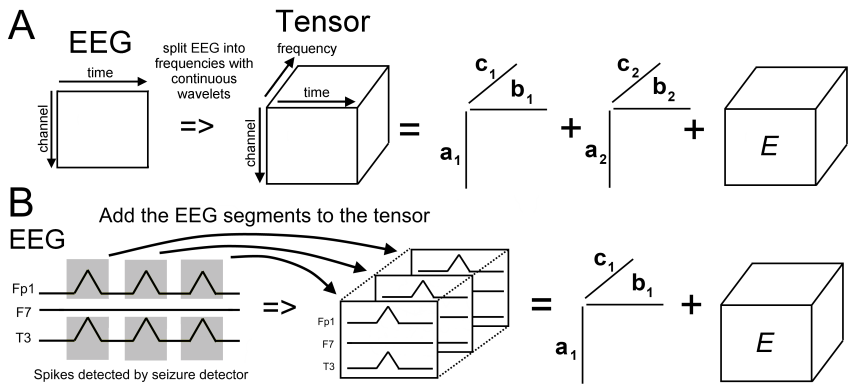

Figure 6.3: *(A) Localization of oscillatory type seizures: The third dimension of the tensor was constructed by decomposing the 2D EEG (channel and time) into a set of frequency components using continuous wavelets. After the tensor is built up, a two-component CP decomposition is calculated. (B) Localization of spike train type seizures: The spikes as detected and segmented by the seizure detector are added to the tensor. After the tensor is built up, a one-component CP decomposition is calculated.*

6.2.3 SP-CP decomposition

This algorithm is designed to localize neonatal spike train-type seizures. Instead of using the complete EEG segment to construct the tensor as in the O-CP method, here we make use of the output of the spike train seizure detector [46]. The output of this detector consists of a series of segmented spikes. The goal is to use all spikes available to robustly localize the origin of the detected seizure. Using multiple spikes is better than single spike localization as the latter is strongly dependent on the signal-to-noise ratio (SNR), that is, the ratio of spike to background EEG amplitudes [8]. The method we developed, based on CP tensor decomposition, analyzes all spikes simultaneously. The first two dimensions of the tensor again are EEG channels and time. Instead of using the frequency information, the third dimension is now built up by aligning all EEG segments (taking all channels) of the detected spikes one after the other in different slices of the tensor (see Fig. 3-B). The third dimension of the tensor thus consists of an aligned set of EEG slices. Before the detected spikes can be added to the tensor, they need to be standardized and properly aligned to each other. This is done by the following procedure:

1. Divide the spike segment by the maximum value of the EEG-segment and subtract the mean over all channels (makes the EEG segment average referenced).

2. Shift the detected segments to align the maximum values of all the spikes to each other.
3. Multiply each detected spike segment with a Hamming window.
4. Add zeros before and after each detected spike segment until the length of each spike segment is equal to the length of the longest segment to be added to the tensor.
5. Arrange all EEG segments after each other to construct the tensor.

The first step is needed to remove the DC-offset on the spikes and differences in amplitude. Only the variation in the morphology of the spike is in our interest. This first step makes the detected spikes more uniform. The zeros added in step 4 are necessary because the lengths of the EEG segments of the detected spikes are not identical. After the zeros are added, each segment has equal length and a proper tensor can be constructed. This addition of zeros has no influence on the outcome of the CP-decomposition and does not distort the localization. The Hamming window in step 3 is necessary because the addition of the zeros would otherwise lead to a discontinuity at the boundaries of the signal. The Hamming window forces the boundaries of the signal to zero, eliminating the gap.

After construction of the complete tensor, it was decomposed with a one-component CP decomposition. We only needed one component as the tensor only contains seizure data. The one component trilinear structure models as much variance as possible in the tensor. The remaining data that cannot be modeled with the single trilinear structure end up in the residual E tensor (Fig. 6.3-B). The resulting **a**-component of the trilinear structure is the spatial distribution we are interested in. The **b**-component is the extracted time series. The **c**-component contains the distribution over the spikes in the tensor. Note that the meaning of the **c**-component for the SP-CP method is different than it was for the O-CP method, in which the third dimension was built up of wavelet coefficients instead of different EEG segments.

6.2.4 Spike triggered averaging

Another well-known method used to localize spikes is EEG 'spike triggered averaging'. This method is widely used to improve the SNR and better localize paroxysmal sharp activity, such as interictal spikes in patients with epilepsy [8] or rolandic sharp waves in neonates [15]. The spatial distribution of the spikes is obtained by taking the value of the amplitude of each channel at the largest peak of the averaged spike EEG. In the results section we compare the SP-CP method with spike triggered averaging and quantify the robustness of both methods to noise.

6.3 Results

6.3.1 Illustration of the application of the O-CP method

We illustrate extraction of oscillatory sources with the O-CP method by applying this method to the EEG presented in Fig. 6.4. This EEG shows two dominant types of activity. Most important is the oscillatory seizure activity on channels T3-C3, Cz-C4, Fp1-F3, and C3-P3. The second strong source is a respiratory artifact on channels T3-T5 and T5-O1, which was verified by its strong correlation with the signal from a sensor on the abdomen.

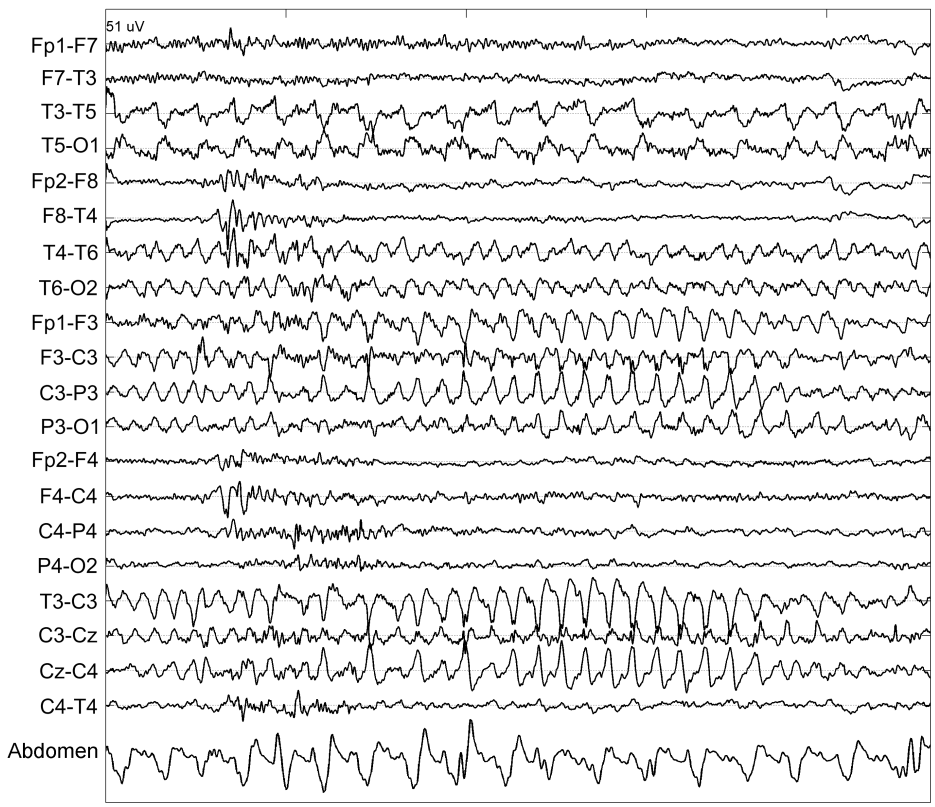

Figure 6.4: *Example of an oscillatory seizure predominantly present on channels T3-C3, Cz-C4, Fp1-F3, and C3-P3. Besides the seizure, a respiratory artifact is present on channels T3-T5 and T5-O1. The artifact was identified by the high correlation with the signal recorded by a sensor on the abdomen.*

The seizure activity needs to be completely separated from the artifact to obtain a reliable localization. Therefore, a two-component O-CP decomposition is calculated, implying that background EEG activity is assumed to end up in the residual variability tensor E (Eq. 6.3). Fig. 6.5-A shows the two extracted **b**-components of the CP decomposition, which correspond to the time series extracted from the EEG (Fig. 6.4). The signal at the top corresponds to the extracted seizure activity, the signal at the bottom to the slower respiratory artifact. Fig. 6.5-B shows the topographic representation of the extracted spatial distributions or **a**-components in the CP-decomposition. Fig. 6.5B-1 corresponds to the location of the left-central seizure activity, while Fig. 6.5B-2 corresponds to the left posterior temporal location of the respiratory artifact. Separation between the two oscillatory sources is possible as they have different spatial and frequency properties, implying that they cannot be accurately modeled with a single trilinear structure. In order to model the variance in the tensor properly, the CP-decomposition must "accommodate" the different oscillations within different trilinear structures.

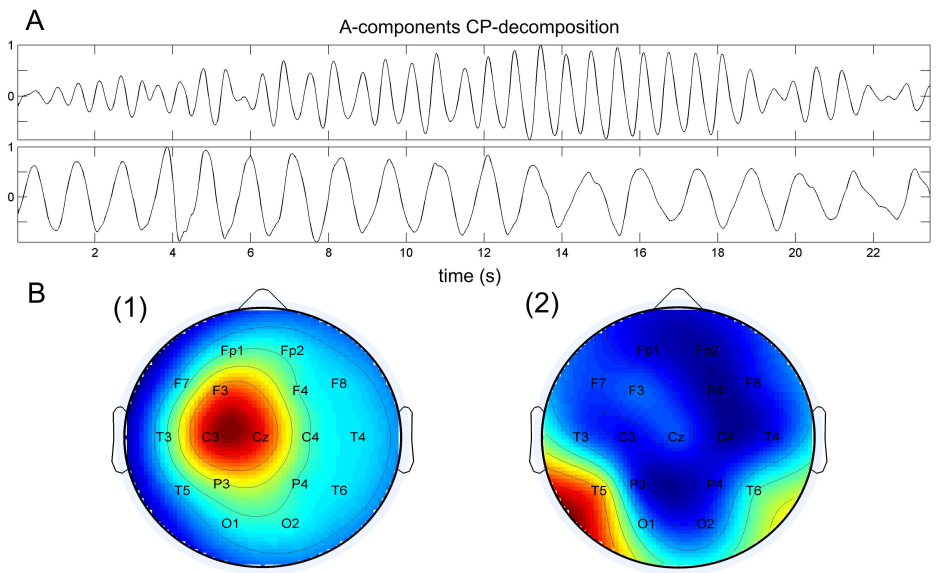

Figure 6.5: *Result of the O-CP algorithm on the EEG in Fig. 6.4. (A) The upper curve is the extracted time course corresponding to the seizure activity and the lower to the respiratory artifact. (B) Topographic plots of the extracted spatial distribution corresponding to (B-1) the seizure activity and (B-2) the artifact activity. Note that the artifact does not contaminate the seizure localization as there is no temporal activity on B-1.*

6.3.2 Illustration of the application of the SP-CP method

The application of the SP-CP method is illustrated by applying it to the EEG and detected spikes displayed in Fig. 6.6. Visual analysis indicates that the spikes originate from the left anterior temporal brain region. The result of the SP-CP algorithm is shown in Fig. 6.7.

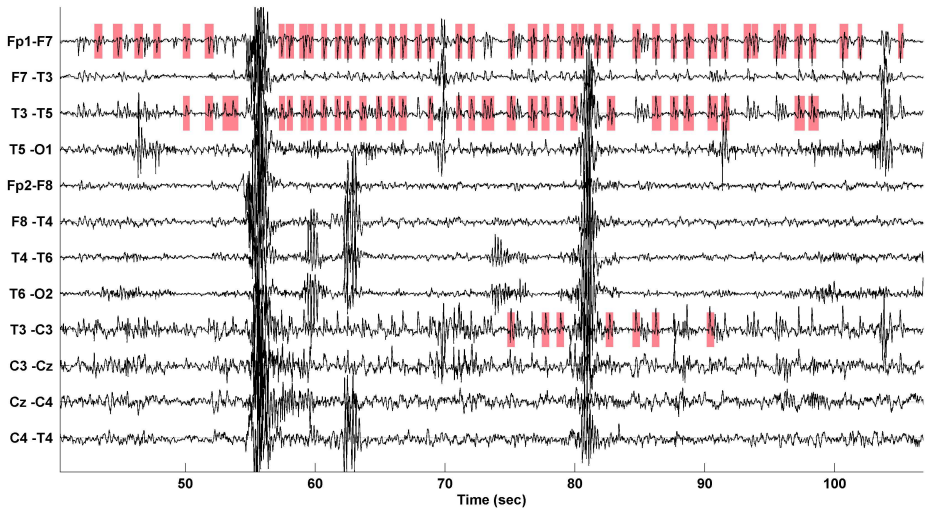

Figure 6.6: *Example of a spike train type seizure and result of the automated detection algorithm. The segments detected by the spike train detection algorithm are marked in grey. The seizure is located on channels Fp1-F7, T3-T5, and T3-C3.*

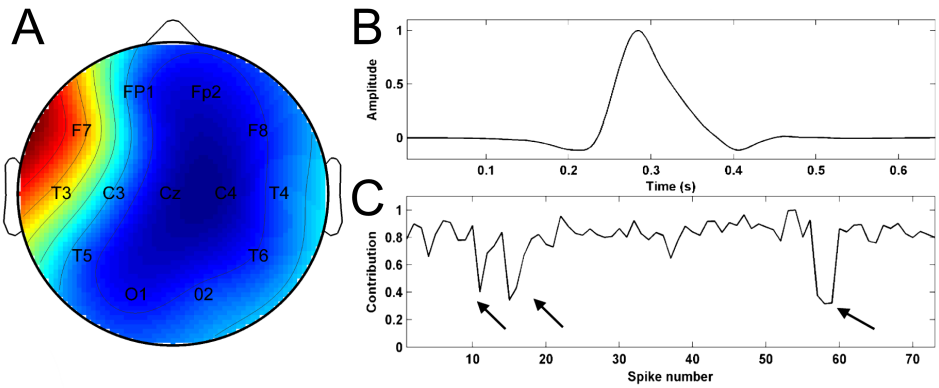

Figure 6.7: *(A) **a**-component of the CP decomposition (see Fig. 6.3(B). The **a**-component corresponds to the spatial distribution of the spikes and can be plotted as a topographic plot. The location of the extracted activity is left anterior temporal. (B) SP-CP extracted time series (**b**-component) with similar morphology to the detected spikes. (C) **c**-component of the CP decomposition. This curve represents the distribution of the extracted time series over all spikes (73 spikes were detected) in the tensor. The arrows indicate the few spikes that have a lower contribution to the extracted time series.*

Fig. 6.7-A is the **a**-component of the CP-decomposition (see Fig. 6.3-B). The **a**-component corresponds to the spatial distribution and can be plotted as a topographic plot. The location of the extracted activity is left anterior temporal, which corresponds to the location obtained by visual analysis of the EEG in Fig. 6.6. Fig. 6.7-B illustrates the **b**-component of the CP-decomposition. This component is the extracted time series and can be viewed as a prototype for the detected spikes. Fig. 6.7-C is the **c**-component of the CP-decomposition. This curve represents the distribution of the extracted time series over all spikes (73 spikes were detected) in the tensor. The arrows indicate the few spikes that have a lower contribution to the extracted time series.

6.3.3 Robustness of the SP-CP method and comparison with spike triggered averaging

The following simulations illustrate the robustness of the SP-CP method in comparison with spike triggered averaging. In the first simulation, we constructed a tensor consisting of 5 identical EEG spike segments. We then replaced the third slice in the tensor by uniform random noise and calculated the CP decomposition of this tensor. The **c**-component of the decomposition is plotted in Fig. 6.8-A. This **c**-component corresponds to the weight of each EEG spike segment to the localization, similar as the **c**-component plotted in Fig 6.7-C. Fig. 6.8-A demonstrates that slices 1, 2, 4, and 5 contribute equally (because they are

identical), but slice 3 (the one with uniform noise) has a contribution that is 50 times lower than that of the other slices. This simulation illustrates that when an EEG slice does not correspond to the global variance in the tensor, it is assigned a very low weight and, hence, a low contribution to the extracted localization. In spike triggered averaging, this is not the case as each spike segment carries an equal weight to the averaged result.

This advantage over spike triggered averaging can be further illustrated by analyzing how both methods behave when noise is added to all slices of the tensor. We measured the influence of the noise by calculating the correlation between the extracted spatial localization (**a**-component) when no noise is added and the one with added noise. When the noise has no influence on the localization, this correlation is equal to 1. The result is shown in Fig. 6.8-B. At high SNR, the spike triggered averaging has comparable performance to the SP-CP method, with the correlation being very close to or equal to 1. However, at an SNR of 0 dB, i.e., when the power of the noise equals that in the spike, the performance of the spike triggered averaging method starts to drop significantly, while the correlation of the SP-CP method remains close to 1.

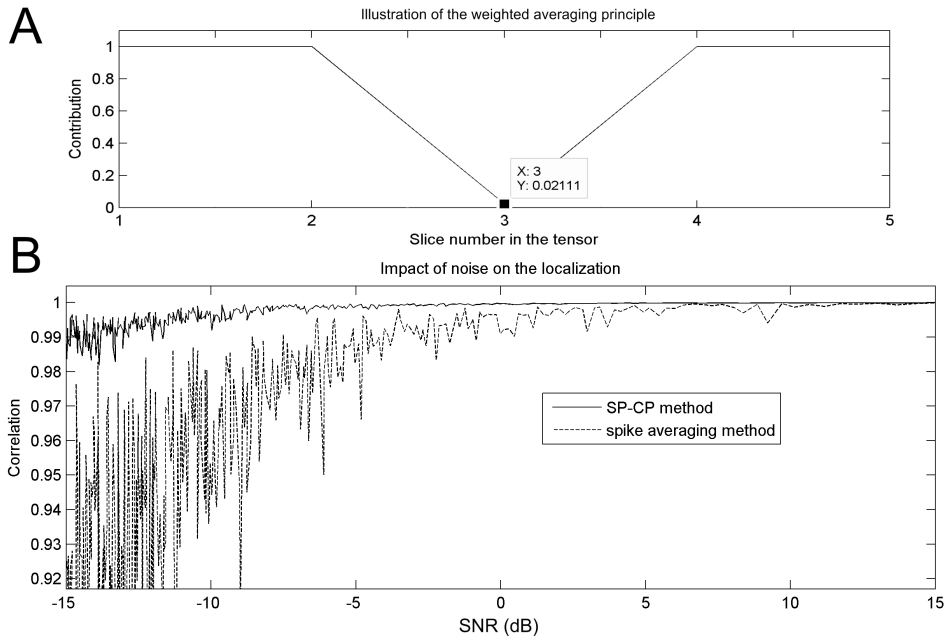

Figure 6.8: *Illustration of the robustness of the SP-CP method. (A)* $\mathbf{c}$*-component of the CP decomposition of a tensor consisting of 4 identical slices (slices 1, 2, 4, and 5) and random noise on the 3rd. The weight of the 3rd slice is very low compared to that of the other slices, indicating that the CP method does not use this slice to model the variance in the tensor. In spike averaging, each slice gets an equal weight. This difference makes the SP-CP method less sensitive to noise. (B) Illustration of the robustness of the SP-CP method to noise added to the tensor. Even at high SNR, the extracted SP-CP localization remains close to the localization without noise (correlation equal to 1). At low SNR, the spike averaging method is much more influenced by the noise than the SP-CP method.*

6.3.4 Comparison with visual analysis of the EEG

Fig. 6.9 shows the topographic plots of 2 seizures for each patient together with a textual indication of the relevant electrode positions defined by visual analysis of the plot. Table 1 shows the results of the visual analysis of the EEG by the clinical neurophysiologist and the visual analysis of the topographic plots (of which Fig. 6.9 shows 2 examples for each patient). Whether the O-CP or SP-CP method is used to localize the seizure is entirely based on the detection by the seizure detector [46]. The EEG trace marked by this detector as seizure EEG is used as input to the respective method without any manual selection. A few seizures were detected by both algorithms. In those cases, both localization methods were used and compared to the visual analysis.

Table 6.1: *Results of the comparison between visual analysis of the EEG by the clinical neurophysiologist and visual analysis of the topographic plots produced by the algorithms.*

Patient	Seizure	Analysis	Location Algorithm	Location Clinical neurophysiologist
1	1	O-CP	O2	O2
	2	SP-CP	P3-Cz, spread C3	P3, spread Cz-C3
	3	SP-CP	P3-Cz	P3-Cz
	4	SP-CP	P3-Cz	Cz
	5	SP-CP	P3-Cz, spread C3	P3-Cz, spread P3
2	1	O-CP	O1	O1
	2	O-CP	C3-Cz	C3-Cz
	3	O-CP	O2	O2
	4	O-CP	O1	O1
	5	O-CP	Cz, spread P3-P4	Cz, spread P3-P4
3	1	SP-CP	Cz-C4	O1
	2	SP-CP	C4-F4, C3-F3, Cz spread T3-F7, T4-F8	C4, spread F8,T3
	3	SP-CP	C3-F3, Cz-C4	Cz-C4, spread F3
4	1	SP-CP	F4-C4, spread Cz, P4	Cz-C4
		O-CP	Cz-C4, spread F4, P4	Cz-C4
	2	O-CP	F3	F3-C3
		SP-CP	F3	F3-C3
5	1	SP-CP	T3-C3	T3
	2	SP-CP	Cz-P4	Cz
	3	SP-CP	Cz-C4	Cz-C4
6	1	O-CP	T3-P3, spread T5-O1, C3	T5-O1
		SP-CP	T3-P3, spread T5-O1, C3	T5-O1
	2	O-CP	T3-T5, C3-P3	T5-O1, spread P3
		SP-CP	T3-T5, C3-P3	T5-O1, spread P3
	3	SP-CP	F4-F8, C4-T4	F8-T4

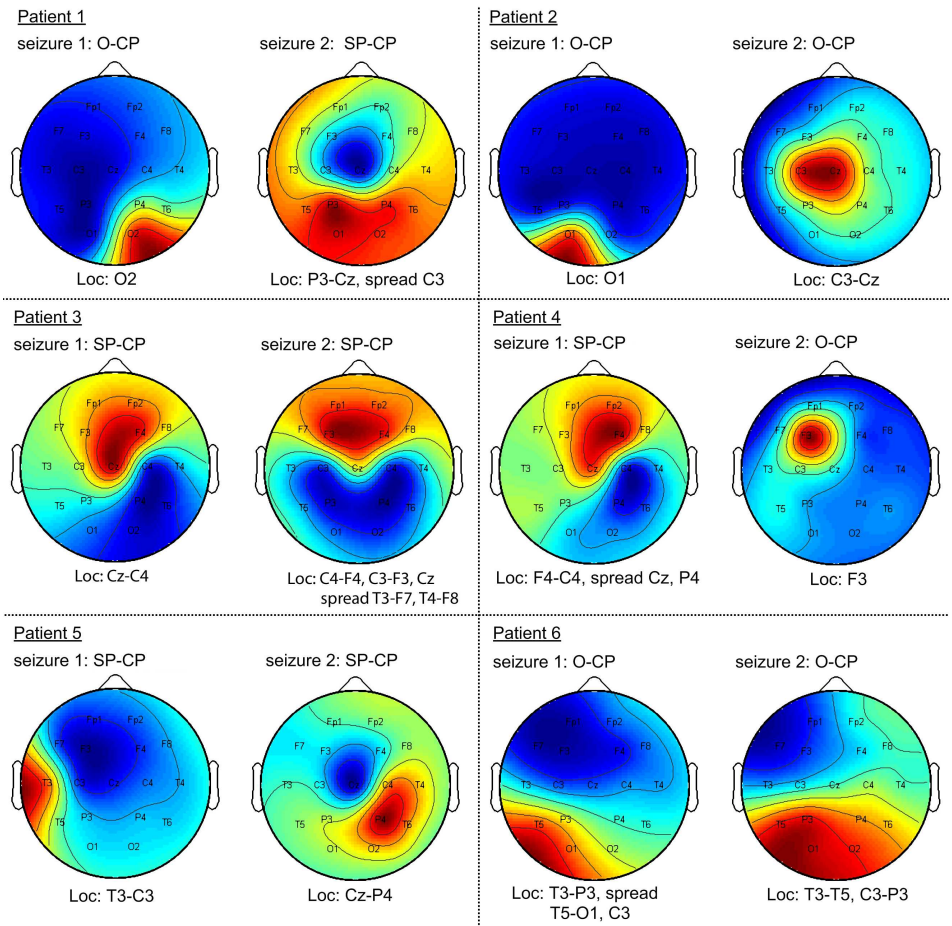

Figure 6.9: *Locations (Loc) of the seizures determined by the topographic plots of the SP-CP and O-CP algorithms (see also Table 1). The algorithm used to localize the seizure is mentioned above each topographic plot.*

6.4 Discussion

In this chapter, we introduce two methods to localize neonatal seizures. Each method was designed to handle a specific seizure type. Both use the CP-decomposition methodology to extract information regarding the localization of the source of the seizure as reflected on the scalp. The O-CP method was designed to extract and localize the oscillatory type of seizures; the SP-CP was designed to localize spike train activity. The two methods use a 3-dimensional tensor in which the first two dimensions are space and time, but differ in the construction of the third dimension. The O-CP method decomposes the EEG into different frequency components, and the SP-CP method constructs the third dimension by arranging all detected EEG spike segments one after the other. Thus, each method uses the specific features of the seizure type it is designed to localize. We also show that these methods can differentiate seizure activity from artifact and the SP-CP method, when compared to simple spike averaging, is resistant to the effect of random noise.

6.4.1 Application of both methods to the same seizure

We used a different localization method for oscillatory and spike train type seizures, based on their morphological characteristics. However, some neonatal seizures consist of a combination of the two seizure types. Those seizures can be localized using either method. In the results shown in Table 1, we have included a number of seizures which were localized with both methods (patient 4, seizure 1, 2; and patient 6, seizure 1, 2). We can conclude that both methods give, as expected, similar results.

6.4.2 Dynamic seizures

The methods assume a fixed localization for the complete window of analysis. This is a potential limitation in case of dynamic seizures that spread or migrate from one brain region to another. Epileptic seizures in adults and older children frequently behave in this way. However, neonatal seizures tend to have a comparatively limited electrographic spread [19, 158]. This is probably because the connectivity between different brain regions is not well-developed in the immature brain [108]. In those cases where there is some spreading of the seizure, it is necessary to divide the seizure in possibly overlapping windows. The CP-decomposition methods should then be applied to each window to localize the seizure more accurately, and to track it in time. Algorithms that enable such tracking have recently described [145]. In case a CP-decomposition is made on a seizure that starts in one brain region and ends in another, De Vos et al [42] proved with simulations that the

CP-decomposition will model the seizure location somewhere in the middle, as one can intuitively expect. Secondly, the active region of the seizure may become larger in time, meaning that the seizure spreads to more neighboring electrodes. This spreading is not a real problem for localization, as the major location of the seizure stays the same; it is only the spread of the seizure to other electrodes that becomes stronger over time.

6.4.3 Interpretation of the topographic plots

If there is a strong difference in polarity visible on the topographic plots (clear difference between positive (red) and negative (blue) brain regions) then the isopotential lines in between those regions indicate the location of the seizure on the scalp (e.g. Fig. 6.9, patient 5, seizure 2 with localization between Cz-P4). Seizures localized to the edge of the topographic map (e.g. Fig. 6.9, patient 1, seizure 1 with localization on O2) have only 1 strongly localized polarity, the opposite polarity is more diffusely distributed as it is directed away from the electrodes. This region of the brain is not encompassed by a complete array of surrounding electrodes thus a sharp cutoff between the two polarities as seen in seizure 1 cannot be obtained. Another situation is when there is a strong polarity expressed close to the midline (e.g. patient 2, seizure 2) without clear difference between opposing polarities. This is because the opposite polarity is directed towards deeper brain regions and thus not visible on a 2D plot. These limitations are introduced due to the way scalp EEG is recorded and not due to limitations of the algorithm.

6.4.4 Comparison between topographic plots and visual analysis of the EEG

Table 1 shows the comparison between the visual analysis of seizures by the clinical neurophysiologist and the topographic plots of the algorithms. This similarity is difficult to quantify, but qualitatively, there is a good agreement between the two methods. For instance, seizure 1 of patient 3 shown on Fig. 6.9 clearly originates from the right side of the brain between channels Cz-C4, while seizure 2 affects both hemispheres. This can especially be of help to non-expert readers of the EEG, such as NICU personnel, who can derive such information much more readily from the topographic plots than by looking at the raw EEG.

6.4.5 Practical applications of the methods

The algorithms presented in this paper can be used in the NICU together with the previously developed seizure detector to form a complete seizure monitoring

system. Such monitoring can yield important prognostic information [164, 165]. E.g. seizure burden, length of seizure discharges [38], number of seizure foci present [18], spread of seizures to contralateral hemisphere [164], etc. It could also be of help in a future scenario of guiding targeted therapies for different types of brain injuries in the NICU. Visually scoring the EEG to obtain this information for use in the NICU is labor-intensive and therefore happens seldom in clinical practice.

Chapter 7

Neonatal seizure localization in a realistic head model.

In this chapter we localize the detected neonatal seizures in a realistic head model. Therefore, the spatial distributions obtained by the SP-CP and O-CP methods developed in the previous chapter are combined with MRI segmentation and dipole source localization. This combination allows to localize the seizures more precisely and visualize the results on the patient specific MRI. The goal of these methods is to be able to search for a link between the location of the brain damage as seen on MRI and the estimated location of the seizures as measured with EEG. This chapter was realised in collaboration with the IPI (MRI segmentation and building of realistic head model) and TELIN (dipole source localization in realistic head model) research groups of the UGent.

7.1 Introduction

It is not known yet if there is a relationship between the location of the neonatal seizures and the location of the structural brain damage as seen on imaging techniques such as MRI and ultrasonogram [11]. It might be that the location of the brain damage is not directly related to the location of the seizures. But it is not unlikely that damage in one brain region leads to seizures in another in a predictable manner. If such a relationship could be found, it would be of great help for early diagnosis, prognostication and guide treatment of neonates with brain damage in the NICU. For such research purposes, the SP-CP and O-CP algorithms developed in the previous chapter can be combined with dipole source localization [68, 131, 132] in a realistic head model [50]. There is controversy

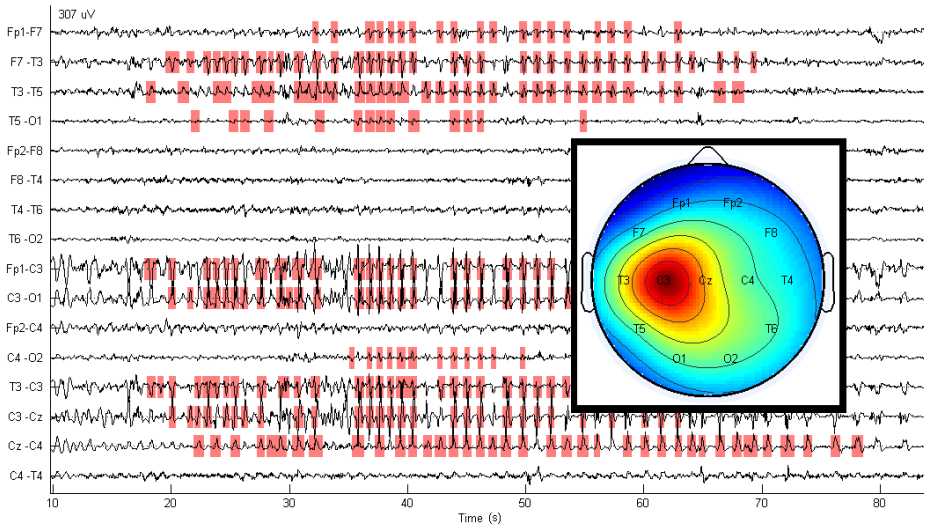

Figure 7.1: *Illustration of the extraction of the spatial distribution of a neonatal spike train type seizure using the SP-CP method. The spatial distribution indicates the spread of the seizure on the scalp.*

whether (neonatal) seizures can be modeled with a dipole and realistic conductivity values for the neonatal brain are not yet at hand with certainty. Even with these limitations, we feel that combination of these techniques is a useful tool in exploring the link between the location of structural brain damage and neonatal seizures.

7.2 Materials and methods

7.2.1 Spatial distribution of the seizures on the scalp

First, the neonatal seizure detector detects the seizures and marks the seizure activity in the EEG [46]. Depending on the nature of the seizure, either oscillatory or spike train, respectively the O-CP or SP-CP method is used to extract the spatial distribution of the seizure on the scalp. Fig. 7.1 shows an example of the spatial distribution of a spike train type seizure extracted with the SP-CP method.

7.2.2 MRI segmentation

In comparison to an adult head, segmentation of term neonatal MRI volumes is a more complex and challenging task. The difficulties are mainly caused by: an underdeveloped brain and skull, large intensity overlaps between different tissues, intensity inhomogeneity, low contrast to noise ratio, motion artifacts (ghosting effects) and low inter-slice resolution. To date, many MRI segmentation techniques have been reported for the adult and neonatal brain [223, 163, 208, 167]. In this application a five step segmentation process was developed [50]:

1. Head segmentation: removal of the background.
2. Brain extraction: generation of a brain mask.
3. Brain segmentation: into two clusters, CSF and tissue.
4. Fat and skull segmentation.
5. Scalp (skin) segmentation.

An example of a final segmentation result applied to the head of a 39 weeks old infant is shown in Fig. 7.2.

7.2.3 Dipole source localization

The EEG dipole localization problem is twofold [73, 75]. First, the forward problem states the relations between the potential values at the scalp electrodes and a given source. The electrode potentials are obtained by solving the Poisson equation given a dipole source in a specified geometry.

$$\nabla.(\sigma(x)V(x)) = I\delta(r - r_k) - I\delta(r - r_l) \tag{7.1}$$

where $\sigma(x)$ is the location dependent conductivity tensor and $V(x)$ is the potential distribution inside the head model due to a dipole with current source and sink at positions r_k and r_l. In a spherical head model, equation 7.1 can be solved using an analytical expression. The head model we used, was a realistic head model derived from an T1 MRI. In this study we used a finite difference method that can incorporate anisotropic conductivities [74]. The head model was segmented in 4 compartments: scalp tissue, skull, cerebrospinal fluid (CSF) and brain tissue. The conductivities of the compartments were isotropic and were equal to 0.43 S/m, 0.020 S/m, 1.43 S/m and 0.17 S/m for scalp tissue, skull, CSF and brain tissue respectively [65]. The 13 electrode positions were set in a standard 10-20 system and were hence not adjusted to the patient specific positions.

Second, the inverse problem searches parameters of the dipole given the scalp potentials. Estimating the electrical source in the brain based on the spatial

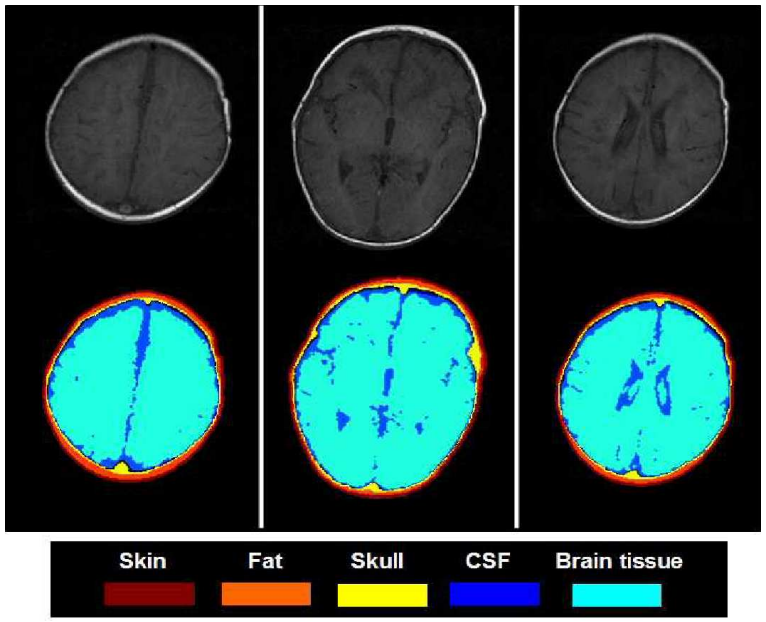

Figure 7.2: *Segmentation result of the head of a 39 weeks old infant. Upper row shows original T1 MRI images and the lower row presents the segmented images. At the bottom an explanation of the labels is given. From [50].*

distribution of the potentials on the scalp is not an easy problem. The problem is greatly underdetermined as there are an infinite number of electrical sources in the brain that can generate the same potential distribution on the scalp. In literature, several approaches, based on different assumptions can be found [7, 132]. One assumption is that the surface potentials are generated by a dense set of dipolar sources distributed on the cortical surface. The most popular method from this "distributed source" family is Loreta [156]. In a second approach, which is the most common, a limited number of "equivalent dipoles" are assumed to generate the measured potential distribution [183]. Dipole modeling is a well-established technique for localising interictal spikes, see e.g. [131, 105] and references herein.

Solving the inverse problem consists of finding the parameters of the dipole source that best explain the set of measured potentials consisting of the preprocessed EEG spike trains. We find the optimal dipole position r and direction d for the input potentials V_{in} at k scalp electrodes. This is done by minimizing the relative residual energy (RRE):

$$RRE = \frac{\|V_{in} - V_{model}(r,d)\|_2}{\|V_{in}\|_2} \tag{7.2}$$

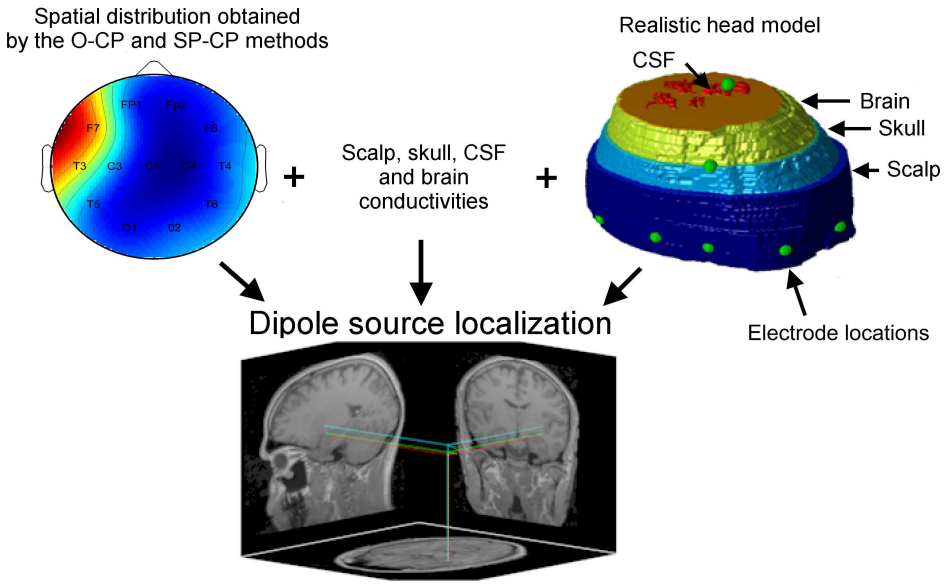

Figure 7.3: *Schematic overview of the requirements for dipole source localization in a realistic head model.*

where V_{in} are the preprocessed spike trains and V_{model} are the electrode potentials obtained by solving the forward problem with a dipole source position r and direction d. $\|.\|_2$ indicates the L_2-norm. The solution of the inverse solver is restricted to the brain compartment. The Nelder-Mead simplex method is used to find the minimum of the RRE.

7.2.4 Combination of methods

The separate algorithmic developments in EEG analysis, MRI segmentation and dipole source localization can be combined in one analysis together with the knowledge of brain conductivities. Fig. 7.3 gives an overview of that combination. The dipole is visualized on the T1 MRI image for interpretation.

7.3 Results

The methods were tested on 6 full-term neonates with brain damage showing electrographic seizures due to asphyxia. T1 MRI images were acquired on a Siemens 1,5T MRI scanner ($256 \times 256 \times 20$ voxel matrix with a resolution of

$0.7mm \times 0.7mm \times 4mm$). Representative seizures from each patient were selected and localized using a patient specific realistic head model. Fig. 7.4 shows some qualitative results of the source localization method.

7.4 Discussion

The aim of this study is to show the feasibility to perform EEG source localization on the newborn brain, based on a realistic head model. We are aware that a continued phase of quantitative validation is needed by testing the algorithm on more patients with extensive validation. However, at the time being the latter was not to our disposal yet. RRE values for all patients range from very low (<0.1) to moderatly high (>0.2).

The dipole positions we obtained are where we expect them to be. For instance, the topographic plot of seizure 1 of patient 1 has a clear focus of the positive amplitude activity on channel O1 (the other negative polarity is absent as it is directed away from the electrodes). This is only possible if the seizure activity is cortical, otherwise the focus would be more diffuse. The estimated dipole by the combined methods is indeed cortical. The topographic plot of seizure 2 of patient 1 on the other hand shows a more diffuse picture for both polarities. This is only possible if the seizure generator is further away from the electrodes and in this case from deep inside the brain. The estimated dipole clearly indicates a deep brain source.

It is important to note that the quality of the MRI data was rather low as it was not recorded with this application in mind. For several datasets part of the top of the skull was missing and had to be reconstructed. The exact location of the EEG electrodes was also not known and was estimated based on the 10-20 standardized system. To minimize errors and lead to better results all these issues need to be addressed first. Although these results are qualitative in nature, the preliminary results are plausible and proof the technology is ready and they show great potential to gain insight in the connection between brain damage and seizures.

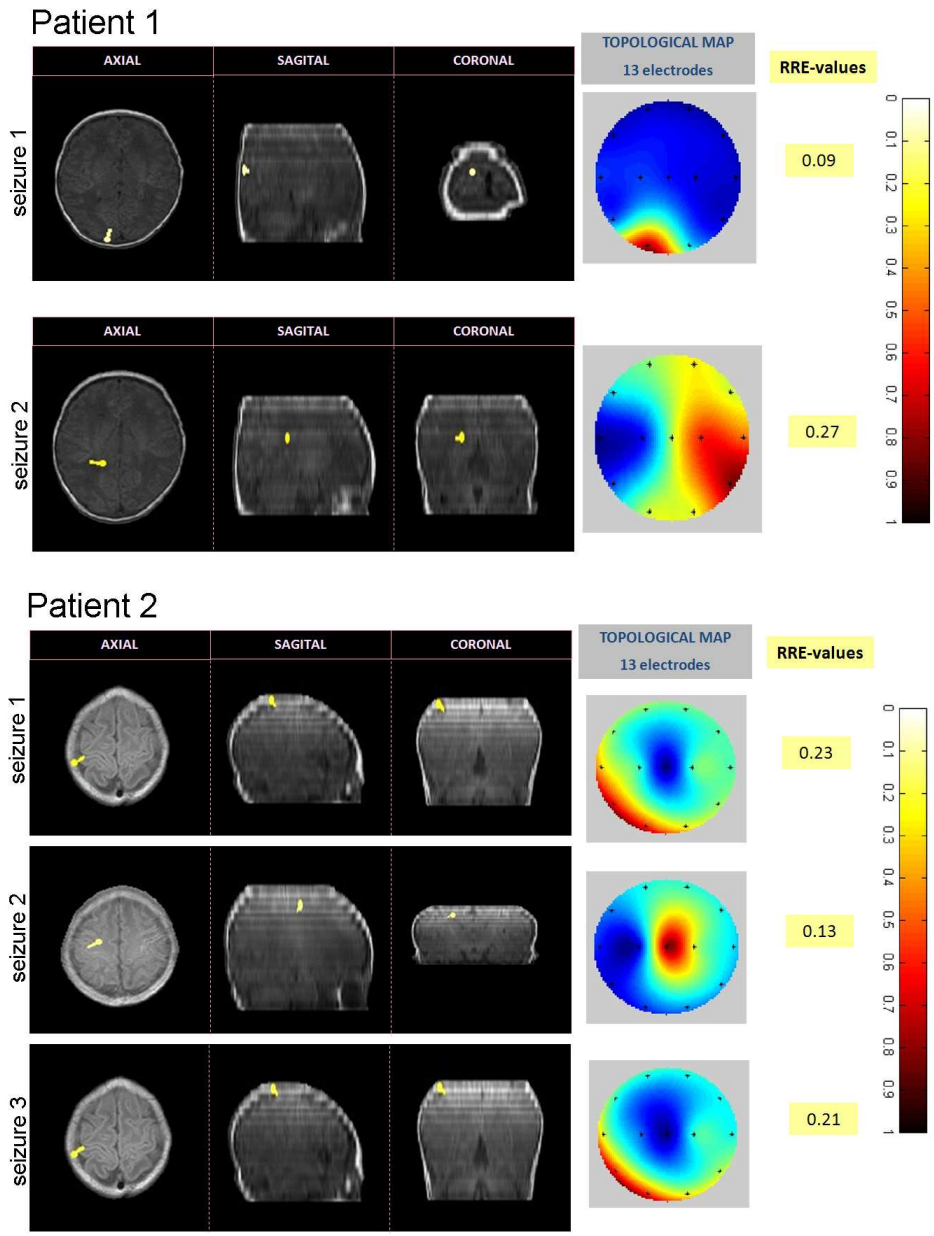

Figure 7.4: *Results of the seizure localization in a realistic head model of 2 patients. Seizure 1 of patient 1 is a cortical left occipital seizure while seizure 2 is localized deep in the brain. All three seizures of patient 2 are left central.*

Chapter 8

CPA applied to EEG transients and time varying EEG activity

This chapter describes a few other applications of CPA analysis and extends the use of the SP-CP and O-CP methods described in chapter 6. In the first section, the SP-CP method is applied to a range of EEG transients. We start with the application of the method to an adult patient with a thalamic bleed. Then, the method is applied to EEG spikes of children with a complex occipito-frontal spike pattern. In the second section, the O-CP method is extended to be used on time varying EEG activity. Therefore, the EEG is divided into short overlapping segments and on each segment an O-CP analysis is performed. The results of all the O-CP analysis are grouped and integrated using an SVD postprocessing step.

8.1 SP-CP transient analysis

8.1.1 Application to a patient with a thalamic bleed

The adult patient in this application has a severe thalamic bleed as can be seen on the MRI in Fig. 8.1A. The brain damage leads to abnormal transients in the EEG. Fig. 8.1B shows the average of 7 transients. These transients are related to the brain damage. We want to know the spatial spread of these transients, but as they are individually corrupted by other ongoing EEG we need to use all of them in one analysis. Therefore, the 7 transients are aligned into a tensor with dimensions time, electrode and transient. The SP-CP method is applied to that tensor as described in chapter 6.

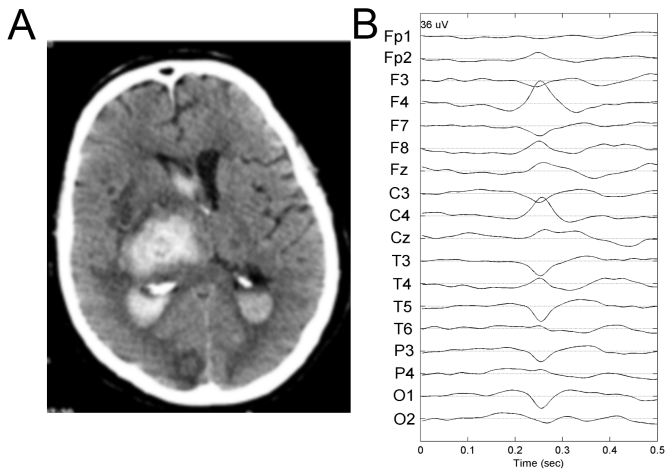

Figure 8.1: *A: MRI of the patient with a thalamic bleed. B: Average of 7 EEG transients related to the condition of the patient.*

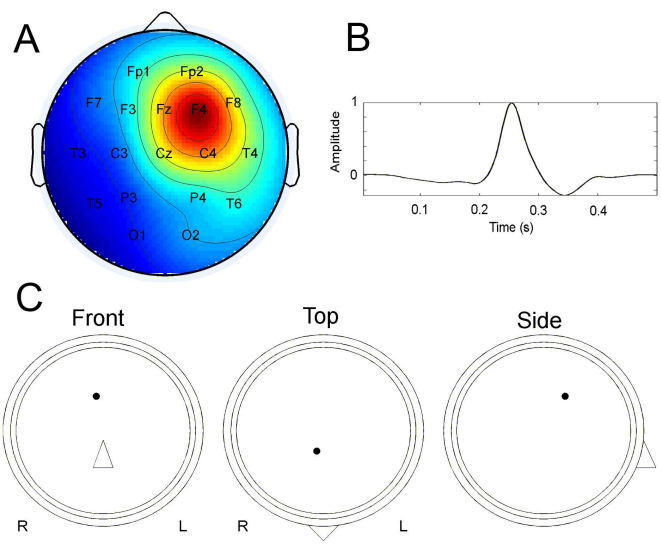

Figure 8.2: *Results of the SP-CP analysis of the transients in the EEG of a patient with a thalamic bleed. A: Topographic plot of the spatial distribution on the scalp. B: Extracted time domain activity of the transients. C: Dipole source localization in a three layer spherical head model of the spatial distribution. The dipole indicates a deep brain source.*

The results of the SP-CP analysis of the tensor are shown in Fig. 8.2. Fig. 8.2A shows a topographic plot of the extracted spatial distribution and Fig. 8.2B shows the extracted time information. Fig. 8.2 shows the dipole source localization in a spherical head model of the extracted spatial distribution. These results indicate that the transients observed in the EEG are generated deep inside the brain. There is a likely relationship between the generator of the transients and the bleeding. Although we can not be sure about the results, they do indicate that the SP-CP method is a good tool for transient analysis.

8.1.2 Application to complex occipito-frontal spikes

The children in this application have a rather abnormal spike distribution pattern on the scalp. We won't go into greater detail about the medical background of this condition. We will only investigate what the SP-CP method is able to do with this complex spike pattern. First there is an occipital spike which is within 8-30 ms followed by a prefrontal spike (Fig. 8.3). The prefrontal spike is not seen without the occipital spike. We want to separate the two spikes from each other. Fig. 8.4 shows the results of the SP-CP technique applied to the occipito-frontal spikes of 4 patients. For each patient, a set of spikes are aligned in the tensor. The tensor is then modelled using a 2-component CPA model. In this application, we use 2 components as we want to separate the 2 types of spikes from each other. The extracted time signals shown in Fig. 8.4 illustrate the time delay between the spikes. The topographic plots illustrate the spatial difference between the extracted spikes. The first spikes starts occipital and the second is frontal.

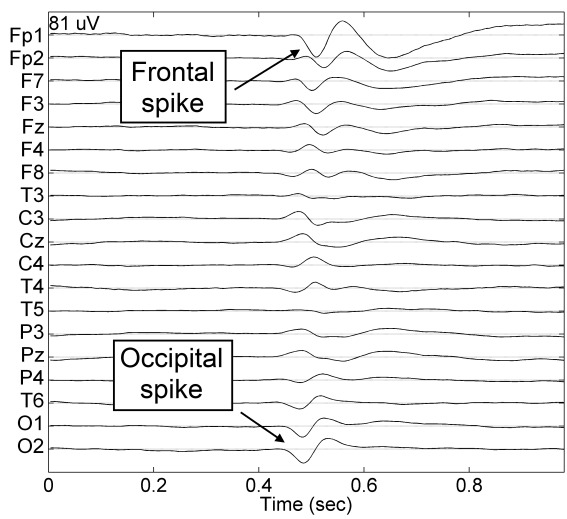

Figure 8.3: *Illustration of the average of 30 occipito-frontal spikes of a single patient. First there is an occipital spike followed by a frontal spike.*

8.1.3 Discussion

In this section, the SP-CP method that was developed in the previous chapter is applied to other transients in the EEG. The results illustrate the wide applicability of the SP-CP method for transient analysis in EEG. A set of transients can be modelled with 1 CPA component or more depending on the number of underlying sources generating the transients. Another potential application is the modelling of inter-ictal epileptiform spikes in the EEG of epilepsy patients. These inter-ictal spikes originate from the same region generating the epileptic seizures and are extremely valuable in diagnosis and analysis of epilepsy. Current practice is to average a number of these inter-ictal spikes to improve the SNR and then localize them. SP-CP may provide significant advantages such as better signal to noise ratio (as proven in chapter 6).

8.2 O-CP analysis for EEG dynamics

8.2.1 Introduction

The most important drawback of O-CP analysis described in chapter 6 is that it must be applied to a single EEG window. As only one localization vector can be given for each type of activity, this leads to the assumption of a stationary localization for the complete window of analysis for that type of activity. The method is thus not optimized to extract seizure activity in a situation where the seizure activity is shorter in duration than the complete window under analysis. Furthermore, we would like a method that is also able to give time information about exactly when the extracted activity is present in the window under analysis and is able to give an intuitive order of the importance of each extracted activity in the EEG.

8.2.2 Method

To cope with several types of activity that are active during only a limited amount of time in the window of analysis, we divide the EEG into several short, overlapping windows. We chose to take windows of 2 s with an overlap of 0.5 s between consecutive windows as this is a good compromise between time resolution and having enough data points for a reliable signal separation. A tensor is constructed of each window with a continuous wavelet as described in chapter 6. Subsequently, the tensor is decomposed using a 2-atom CPA. By checking the Core Consistency Diagnostic [10], we found the optimal number of atoms to be two.

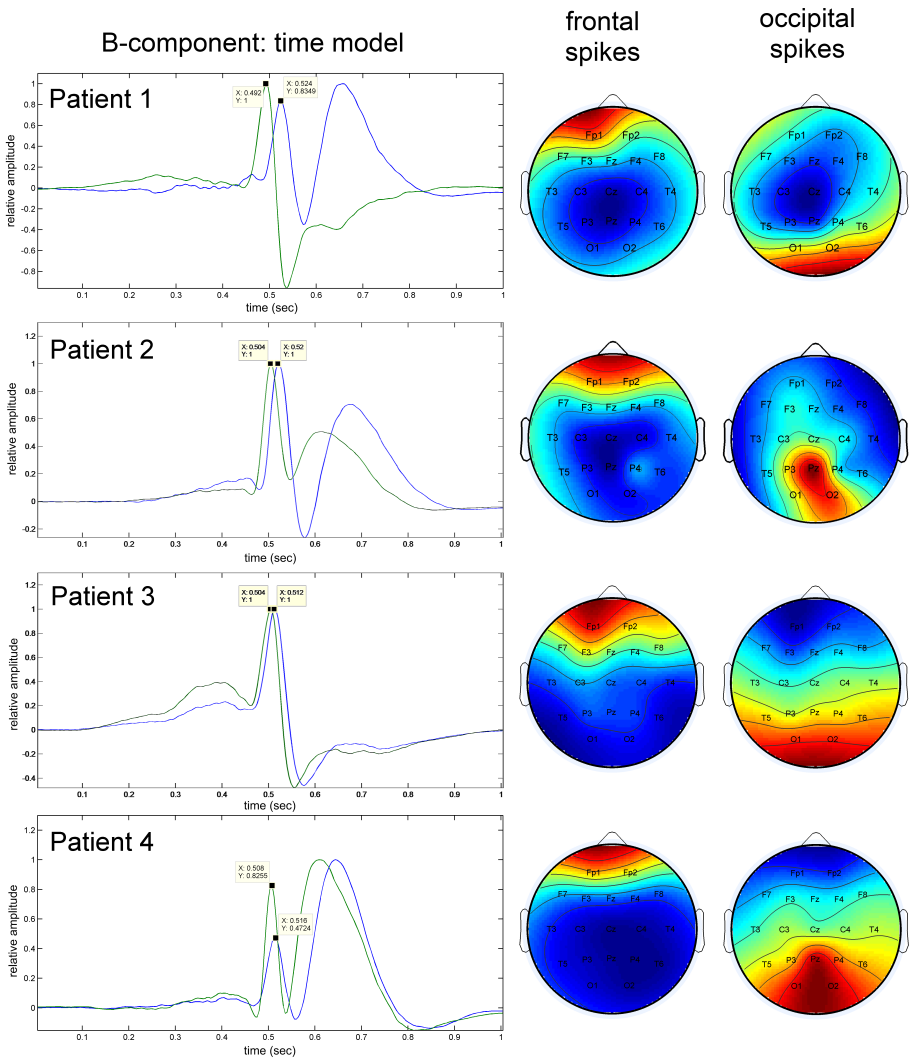

Figure 8.4: *Results of the SP-CP analysis of 4 patients with occipito-frontal spikes. The time signals illustrate the SP-CP method is able to separate both spikes. The topographic plots show that the first spike is occipital (green time signal) while the second is frontal (blue time signal). These results indicate the good separation both in the time and spatial domain.*

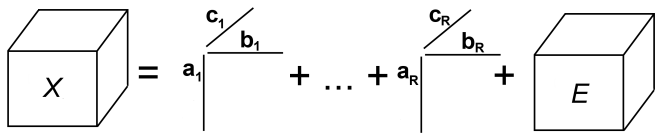

Figure 8.5: *Pictorial representation of CPA with R atoms.*

This decomposition leads to two extracted time vectors (components $\mathbf{b}_1$ and $\mathbf{b}_2$, see Fig. 8.5), two localization vectors ($\mathbf{a}_1$ and $\mathbf{a}_2$) containing the spatial distribution of the extracted time series and two frequency distribution vectors ($\mathbf{c}_1$ and $\mathbf{c}_2$). For the purpose of localizing the seizures, we are particularly interested in the two localization vectors per window. Both localization vectors of each window are collected in the rows of one matrix which we refer to as the **A**-matrix (Fig. 8.6). SVD decomposes a matrix into orthogonal components and orders them in order to their contribution. SVD applied to the **A**-matrix allows us to extract the dominant sources. The right eigenvector (matrix **V** in Fig. 8.6) corresponding to the singular value with the highest relative power (s_1) is the spatial distribution of the dominant source in the complete EEG. The left eigenvectors (matrix **U** in Fig. 8.6) contain the time occurrence of the activity in the window under analysis. The relative power of the singular value can be calculated using:

$$S_i = \frac{s_i^2}{\sum_{j=1}^{N} s_j^2} \tag{8.1}$$

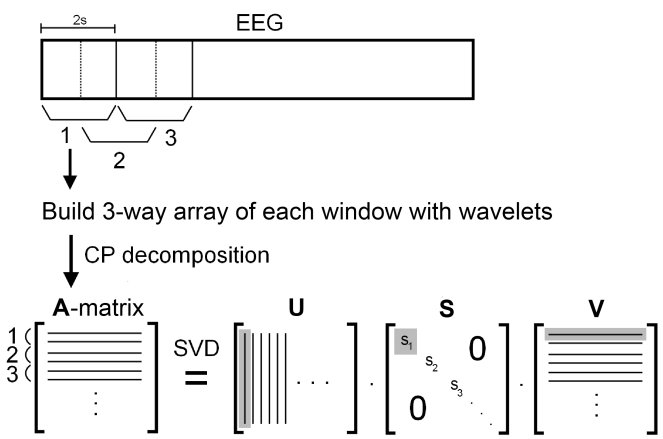

Figure 8.6: *Schematic overview of the CP-SVD method. The **A**-matrix consists of 2 localization vectors for each EEG-window. An SVD analysis is performed on this **A**-matrix. The spatial distribution vector in matrix **V** corresponding to the largest singular value s_1 is the spatial distribution of the dominant source in the complete EEG.*

8.2.3 Results

Simulation

We define the performance of the method on the simulated EEG signal shown in Fig. 8.7. The simulated signal consists of 2 sine waves corrupted by noise. The first sine wave of 2Hz is set at the 2 frontal Fp channels; the second of 4 Hz is set at channels F8 and T3. Both are active during half of the entire window and are non-overlapping.

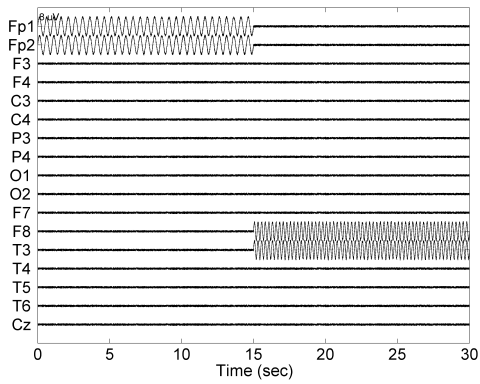

Figure 8.7: *Simulated EEG signal with oscillations on the frontal channels and on channels F8, T3.*

Fig. 8.8 shows a visualization of the **A**-Matrix that contains all the **a**-components of the subsequent CP-decompositions applied on overlapping 2 s windows. This figure shows that the first half of all the windows contain strong activity on the frontal Fp channels and the second half of the analysis contains strong activity on channels F8 and T3.

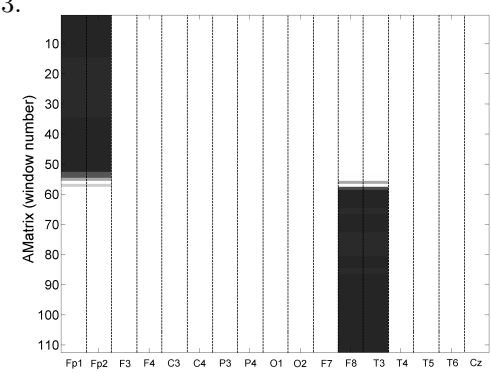

Figure 8.8: *Visualization of the **A**-Matrix containing all spatial distribution vectors extracted by the subsequent O-CP decompositions on the simulated signal.*

The subsequent SVD analysis calculated on the **A**-Matrix shown in Fig. 8.9 reveals that there are 2 dominant components present in the simulated signal with a relative strength, calculated using the power of the singular values, of 50.5% and 49.5%. The topographic plots are the spatial distributions corresponding to the first two right eigenvectors in Fig. 8.6 (Matrix **V**). Correlation of these **u**-vectors with the original simulated mixing of the sources is equal to 1, meaning exact reconstruction and no influence of the noise. The curves below the topographic plots show the distribution of the activity over the extracted spatial distributions in the **A**-matrix (**U**-matrix of the SVD analysis) and give an indication of the time occurrence of the detected activity. The frontal activity is clearly active during the first half of the window and the other activity during the second half.

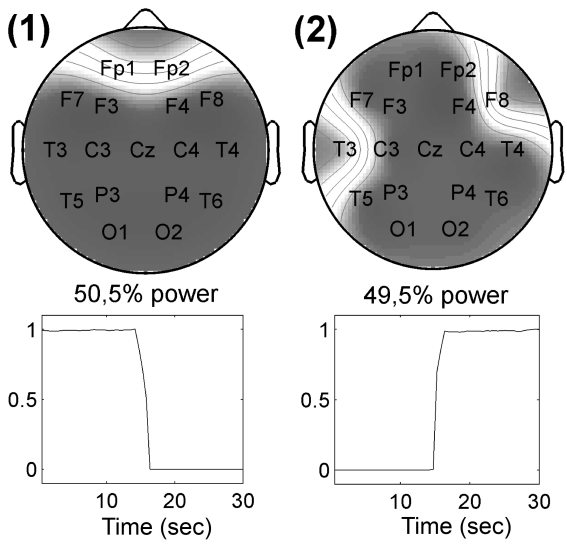

Figure 8.9: *Results of the CP-SVD method applied on the simulated EEG shown in Fig. 8.7. (1): The first eigenvector with a power of 50.5%, frontal distribution and the time profile indicates it is only present during the first half of the signal. (2): The second eigenvector with a power of 49.5%, spatial distribution on T3 and F8 and the time profile indicates it is only present during the second half of the signal.*

Illustration

We will illustrate the application of the algorithm on the neonatal EEG displayed in Fig. 8.10. There are three important types of activity present in this EEG. There is an oscillatory seizure present on the occipital channel O1. There are horizontal eye movements on the frontal channels Fp1 and Fp2, starting from second 22. And finally, there is a burst (between seconds 10 to 15), predominantly present right temporally.

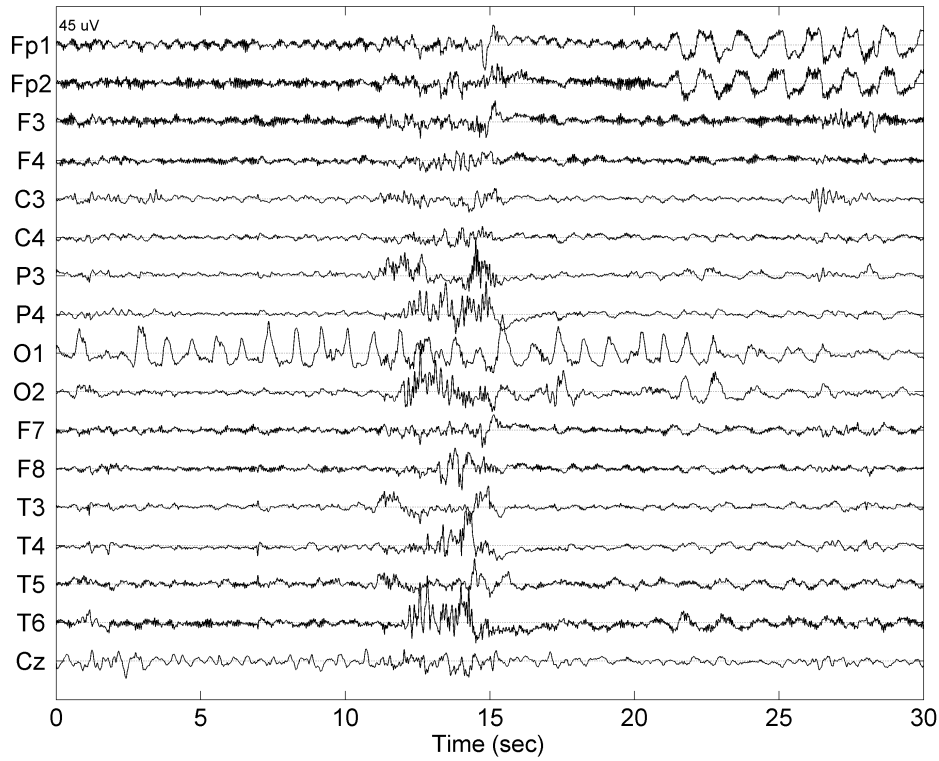

Figure 8.10: *Example of an oscillatory seizure predominantly present on channel O1. On the frontal channels Fp1 and Fp2 another oscillation is present due to horizontal eye movements. Between 10 and 15 s a burst of activity is present predominantly right temporally.*

Fig. 8.11 shows the visualization of the **A**-Matrix that contains all the **a**-components of the subsequent CP-decompositions applied on the EEG of Fig. 8.10. The three dominant types of activity can clearly be identified on this plot. The first **a**-components contain activity on channel O1. Between **a**-components 40 to 60 the more dispersed burst activity can be seen and at the end, the eye movements on the frontal channels are dominant. The results shown in Fig. 8.11 of the subsequent SVD analysis on this **A**-Matrix reveal the dominant sources. Only the first 4 dominant sources are shown. The topographic plots of the first 4 right eigenvectors (matrix **V**) show occipital, frontal and right temporal activity.

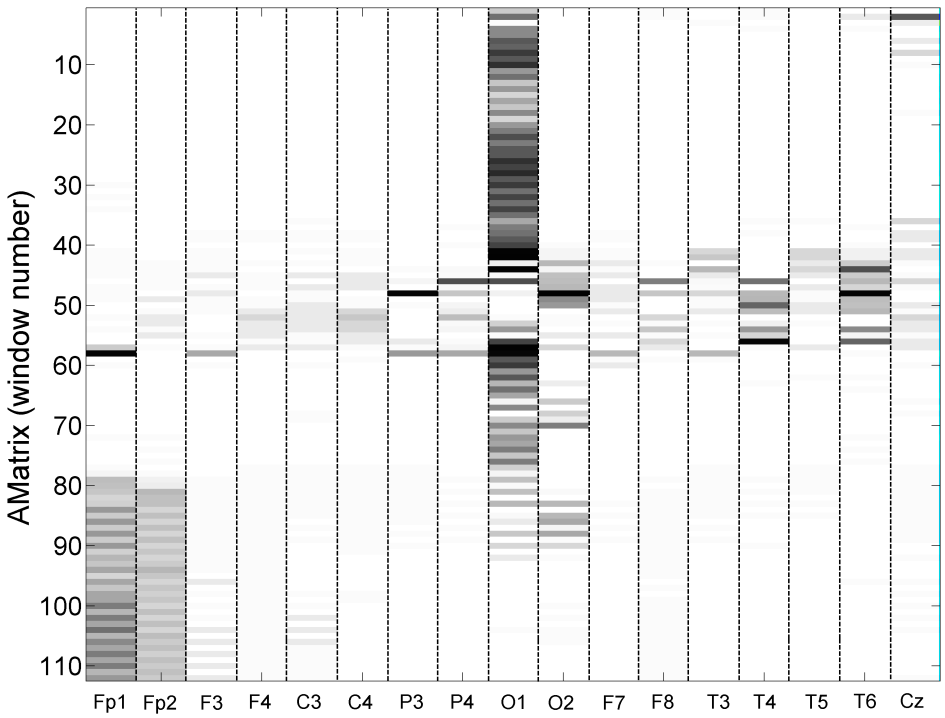

Figure 8.11: *Visualization of the* $\boldsymbol{A}$*-Matrix containing all spatial distribution vectors extracted by the subsequent O-CP decompositions on the real EEG.*

The seizure activity and eye movements are nicely separated from each other, the burst activity is split up between two sources. The seizure activity is the strongest source in the EEG with a relative power of the singular value of 54%, followed by the eye movements with a power of 30%. The plots of the left eigenvectors ($\mathbf{U}$-matrix) reveal the time occurrence of each activity. The seizure activity at O1 is strongest in the beginning, fading at the end and with a dip in the middle due to the burst. The frontal activity is strongest at the end. The two burst sources are clearly strongest in the middle of the window under analysis.

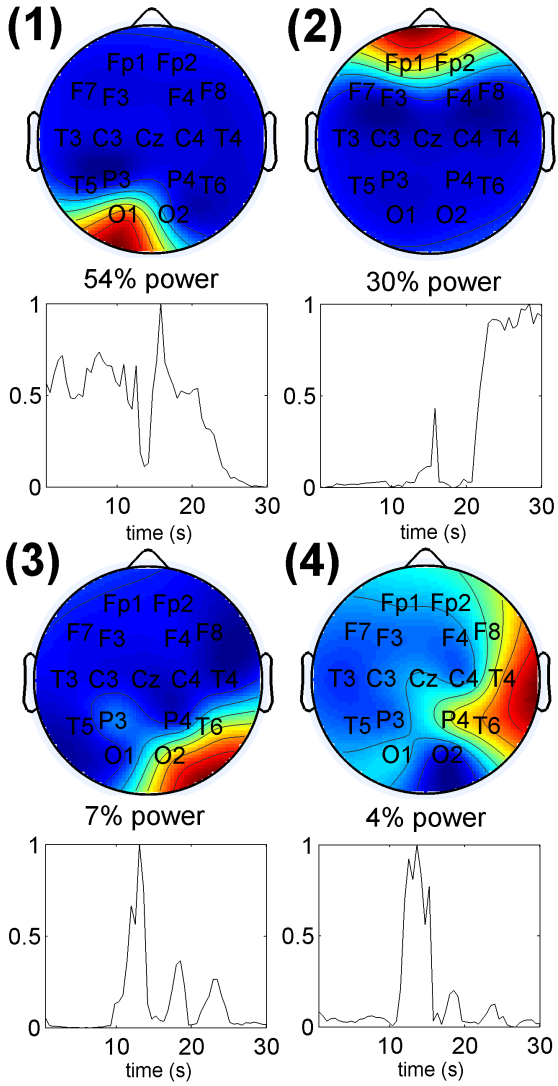

Figure 8.12: *Results of the CP-SVD analysis of the EEG shown in Fig. 8.10. The four first left eigenvectors of the SVD analysis are shown here. The topographic plots correspond to the first four right eigenvectors of matrix* $\boldsymbol{V}$ *in Fig. 8.6. The value under each topographic plot is the relative power of the singular value and the curves at the bottom, display the distribution over the extracted spatial distributions in the* $\boldsymbol{A}$*-matrix (matrix* $\boldsymbol{U}$ *in Fig. 8.6).*

8.2.4 Discussion

This is a new approach to extract the spatial distribution of the dominant sources in an EEG window that can also provide time information about when the sources are active and give a natural order of the strength of the sources in the EEG. The method splits the EEG up in 2 s windows and builds a third-order tensor in which the first two dimensions are space and time and the third dimension is constructed by decomposing the EEG into different frequency components. The subsequent CP-decomposition of each tensor provides us with reliable spatial distributions which can be grouped in a matrix called the **A**-matrix. Visualization of this matrix (Fig. 8.9 and 8.12) shows the value, as the time/localization information of the matrix is easily interpretable. SVD analysis of this **A**-matrix allows us to calculate the strength of each source using the power of the singular values. The left eigenvectors give us the time information when the source is active during the window and the right eigenvectors give us the topographic information of the extracted activity. Combination of this information gives us a clear overview of what is going on in the EEG and allows easy interpretation.

There is however a very strong limitation and drawback to the use of SVD in the postprocessing step of the O-CP localizations. The use of SVD assumes that the spatial distributions of the dominant sources are orthogonal to each other. This is a strong assumption that is not always valid. In practice the method is only applicable to sources that have a clear spatial separation from each other (e.g. eye movements and seizure activity). It is not possible to use BSS techniques like ICA here as the size of the spatial distributions (typically 17 samples) is too small for reliable estimation of independent sources. Nevertheless the drawbacks, the concept of a set of subsequent O-CP analysis on short windows and subsequent postprocessing and integration of the O-CP results is valuable.

Chapter 9

On and Off-line software development and concepts for commercialisation

This chapter describes the software in which the developed algorithms are implemented. The Graphical User Interface (GUI) allows the neurophysiologist to visualize the data, start the analysis and interpret the results offline. As the software has to be used by neurophysiologists it needs to be user friendly and straightforward to use. A real-time proof of concept software implementation of the seizure detection was created and tested at the bedside. Although the software is functional, it is far from being commercially usable. In the final part of this chapter we discuss several concepts of products that may be suitable for commercialization.

9.1 Graphical User Interface

EEG recordings can become very long (24-72 h). With such large amounts of data it is important that the data can be quickly visualized and navigated. Therefore, a Graphical User Interface (GUI) is essential. Fig. 9.1 displays the GUI as it is developed in its current form. Neurophysiologists use it already for quite some time and find it easy to use. The GUI consists of the followings elements:

1. EEG plot window
2. Data position bar

3. ECG plot window
4. Abdomen sensor plot window
5. Tremor sensor plot window
6. EOG plot window
7. Filter settings
8. EEG navigation settings
9. EEG sensitivity
10. Artifact removal settings
11. EEG navigation controls
12. Montage switch

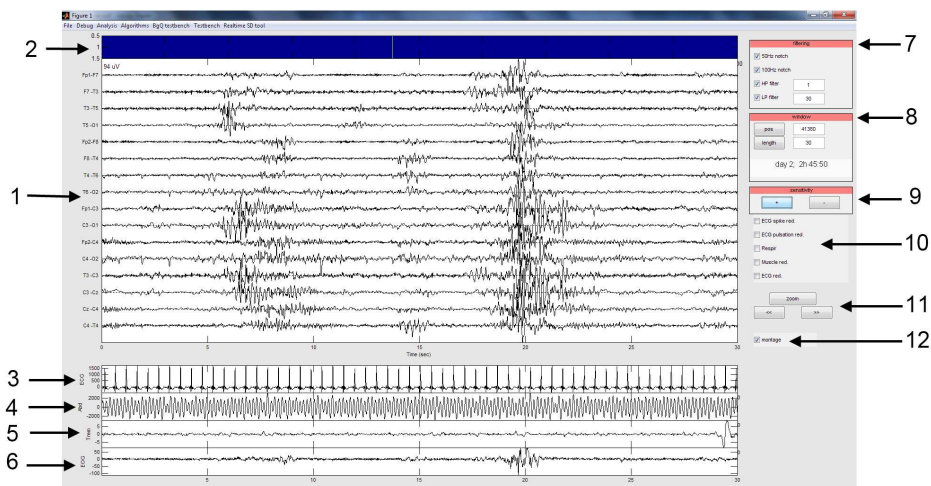

Figure 9.1: *Illustration of the developed graphical user interface in which the EEG can be viewed and analysed.*

The *data position bar* is a helpful tool to quickly navigate through a large amount of data. The bar represents the complete EEG measurement and can be clicked for easy data navigation. For example, if the complete measurement is 24 h long and the user clicks in the middle of the bar, then the data visualized in *EEG plot window* is the data measured at 12 h since the beginning of the measurement.
Numbers 3-6 represent the plot windows in which the polysomnography data is visualized. At this moment 4 types of polysomnography are supported (ECG,

respiration, tremor and EOG).
The *filter settings* allow to turn the filters on/off. The low/high-pass filters can be set to the desired frequency.
The *EEG navigation settings* give control over what data is visualized in the *EEG plot window*. The position is calculated in seconds since the beginning of the measurement. The length control box defines the length of the data visualized. The recording day and hour of the measurement position is given below these controls.
The *EEG sensitivity* allows to control the amplitude of the EEG. The current EEG amplitude is marked in the left-upper corner of the *EEG plot window*.
The *artifact removal settings* allow to turn on/off the artifact removal.
The *EEG navigation controls* allow more precise control over the EEG window that is visualized. The arrows shift the window left/right. The zoom button allows to zoom in on a specific part of the EEG.
The *Montage switch* allows to switch between a predefined bipolar montage and average reference.

9.2 Proof of concept at the bedside

During development of the seizure detector, special care was taken to make use of methods with low computational complexity. The algorithm has to able to run at real-time on a 20 channel bipolar EEG montage. The seizure detection is run on 30 s long windows which are shifted through time with a 5 s time step. Therefore, the algorithm needs to process each 30 s window in less than 5 s. Artifact removal using BSS adds additional computation time. To limit the computational load, the maximum number of iterations of the BSS methods are limited to ensure a short calculation time for each window. The sofware was implemented in matlab. To be able to test at the bedside, additional commercial software, namely 'brainRT' by 'OSG' was needed. This commercial software writes the recorded data to a file on a folder on the harddrive. The matlab implementation of our software monitors this file and every time 5 s of new data is added by the OSG software, our software reads the added data and runs the algorithms. When our software finishes the computations in less than 5 s, the matlab software is ready to accept new data and monitoring can proceed in real-time. In case our software takes longer than 5 s to process the data, a delay may arise between the data that is recorded and processed. If the slower than real-time processing is brief, the system is designed in such way that it can catch up with the recording on the next iterations. Therefore an occasional slower than real-time processing does not pose a problem. This situation can arise when there is a lot of repetitive activity in the EEG (e.g. during a seizure) and the correlation step of the spike train detection or autocorrelation step of the oscillation detection need to process a lot

of data. When a seizure is detected, an auditive alarm goes off. What is detected is visualized to the user and the start and duration of the seizure is stored in a list. The system was tested at the bedside. Seizures could be simulated by lightly tapping on the electrodes fixed to the scalp of the neonate. The system correctly detected the simulated seizures and gave an auditive alarm to the user. Although the system is functional and the proof of concept test was successful, we are still far away from a commercial grade system. First of all, we still need the OSG commercial software to connect to the EEG amplifier and store the data. This system is a full size EEG monitor and overkill for most NICU's. A usable EEG monitor at the bedside needs dedicated hardware, must be small and portable and easy to use. Secondly, the current matlab implementation is too complex to be usable by nurses or neonatologists at the bedside. Ideally, the software should be translated to a faster programming language (e.g. C++) with a dedicated user interface.

9.3 Concepts for commercialisation

9.3.1 Basic 2-channel system

The state of the art in current clinical practice is the CFM monitor. The success of this monitor can be attributed to its small size, ease of operation, and (perceived) easy interpretation. Although this system has many drawbacks as a seizure monitor it is an excellent tool for quantification of the background amplitude in the EEG. Therefore, future neonatal monitoring systems can stick to CFM as a background monitor tool but add additional more reliable automated seizure monitoring to it.
The seizure detection algorithm presented in this thesis is designed to run on single channel EEG. When more channels are available, the outputs of the analysis on each individual channel are just added to each other. Therefore the seizure detection can be run in the background on the raw measured one-channel EEG trace by the CFM monitor while the user only sees the processed CFM trace. When a seizure is detected, an auditive alarm can sound and the detected seizure can be visualized to the user by marking it on the CFM trace. Such a system would be as easy to use as the current CFM monitor but its possibilities for seizure monitoring would be much improved. As we have shown in chapter 4, our automated seizure detection is much more reliable than manual analysis of the CFM trace (albeit at a slightly lower sensitivity). An additional advantage is that the treating nurses can be warned at the moment the seizure is occurring as oppossed to visually checking the CFM trace once in a while.

9.3.2 Basic multi-channel system

The main drawback of the basic 2-channel system is the lack of spatial resolution. Yet, it is unrealistic to expect every NICU to use full 17 channel EEG monitors as used for adults. Fixing many electrodes on the head of the neonate seems to be difficult and time consuming. A compromise needs to be found between spatial resolution and the time needed to fix the electrodes. Therefore we propose a six channel EEG system with electrodes at C3-4, T3-4 and O1-2. Such a system would provide a good spatial coverage of the brain regions that are most sensitive for seizures. The frontal brain region (electrodes Fp1-2, F3-4, F7-8) is not measured because it is the one which is the least sensitive for neonatal seizures. Due to the proximity of the eyes, the frontal electrodes are susceptible for artifacts. Therefore, the frontal channels may be omitted. Parietal channels (P3-4) are also omitted even though this brain region is sensitive for seizures. This is not a real problem as seizures that are captured by P3-4 are in general also captured by C3-4, thus we are not loosing sensitivity. The display to the user can either be several CFM traces or the raw 6-channel EEG.

9.3.3 Advanced multi-channel system

This is the most complicated system and close to the EEG setup as used for adults. It can have up to 17 EEG channels and thus measure the whole brain. The advantage of the large amount of channels is the good spatial resolution and maximum sensitivity for seizure detection. The spatial resolution makes it feasible to use the seizure localization methods developed in this thesis. After a seizure is detected, the spatial distribution on the scalp can be visualized to the user using topographic plots. If polysomnography channels (ECG and respiration) are added, it is possible to do BSS to remove ECG spike, blood vessel pulsation and respiration artifacts and thus lower the number of false positive detections. Such a complicated system is probably too complex for the average NICU. Nevertheless, research oriented NICU's may have the need for such a system. A multi-channel system covering the whole of the brain may be cumbersome to use now due to the large amount of channels that need to be attached to the scalp. But this may change in the future due to development of electrode caps. These caps allow to fix a lot of electrodes at once instead of attaching them one by one. Obviously, this reduces the amount of preparation time to do an EEG and makes full-EEG feasible in any NICU. More advanced techniques exploiting the spatial resolution (like seizure localization) may then become the standard. Another promising development are wireless EEG electrodes which may greatly reduce the amount of wires.

9.4 Conclusion

In this chapter we discussed the software for offline and online processing of EEG signals. The offline processing allows to browse through the data and test the developed algorithms. It provides basic EEG processing functionality to the user such as filter settings, sensitivity and artifact removal. An implementation for online processing was developed. This software works in addition to commercial software by the company OSG. This software was succesfully tested for functionality at the bedside but is still far from usable in a clinical situation. We proposed 3 types of neonatal seizure monitoring systems with increasing complexity. The most simple device is an extended CFM monitor with automated seizure detection. Such a device would already provide a significant improvement for seizure monitoring in the NICU and is not more complex to use than the current CFM monitors. The second and third device use more EEG channels and are thus more complex to use. The benefit is that these devices offer more spatial resolution and thus increased sensitivity for seizures. We believe that the 6 channel device is still practically usable in the NICU. The full 17 channel device is probably only usable by more research oriented centers.

Chapter 10

Conclusions and open problems

In this final chapter, findings and conclusions of the presented work are summarised. In this thesis we covered three important topics which are valuable for implementation in a bedside neonatal seizure monitor. We did so using a broad range of signal processing techniques. For each topic we summarize the most important findings. Finally, some directions for further research are pointed out. Besides seizures, the background EEG and polysomnography are also of great importance and should be the subject of future development. We give an overview of the most important and promising techniques in literature together with some of our own preliminary results on the dataset used in this thesis.

10.1 General conclusions of the thesis

10.1.1 Neonatal seizure detection

- We identified the most important characteristics of the neonatal seizures the human observer seems to employ and we translated those into an algorithm using time domain signal processing. This is a logical strategy as it is essentially the human observer we are trying to replace. These characteristics are first of all the sudden change relative to the background EEG and secondly the repetition in time.
- We identified two major types of seizures, namely the spike train and oscillatory type. For each type a separate detection strategy was developed. Althought both are independent, they are matched to each other and both make use of the same human observer characteristics [46].

- Spike train type seizures display a discontinuous type of repetition, with generally a high frequency content. Oscillatory seizures display a continuous repetition with lower frequency content compared to the spike train type. This difference led to the separate implementations of the detection strategy.
- We proved it is possible to detect neonatal seizures with high sensitivity and low false positive rate.
- A real time implementation of the seizure detection algorithm was implemented and successfully tested at the bedside.

10.1.2 Artifact removal

- Many artifacts hinder the automated seizure detection as some of them have very similar morphology to seizures. To be able to identify the artifacts, polysomnography recordings are required.
- We identified the most important neonatal EEG artifacts leading to false positive detections by the seizure detection. These are ECG spike artifacts, blood vessel pulsation artifacts and respiration artifacts.
- BSS algorithms like ICA are able to extract the source of the artifact from the EEG.
- Additional processing is needed to be able to identify the source artifact based on the polysomnography recordings by enhancing the similar characteristics between them.
- Artifact removal can lower the amount of false positive detections of the developed seizure detector.
- Artifact removal allows to reliably perform seizure detection on recordings with persistant artifacts which would otherwise be unusable.

10.1.3 Neonatal seizure localization

- The spatial distribution on the scalp of a neonatal seizure can give information about the depth of the seizure (cortical or subcortical), number of seizure foci present, spread of seizures to contralateral hemisphere, etc.
- We developed two methods to separate the seizure activity from all other concurrent EEG activity based on the third order CPA method [47].
- It is important to build up the third order tensor in such a way that the activity we want to extract can be modelled with the trilinear structure of

the CPA method. For the spike train seizure type, this can be done by aligning the EEG of the detected spikes into separate slices of the tensor. For the oscillatory type, this can be done by decomposing the EEG into a set of frequency intervals using wavelets.

- The topographic plots provide the users easy understanding of the spatial information contained in the EEG which would otherwise need years of training.

10.1.4 Additional conclusions

- The extracted spatial distributions by the seizure localization methods can be used together with dipole source localization and a realistic head model to identify the brain region involved in generating the seizure [50]. Such a setup could be used in the future to study the possible link between seizure location and the location of the brain damage as seen on MRI.
- The SP-CP spike train localization method can be used universally as an analysis tool for transients in the EEG originating from the same brain region. Using more than one CPA components, the SP-CP method is even able to reliably separate transients with complex morphologies.
- The O-CP method can be applied to subsequent EEG windows to follow the time varying spatial information in the EEG [45]. With a subsequent SVD analysis, the most dominant brain regions can be identified and quantified. But we need to be aware that the SVD post-processing step does impose orthogonality of the spatial information, which makes it usable in only a limited number of cases such as when there is limited spacial overlap between the activities.
- The algorithms developed in this work can be combined together to form a complete seizure monitoring system outperforming the current systems in practice.

10.2 Future work and open problems

10.2.1 Burst-suppression monitoring

The burst suppression pattern on neonatal EEG is associated with poor outcome [129]. A neonate with a predominant interburst interval duration of more than 30 s has a 100 % probability of experiencing severe neurologic disabilities or death and an 86 % chance of developing subsequent epilepsy. Therefore, quantification

of burst and interburst intervals is valuable for the early estimation of neurologic prognosis. Burst-suppression analysis in the EEG should consist of 4 basic steps [3].

1. segmentation
2. feature extraction
3. classification
4. presentation

The idea is to break down the EEG into (pseudo)stationary segments and extract features that can be used to classify the segments (e.g. into burst, suppression, artifact, ...). To determine segment boundaries as exactly as possible, methods with fixed duration segments cannot be applied [178]. The final presentation step visualizes the data in a compressed form to allow a quick overview of the trend in a large dataset. Ideally, the system should compress BS information down to a quantity which can be evaluated at a glance, and should display them in a format intelligible to the neurologist [12]. Several representative measures can be extracted from BS-EEG, such as amplitude measures of the electrical activity between the bursts or the bursts themselves, frequency content of bursts, duration of the interburst interval and even a combination of any of these measures. For instance a compact representation of the BS pattern is the burst suppression ratio (BSR) [172].

$$BSR = \frac{total\ time\ of\ suppression}{epoch\ length} \tag{10.1}$$

In the literature several burst detection algorithms can be found. Lofhede et al. [117] extracts features from EEG windows and classifies those features in a subsequent step using an SVM classifier. Scherman et al. [184] made use of energy operators to detect bursts, the system itself was evaluated by Atit et al. [4], who compared the performance of the Teager Energy Operator to the Square Law Detector. Palmu et al. [153] also made use of an NLEO with good performance and compares the results to three neurophysiologists visually marking the bursts in the EEG. Future development should be committed to improve on these BS detection algorithms and most importantly bring them to the bedside in the NICU.

10.2.2 Entropy analysis

Entropy measures are gaining popularity in biological data analysis because of their ability to discriminate regular dynamics from irregular dynamics. Entropy

measures can quantify the complexity of measured observation signals without information about the underlying dynamics of the system [93]. In the literature, entropy measurements are used in many disciplines like sleep research [121, 16, 155], to study the effect of medication [122], recovery after cardiac arrest [188], hypoxic ischemic injury [204], ...

Entropy analysis of neonatal EEG may be interesting to study the effect of treatment with drugs, quantify long term changes in background activity (e.g. sleep wake cycling) in time and the effect of seizures on the background pattern (Fig. 10.1). It was suggested by Tong et al. [205] to define the entropy at each frequency instead of the entire frequency range using time frequency representation $tfr(\omega_i, n\Delta t)$. This makes sense as in neurological signal processing, we are often interested in different rhythms or specific spectral components [201]. Fig. 10.2 shows the entropy of a seizure and the background EEG before and after the seizure for frequencies ranging between 1 and 30 Hz. To obtain this result, the EEG was divided into overlapping windows of 5 s duration with an overlap of 1 s. Each window was split up into its frequency content (1-30Hz) using the continuous wavelet transform. For each frequency the Shannon entropy was calculated. Grouping all entropy values of each frequency and each time window together gives us a time-frequency plot of entropy values. From Fig. 10.2 it can be seen that the seizure has a large impact on the entropy. Mainly the higher frequencies (>5 Hz) show a large drop compared to the background EEG before and after the seizure.
These preliminary results show that entropy analysis of neonatal EEG may provide meaningful information for long term monitoring as well as for shorter events like seizures. Therefore, more research should be done to further develop these methods and validate them with clinical information.

10.2.3 Polysomnography analysis

Brain activity, respiration, heart activity and many other physiological measures cannot be seen as independent measurements. All of them are in one way or another coupled to each other and in many cases contain mutual information. For neonates, heart activity and respiration are the most important polysomnographic measurements and more research should be done to analyze them.

Regularity of respiration

Sleeping and waking reflect the underlying functioning of the brain [76, 202]. Sleep-wake patterns have been found to be related to developmental outcomes [14]. Respiration activity is strongly related to the sleep-wake cycles. In a

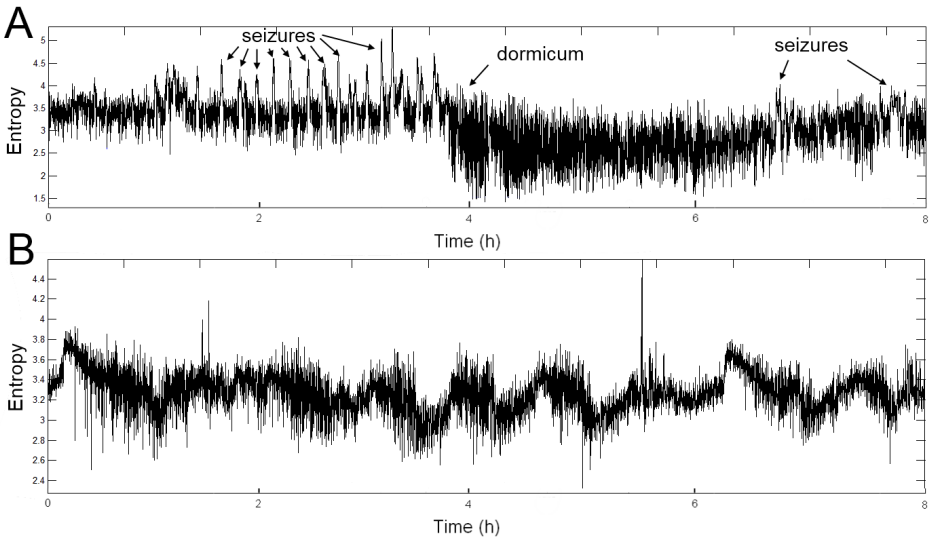

Figure 10.1: *A: Entropy analysis of a term asphyxiated neonate with seizures. In the first 4 h of the measurement there are a number of seizures present in the EEG (as indicated with arrows). After giving dormicum the seizures and EEG activity are suppressed, which can be seen by the lower entropy value. Towards the end of the measurement, entropy rises and seizures start to appear again. B: Entropy analysis of a normal term neonate. In the entropy analysis sleep-wake cycling can be observed.*

healthy neonate, the respiration is regular during quiet sleep. When awake and during active sleep, respiration is much more irregular [64]. Absence of sleep-wake cycles is one of the earliest abnormalities in an abnormal brain [218]. Conversely, the presence of sleep wake cycling is a good prognostic sign. To measure the regularity of the respiration, the signal is divided into windows of 30 s. Then the autocorrelation function of the signal is calculated. The regularity of the autocorrelation function is quantified by calculating the normalized area under the curve. The larger this area, the stronger the correlation in time as the autocorrelation function quickly drops to zero for uncorrelated signals but remains high for repeating signals. The result shown in Fig. 10.3D shows that for a healthy neonate sleep-wake cycling can be identified, while for asphyxiated neonates (Fig. 10.3A-C) these are not present, which is an indicator of brain damage.

ECG analysis

Vaughn et al. [214], Green et al. [70] and Cherian et al. [26]. studied the changes in ECG during seizure activity. Vaughn et al. found that the mean heart rate extracted from the ECG significantly decreases during seizure, while Green et al.

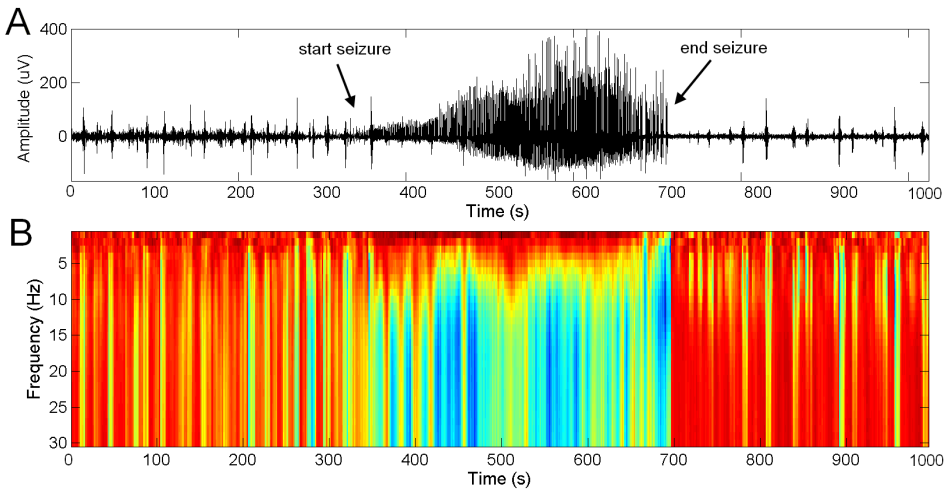

Figure 10.2: *A: 1000 seconds of burst suppression EEG, with a seizure starting at 350 s and ending at 700 s. B: Shannon entropy analysis of the EEG. The result shows a time-frequency (1-30 Hz) plot of entropy values (red is a high entropy, blue is low). During the seizure the entropy of the frequencies above 5 Hz drops sharply but restores when the seizure is over.*

reported a significant increase in heart rate and Cherian et al. found that heart rate changes are insensitive for detecting postasphyxial seizures. These results show that seizures might have an affect on the heart rate, but the conflicting results show that the precise nature is not yet known [123], therefore more studies are needed.

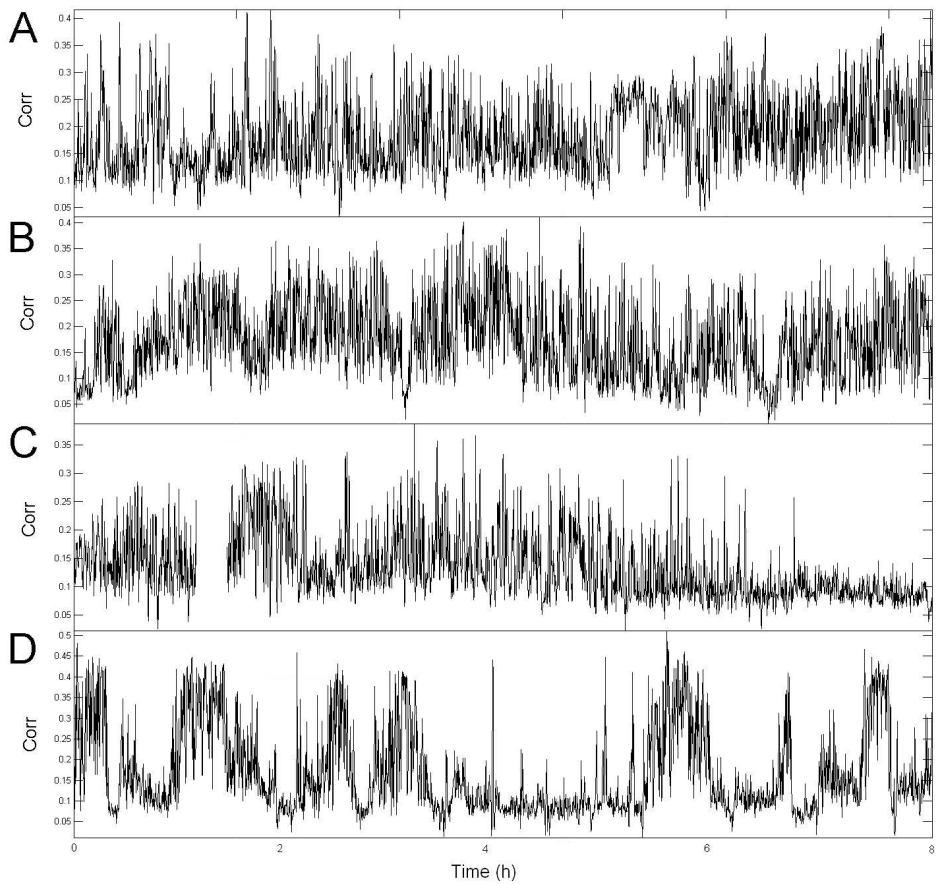

Figure 10.3: *A-C: Regularity analysis of the respiration of 4 asphyxiated term neonates with electrographic seizures. The respiration analysis is relatively flat with no apparent sleep-wake cycles. D: Regularity analysis of a healthy full-term newborn. The analysis shows clearly identifiable sleep-wake cycles.*

Bibliografie

[1] A. Aarabi, F. Wallois, and R. Grebe. Automated neonatal seizure detection: a multistage classification system through feature selection based on relevance and redundancy analysis. *Clin Neurophysiol*, 117:328–340, 2006.

[2] E. Acar, C. Aykut-Bingol, H. Bingol, R. Bro, and B. Yener. Multiway analysis of epilepsy tensors. *Bioinformatics*, 23:10–18, 2007.

[3] R. Agarwal, J. Gotman, D. Flannagan, and B. Rosenblatt. Automatic EEG analysis during long-term monitoring in the ICU. *Electroencephalogr Clin Neurophysiol*, 107:44–58, 1998.

[4] M. Atit, J. Hagan, R. Bansal, R. Ichord, R. Geocadin, C. Hansen, D. Scherman, and N. Thakor. EEG burst detection: Performance evaluation. *Proceedings of the first joint BMES/EMBS conference serving humanity, advancing technology.*, 1:441, 1999.

[5] D. Azzopardi, N.J. Robertson, F.M. Cowan, M.A. Rutherford, M. Rampling, and D. Edwards. Pilot study of treatment with whole-body hypothermia for neonatal encephalopathy. *Pediatrics*, 106:684–694, 2000.

[6] B.W. Bader and T. Kolda. Algorithm 862: Matlab tensor classes for fast algorithm prototyping. *ACM Transactions on Mathematical Software*, 32:635–653, 2006.

[7] S. Baillet, J. Mosher, and R. Leahy. Electromagnetic brain mapping. *IEEE Signal Proc. Mag.*, 18:14–30, 2001.

[8] T. Bast, T. Boppel, A. Rupp, I. Harting, K. Hoechstetter, S. Fauser, A. Schulze-Bonhage, D. Rating, and M. Scherg. Noninvasive source localization of interictal EEG spikes: effects of signal-to-noise ratio and averaging. *Clin Neurophysiol*, 23:487–497, 2006.

[9] A. Belouchrani, K. Abed-Meraim, J.F. Cardoso, and E. Moulines. A blind source separation technique using second order statistics. *IEEE Trans. Signal Proc.*, 45:434–444, 1997.

[10] E. Biagioni, L. Bartalena, A. Boldrini, R. Pieri, and G. Cioni. Constantly discontinuous EEG patterns in full-term neonates with hypoxic-ischaemic encephalopathy. *Clin Neurophysiol*, 110:1510–1515, 1999.

[11] E. Biagioni, E. Mercuri, M. Rutherford, F. Cowan, D. Azzopardi, M. Frizone, G. Cioni, and L. Dubovic. Combined use of electroencephalogram and magnetic resonance imaging in full-term neonates with acute encephalopathy. *Pediatrics*, 107:461–468, 2001.

[12] G. Bodenstein, W. Schneider, and C.V.D. Malsburg. Computerized eeg pattern classification by adaptive segmentation and probability-density-function classification. *Comput. Biol. Med.*, 15:297–313, 1985.

[13] C. Borel and D. Hanley. Neurological intensive care unit monitoring. In M.C. Robers and R.J. Traysman, editors, *Critical Care Clinics. Symposium on neurological intensive care*, pages 223–239. Saunders, Philadelphia, 1985.

[14] I.F. Borghese, Minard K.L., and Thoman E.B. Sleep rhythmicity in premature infants: implications for developmental status. *Sleep*, 18:523–530, 1995.

[15] N.I.O. Braga, G.M. Manzano, and J.A.M. Nobrega. A comparison between averaged spikes and individual visually-analyzed spikes in rolandic epileptiform discharges. *Arq. Neuropsiquiatr.*, 60:699–701, 2002.

[16] M. Burioka, N. Miyata, G. Cornelissen, F. Halber, T. Takeshima, D. Kaplan, H. Suyama, M. Endo, Y. Maegaki, T. Nomura, Y. Tomita, K. Nakashima, and E. Shimizu. Approximate entropy in the electroencephalogram during wake and sleep. *Clin EEG Neurosci.*, 36:21–24, 2005.

[17] A. Bye and D. Flanagan. Electroencephalograms, clinical observations and the monitoring of neonatal seizures. *J Paediatr Child Health*, 31:503–507, 1995.

[18] A.M. Bye, C.A. Cunningham, K.Y. Chee, and D. Flanagan. Outcome of neonates with electrographically identified seizures, or at risk of seizures. *Pediatr Neurol*, 16:225–231, 1997.

[19] A.M. Bye and D. Flanagan. Spatial and temporal characteristics of neonatal seizures. *Epilepsia*, 36:1009–1016, 1995.

[20] J.-F. Cardoso. The three easy routes to independent component analysis: contrasts and geometry. In *Proceedings of ICA*, 2001.

[21] J.F. Cardoso and A. Souloumiac. Blind beamforming for non-gaussian signals. *IEE Proceedings-F*, 140:362–370, 1993.

[22] J.D. Carroll and J. Chang. Analysis of individual differences in multidimensional scaling via an n-way generalization of 'Eckart-Young' decomposition. *Psychometrika*, 35:283–319, 1970.

[23] R. Cattell. Parallel proportional profiles and other principles for determining the choice of factors by rotation. *Psychometrika*, 9:267–283.

[24] P. Celka and P. Colditz. A computer-aided detection of EEG seizures in infants: a singular spectrum approach and performance comparison. *IEEE Trans Biomed Eng*, 49:455–462, 2002.

[25] M.A. Chadd and O.P. Gray. Hypothermia and coagulation defects in the newborn. *Arch Dis Child*, 41.

[26] P.J. Cherian, J.H. Blok, R.M. Swarte, P. Govaert, and G.H. Visser. Heart rate changes are insensitive for detecting postasphyxial seizures in neonates. *Neurology*, 67:2221–2223, 2006.

[27] S. Choi, A. Cichocki, H. Park, and S. Lee. Blind source separation and independent component analysis: a review. *Neural Information Processing - Letters and Reviews*, 6:1–57, 2005.

[28] R.R. Clancy and A. Legido. Postnatal epilepsy after EEG-confirmed neonatal seizures. *Epilepsia*, 32:69–76, 1991.

[29] R.R. Clancy, A. Legido, and D. Lewis. Occult neonatal seizures. *Epilepsia*, 29:256–261, 1988.

[30] W. De Clercq. *Advanced preprocessing techniques and nonlinear signal analysis applied to scalp electroencephalograms for the prediction of epileptic seizures*. PhD thesis, Faculty of Engineering, K.U.Leuven, 2005.

[31] G.L. Clifton, S. Allen, and P. Barrodale. A phase ii study of moderate hypothermia in severe brain injury. *J Neurotrauma*, 10:263–271, 1993.

[32] R.W. Coen, C.B. McCutchen, D. Wermer, J. Snyder, and F.E. Gluck. Continuous monitoring of the electroencephalogram following perinatal asphyxia. *J Pediatr*, 100:628–630, 1982.

[33] A. Coenen, O. Zajachkivisky, and R. Bilski. In the footsteps of beck: the desynchronization of the electroencephalogram. *Electroencephalography and Clinical Neurophysiology*, 106:330–335, 1998.

[34] P. Comon. Independent component analysis, a new concept? *Signal Processing*, 36:287–314, 1994.

[35] P. Comon. Blind identification and source separation in 2×3 underdetermined mixtures. *IEEE Trans. Signal Process.*, 52:11–22, 2004.

[36] P. Comon and C. Jutten. *Handbook of Blind Source Separation: Independent Component Analysis and applications.* Academic Press, 2010.

[37] G. Compagnoni, L. Pogliani, G. Lista, F. Castoldi, P. Fontana, and F. Mosca. Hypothermia reduces neurological damage in asphyxiated newborn infants. *Biol Neonate*, 82:222–227, 2002.

[38] J. Connell, R. Oozeer, and L. de Vries. Continuous EEG monitoring of neonatal seizures: diagnostic and prognostic considerations. *Arch Dis Child*, 64:452–458, 1989.

[39] G. Darmois. Analyse générale des liaisons stochastiques. *Rev. Inst. Intern. Stat.*, 21:2–8, 1953.

[40] W. De Clercq, A. Vergult, B. Vanrumste, W. Van Paesschen, and S. Van Huffel. Canonical Correlation analysis applied to remove muscle artifacts from the electroencephalogram. *IEEE Trans Biomed Eng*, 53:2583–2587, 2006.

[41] L. De Lathauwer, B. De Moor, and J. Vandewalle. An introduction to independent component analysis. *Journal of Chemometrics*, 14:123–149, 2000.

[42] M. De Vos, L. De Lathauwer, B. Vanrumste, S. Van Huffel, and W. Van Paesschen. Canonical decomposition of ictal scalp EEG and accurate source localisation: Principles and simulation study. *Computational Intelligence and Neuroscience*, 58253, 2007.

[43] M. De Vos, A. Vergult, L. De Lathauwer, W. De Clercq, S. Van Huffel, P. Dupont, A. Palmini, and W. Van Paesschen. Canonical decomposition of ictal scalp EEG reliably detects the seizure onset zone. *NeuroImage*, 37:844–854, 2007.

[44] L.S. de Vries and L. Hellstrom-Westas. Role of cerebral function monitoring in the newborn. *Arch Dis Child Fetal Neonatal Ed*, 90:201–207, 2005.

[45] W. Deburchgraeve, P.J. Cherian, M. De Vos, R.M. Swarte, J.H. Blok, G.H. Visser, P. Govaert, and S. Van Huffel. Time varying neonatal seizure localization. *Methods of Information in Medicine*, accepted for publication.

[46] W. Deburchgraeve, P.J. Cherian, M. De Vos, R.M. Swarte, J.H. Blok, G.H. Visser, P. Govaert, and S. Van Huffel. Automated neonatal seizure detection mimicking a human observer reading EEG. *Clin Neurophysiol*, 119:2447–2454, 2008.

[47] W. Deburchgraeve, P.J. Cherian, M. De Vos, R.M. Swarte, J.H. Blok, G.H. Visser, P. Govaert, and S. Van Huffel. Neonatal seizure localization using PARAFAC decomposition. *Clin Neurophysiol*, 120:17871796, 2009.

[48] N. Delfosse and P. Loubaton. Adaptive blind separation of independent sources: a deflation approach. *Signal Processing*, 45:59–83, 1995.

[49] M.R. DeLucci, B. Garoutte, and R.B. Aird. The scalp as an electroencephalographic averager. *Electroencephalogr. Clin. Neurophysiol.*, 14:191–196, 1962.

[50] I. Despotovic, W. Deburchgraeve, H. Hallez, E. Vansteenkiste, and W. Philips. Development of a realistic head model for EEG event-detection and source localization in newborn infants.. *Conf Proc IEEE Eng Med Biol Soc.*, 1:2296–2299, 2009.

[51] J.S. Ebersole and T.A. Pedley. *Current Practice of Clinical Electroencephalography.* Lippincott Williams and Wilkins, 2003.

[52] C. Eckart and G. Young. The approximation of one matrix by another of lower rank. *Psychometrika*, 1:211–218, 1936.

[53] A.S. El Radhi, M.H. Jawad, and M. Ibrahim. Infection in neonatal hypothermia. *Arch Dis Child*, 58:143–145, 1983.

[54] P.H. Ellison, J.A. Largent, and J.P. Bahr. A scoring system to predict outcome following neonatal seizures. *J Pediatr.*, 99:455–459, 1981.

[55] R.G. Emmerson and K.H. Chiappa. Electrophysiologic monitoring. In A.H. Ropper, S.K. Kennedy, and N.T. Zervas, editors, *Neurological Neurosurgical Intensive Care*. Aspen, Rockville, second edition, 1988.

[56] F. Estienne, N. Matthijs, D.L. Massart, P. Ricoux, and D. Leibovici. Multi-way modelling of high-dimensionality electroencephalographic data. *Chemometrics and Intelligent Laboratory Systems*, 58:59–72, 2001.

[57] D. Evans and M. Levene. Neonatal seizures. *Arch. Dis. Child. Fetal Neonatal*, 78:70–75, 1998.

[58] S. Faul, G. Boylan, S. Connolly, L. Marnane, and G. Lightbody. An evaluation of automated neonatal seizure detection methods. *Clin Neurophysiol*, 116:1533–1541, 2005.

[59] C.E. Fernandes, G. Favier, and J.C. Mota. Blind channel identification algorithms based on the parafac decomposition of cumulant tensors: The single and multiuser cases. *Signal Processing*, 88:1382–1401, 2008.

[60] A.S. Field and D. Graupe. Topographic component (parallel factor) analysis of multichannel evoked potentials: Practical issues in trilinear spatiotemporal decomposition. *Brain Topography*, 3:407–423, 1991.

[61] B.J. Fisch. The source of the EEG. In *Fisch and Spelhmann's EEG Primer*, chapter 1, pages 3–17. Elsevier, third edition, 1999.

[62] B.J. Fisch. Spatial analysis of the EEG. In *Fisch and Spelhmann's EEG Primer*, chapter 4, pages 73–106. Elsevier, third edition, 1999.

[63] O. Friman. *Adaptive Analysis of Functional MRI Data.* PhD thesis, Linköping University, Sweden, 2003.

[64] V. Gerla, K. Paul, and L. Lhotska. Multivariate analysis of full-term neonatal polysomnographic data. *IEEE Transactions on information technology in biomedicine*, 13:104–110, 2009.

[65] A. Gibson, R. H. Bayford, and D. S. Holder. Two-dimensional finite element modelling of the neonatal head. *Physological Measurement*, 21:45–52, 2000.

[66] P. Gloor. Neuronal generators and the problem of localization in electroencephalography: applications of volume conductur theory to electroencephalography. *J. Clin. Neurophysiol.*, 2:327–354, 1985.

[67] P.D. Gluckman, J.S. Wyatt, D. Azzopardi, R. Ballard, A.D. Edwards, D.M. Ferriero, R.A. Polin, C.M. Robertson, M. Thoresen, A. Whitelaw, and A.J. Gunn. Selective head cooling with mild systemic hypothermia after neonatal encephalopathy: multicentre randomised trial. *Lancet*, 365:663–670, 2005.

[68] J. Gotman, D. Flanagan, J. Zhang, and B. Rosenblatt. Automatic seizure detection in the newborn: methods and initial evaluation. *Electroencephalogr Clin Neurophysiol*, 103:356–363, 1997.

[69] B.R. Greene, G.B. Boylan, R.B. Reilly, P. de Chazal, and S. Connolly. Combination of EEG and ECG for improved automatic neonatal seizure detection. *Clin Neurophysiol*, 118:356–362, 2007.

[70] B.R. Greene, P. Chazal, G. Boylan, R.B. Reilly, C. O' Brien, and S. Connolly. Heart and respiration changes in the neonate during electroencephalographic seizure. *Med. Biol. Eng. Comput.*, 44:27–34, 2006.

[71] A.J. Gunn, T.R. Gunn, and M.I. Gunning. Neuroprotection with prolonged head cooling started before post-ischemic seizures in fetal sheep. *Pediatrics*, 102:1098–1106, 1998.

[72] Berger H. ber das Elektrenkephalogramm des Menchen. *Arch. Psychiatr. Nervenk.*, 87:527–570, 1929.

[73] H. Hallez, M. De Vos, B. Vanrumste, P. Van Hese, S. Assecondi, K. Van Laere, P. Dupont, W. Van Paesschen, S. Van Huffel, and I. Lemahieu. Removing muscle and eye artifacts using blind source separation techniques in ictal EEG source imaging. *Clin Neurophysiol.*, 120:1262–1272, 2009.

[74] H. Hallez, B. Vanrumste, P. Van Hese, Y. D' Asseler, I. Lemahieu, and R. Van de Walle. A finite difference method with reciprocity used to incorporate anisotropy in electroencephalogram dipole source localization. *Physics in Medicine and Biology*, 50:3787–3806, 2005.

[75] H. Hallez, A. Vergult, R. Phlypo, W. De Clercq, Y. D' Asseler, R. Van de Walle, B. Vanrumste, W. Van Paesschen, S. Van Huffel, and I. Lemahieu. Muscle and eye movement artifact removal prior to EEG source localization. In *Proceedings of IEEE EMBS*, pages 2002–2005, New York, 2006.

[76] L.F. Halpern, W.E. MacLean, and A.A. Baumeister. Infant sleep-wake characteristics: relation to neurological status and the prediction of developmental outcome. *Dev Rev*, 15:255–291, 1995.

[77] R.A. Harshman. Foundations of the Parafac procedure: models and conditions for an 'explanatory' multi-modal factor analysis. *UCLA Working Papers in Phonetics*, 16, 1970.

[78] L. Hellstrom-Westas. Midazolam and amplitude-integrated EEG. *Acta Paediatr*, 93:1153–1155, 2004.

[79] L. Hellstrom-Westas, H. Klette, K. Thorngren-Jerneck, and I. Rosen. Early prediction of outcome with aEEG in preterm infants with large intravenctricular hemorrhages. *Neuropediatrics*, 32:319–324, 2001.

[80] L. Hellstrom-Westas and I. Rosen. Continuous brain-function monitoring: State of the art in clinical practice. *Seminars in Fetal and Neonatal Medicine*, 11:503–511, 2006.

[81] L. Hellstrom-Westas, I. Rosen, L.S. de Vries, and G. Greisen. Amplitude-integrated EEG classification and interpretation in preterm and term infants. *NeoReviews*, 7:76–87, 2006.

[82] L. Hellstrom-Westas, I. Rosen, and N.W. Swenningsen. Silent seizures in sick infants in early life. Diagnosis by continuous cerebral function monitoring. *Acta. Paediatr. Scand.*, 74:741–748, 1985.

[83] L. Hellstrom-Westas, I. Rosen, and N.W. Swenningsen. Predictive value of early continuous amplitude integrated EEG recordings on outcome after severe birth asphyxia in full term infants. *Arch Dis Child Fetal Neonatal Ed*, 72:34–38, 1995.

[84] F.L. Hitchcock. Multiple invariants and generalized rank of a p-way matrix or tensor. *J. Math. Phys.*, 7:39–79.

[85] F.L. Hitchcock. The Expression of a Tensor or a Polyadic as a Sum of Products. *J. Math. Phys.*, 6:164–189.

[86] R.E. Hoekstra, B. Ferrara, R.J. Couser, N.R. Payne, and J.E. Connett. Survival and long-term neurodevelopmental outcome of extremely premature infants born at 23-26 weeks gestational age at a tertiary center. *Pediatrics*, 113:1–6, 2004.

[87] K.R. Holden, E.D. Mellits, and J.M. Freeman. Correlation of prenatal and perinatal events with outcomes. *Pediatrics*, 70:165–176, 1982.

[88] G.L. Holmes and Y. Ben-Ari. Seizures in the developing brain: perhaps not so benign after all. *Neuron*, 21:1231–1234, 1998.

[89] G.L. Holmes and C.T. Lombroso. Prognostic value of background patterns in neonatal EEG. *J Clin Neurophysiol*, 10:323–352, 1993.

[90] H. Hotelling. Relations between two sets of variates. *Biometrika*, 28:321–371, 1936.

[91] A. Hyvarinen. Fast and robust fixed-point algorithm for independent component analysis. *IEEE Transactions on Neural Networks*, 10:419–433, 1999.

[92] A. Hyvarinen, J. Karhunen, and E. Oja. *Independent Component Analysis*. John Wiley & Sons, 2001.

[93] R. Jamasebi, S. Redline, S.R. Patel, and K.A. Loparo. Entropy-based measures of EEG arousals as biomarkers for sleep dynamics: applications to hypertension. *Sleep*, 31:935–943, 2008.

[94] C.J. James and C.W. Hesse. Independent component analysis for biomedical signals. *Physiol. Meas.*, 26:15–39, 2004.

[95] H.H. Jasper. The Ten-Twenty Electrode System of the International Federation. *Electroenceph. clin Neuropysiol.*, 10:367–380, 1958.

[96] K.B. Johnson, W.P. Wiesmann, and F.J. Pearce. The effect of hypothermia on potassium and glucose changes in isobaric hemorrhagic shock in the rat. *Shock*, 6:223–229, 1996.

[97] I.T. Jolliffe. *Principal Component Analysis*. Springer, 2002.

[98] C.A. Joyce, I.F. Gorodnitsky, and M. Kutas. Automatic removal of eye movements and blink artefacts from EEG data using blind component separation. *Psychophysiology*, 41:313–325, 2004.

[99] J.F. Kaiser. On a simple algorithm to calculate the energy of a signal. *IEEE Int Conf Acoust Speech Signal Process (ICASSP)*, pages 381–384, 1990.

[100] F.H. Kern and P.R. Hickey. *Cardiopulmonary bypass in neonates, infants and young children.* Oxford: Butterworth-Heinemann, 1994.

[101] R.L. Khan, M.L. Nunes, L.F.G. da Silva, and J.C. da Costa. Predictive value of sequential electroencephalogram (EEG) in neonates with seizures and its relation to neurological outcome. *J Child Neurol*, 23:144–150, 2007.

[102] H. Kiers. Towards a standardized notation and terminology in multiway analysis. *Journal of Chemometrics*, 14:105–122, 2000.

[103] L.G. Kiloh, A.J.Mc Comas, and J.W. Osselton. *Clinical Electroencephalography.* Butterworths, 1981.

[104] M. Klemm, J. Haueisen, and G. Ivanova. Independent component analysis: comparison of algorithms for the investigation of surface electrical brain activity. *Med. Biol. Eng. Computing*, 47:413–423, 2009.

[105] K. Kobayashi, H. Yoshinaga, Y. Ohtsuka, and J. Gotman. Dipole modeling of epileptic spikes can be accurate or misleading. *Epilepsia*, 46:397–408, 2005.

[106] T. Koenig, F. Marti-Lopez, and P. Valdes-Soas. Topographic time-frequency decomposition of the EEG. *NeuroImage*, 14:383–390, 2001.

[107] I. Korotchikova, S. Connolly, C.A. Ryan, D.M. Murray, A. Temko, B.R. Greene, and G.B. Boylan. EEG in the healthy term newborn within 12 hours of birth. *Clin Neurophysiol*, 120:1046–1053, 2009.

[108] I. Kostovic and N. Jovanov-Milosevic. The development of cerebral connections during the first 20 to 45 weeks gestation. *Semin Fetal Neonatal Med*, 11:415–422, 2006.

[109] N. Kovacevic and A.R. McIntosh. Groupwise independent component decomposition of EEG data and partial least square analysis. *NeuroImage*, 35:1103–1112, 2007.

[110] P.M. Kroonenberg. *Applied Multiway Data Analysis.* John Wiley & Sons, 2008.

[111] H. Lagercrantz, M. Hanson, P. Evrard, and C. Rodeck. *The newborn brain: Neuroscience and clinical applications.* Cambridge University Press, 2001.

[112] M.J. Lanska and D.J. Lanska. Neonatal seizures in the united states: results of the national hospital discharge survey, 19801991. *Neuroepidemiology*, 15:117–125, 1996.

[113] L. De Lathauwer and J. Castaing. Blind identification of underdetermined mixtures by simultaneous matrix diagonalization. 56:1096–1105, 2008.

[114] A. Legido, R.R. Clancy, and P.H. Berman. Neurologic outcome after electroencephalographically proven neonatal seizures. *Pediatrics*, 88:583–596, 1991.

[115] P. Lemmers. *The clinical use of near infrared-monitored cerebral oxygen saturation and extraction in the preterm infant.* PhD thesis, Utrecht University, 2010.

[116] A. Liu, J.S. Hahn, G.P. Heldt, and R.W. Coen. Detection of neonatal seizures through computerized EEG analysis. *Electroencephalogr Clin Neurophysiol*, 82:363–369, 1992.

[117] J. Lofhede, N. Lofgren, M. Thordstein, A. Flisberg, I. Kjellmer, and K. Lindecrantz. Classification of burst and suppression in the neonatal electroencephalogram. *J. Neural Eng.*, 5:402–410, 2008.

[118] C.T. Lombroso. Prognosis in neonatal seizures. *Adv Neurol.*, 34:101–113, 1983.

[119] C.T. Lombroso. Neonatal polygraphy in full-term and premature infants: a review of normal and abnormal findings. *J Clin Neurophysiol*, 2:105–155, 1985.

[120] C.T. Lombroso. Neonatal seizures: a clinician's overview. *Brain Dev*, 18:1–28, 1996.

[121] P. Mahon, B.R. Green, E.M. Lynch, B. McNamara, and G.D. Shorten. Can state or reponse entropy be used as a measure of sleep depth? *Anaesthesia*, 63:1309–1313, 2008.

[122] P. Mahon, B.R. Greene, C. Greene, G.B. Boylan, and G.D. Shorten. Behaviour of spectral entropy, spectral edge frequency 90%, and alpha and beta power parameters during low-dose propofol infusion. *British Journal of Anaesthesia*, 101:213–221, 2008.

[123] M.B. Malarvili and M. Mesbah. Newborn seizure detection based on heart rate variability. *IEEE Trans. Biomed. Eng.*, 56:2594–2603, 2009.

[124] J. Malmivuo and R. Plonsey. *Bioelectromagnetism: Principles and Applications of Bioelectric and Biomagnetic Fields.* Oxford University Press, New York, 1995.

[125] A. Malone, C.A. Ryan, A. Fitzgerald, L. Burgoyne, S. Connolly, and G.B. Boylan. Interobserver agreement in neonatal seizure identification. *Epilepsia*, 50:2097–2101, 2009.

[126] D.E. Maynard, P.F. Prior, and D.F. Scott. Device for continuous monitoring of cerebral activity in resuscitated patients. *Br. Med. J.*, 4:545–546, 1969.

[127] M.C. McBride, N. Laroia, and R. Guillet. Electrographic seizures in neonates correlate with poor neurodevelopmental outcome. *Neurology*, 55:506–514, 2000.

[128] E.D. Mellitis, K.R. Holden, and J.M. Freeman. Neonatal seizures ii. a multivariate analysis of factors associated with outcome. *Pediatrics*, 70:177–185, 1983.

[129] C.C. Menache, B.F.D. Bourgeois, and J.J. Volpe. Prognostic value of neonatal discontinuous EEG. *Pediatric Neurol*, 27:93–101, 2002.

[130] E. Mercurie, M. Rutherford, F. Cowan, J. Pennock, S. Counsell, M. Papadimitriou, D. Azzopardi, G. Bydder, and L. Dubowithz. Early prognostic indicators of outcome in infants with neonatal cerebral infarction: A clinical, electroencephalogram, and magnetic resonance imaging study. *Pediatrics*, 103:39–46, 1999.

[131] I. Merlet and J. Gotman. Reliability of dipole models of epileptic spikes. *Clin Neurophysiol*, 110:1013–1028, 1999.

[132] C. Michel, M. Murray, G. Lantz, S. Gonzales, L. Spinelli, and R. Grave de Peralta. EEG source imaging. *Clin Neurophysiol*, 115:2195–2222, 2004.

[133] S.P. Miller, J. Weiss, and A. Barnwell. Seizure-associated brain injury in term newborns with perinatal asphyxia. *Neurology*, 58:542–548, 2002.

[134] F. Miwakeichi, E. Martínez-Montes, P.A. Valdès-Sosa, N. Nishiyama, H. Mizuhara and Y. Yamaguchi. Decomposing EEG data into space-time-frequency components using parallel factor analysis. *Neuroimage*, 22:1035–1045, 2004.

[135] E.M. Mizrahi and P. Kellaway. Characterization and classification of neonatal seizures. *Neurology*, 37:1837–1844, 1987.

[136] E.M. Mizrahi and P. Kellaway. *Diagnosis and management of neonatal seizures.* Philadelphia: Lippincott-Raven, 1998.

[137] J. Möks. Topographic components model for event-related potentials and some biophysical considerations. 35:482–484, 1988.

[138] N. Monod, N. Pajot, and S. Guidasci. The neonatal EEG: statistical studies and prognostic value in full-term and preterm babies. *Electroencephalogr Clin Neurophysiol*, 32:529–544, 1972.

[139] J.P. Morray and E.G. Pavlin. Oxygen delivery and consumption during hypothermia and rewarming in dogs. *Anesthesiology*, 72:510516, 1990.

[140] D.M. Murray, G.B. Boylan, I. Ali, C.A. Ryan, B.P. Murphy, and S. Connolly. Defining the gap between electrographic seizure burden, clinical expression and staff recognition of neonatal seizures. *Arch. Dis. Child. Fetal Neonatal*, 93:187–191, 2008.

[141] T. Nakada. *Integrated Human Brain Science.* Elsevier, 2000.

[142] H. Nam, T.G. Yim, S.K. Han, J.B. Oh, and S.K. Lee. Independent component analysis of ictal EEG in medial temporal lobe epilepsy. *Epilepsia*, 43:160–164, 2002.

[143] M.A. Navakatikyan, P.B. Colditz, C.J. Burke, T.E. Inder, J. Richmond, and C.E. Williams. Seizure detection algorithm for neonates based on wave-sequence analysis. *Clin Neurophysiol*, 117:1190–1203, 2006.

[144] E. Niedermeyer and F.L. da Silva. *Electroencephalography: Basic Principles, Clinical Applications, and Related Fields.* Lippincott Williams and Wilkins, 2004.

[145] D. Nion and N.D. Sidiropoulos. Adaptive algorithms to track the parafac decomposition of a third-order tensor. *IEEE Trans on Signal Processing*, 57:2299–2310, 2009.

[146] P.L. Nunez. *Electric fields of the brain.* Oxford, 1981.

[147] M.R. Nuwer, G. Comi, R. Emmerson, and et al. IFCN standards for digital recording of clinical EEG. *Electroencephalogr. Clin. Neurophysiol*, 106:259–261, 1998.

[148] M. Okada. The cardiac rhythm in accidental hypothermia. *J Electrocardiol*, 17:123–128, 1984.

[149] P. Olejniczak. Neurophysiologic basis of EEG. *J Clin Neurophysiol*, 23:186–189, 2006.

[150] J. Onton, M. Westerfield, J. Townsend, and S. Makeig. Imaging human EEG dynamics using independent component analysis. *Neuroscience and Biobehavioral Reviews*, 30:808–822, 2006.

[151] D. Osredkar, M.C. Toet, L.G.M. van Rooij, A.C. van Huffelen, F. Groenendaal, and L.S. de Vries. Sleep-wake cycling on amplitude-integrated electroencephalography in term newborns with hypoxic ischemic encephalopathy. *Pediatrics*, 115:327–332, 2005.

[152] M.J. Painter, I. Bergman, and P. Crumrine. Neonatal seizures. *Pediatr Clin North Am.*, 33:91–109, 1986.

[153] K. Palmu, S. Wikstrom, E. Hippelainen, G. Boylan, L. Hellstrom-Westas, and S. Vanhatalo. Detection of 'EEG bursts' in the early preterm EEG: visual vs. automated detection. *Clin Neurophysiol*, 121:1015–1022, 2010.

[154] J.M. Palva, S. Palva, and K. Kaila. Phase synchrony among neuronal oscillations in the human cortex. *Journal of Neuroscience*, 25:3962–3972, 2005.

[155] C. Papadelis, Z. Chen, C. Kourtidou-Papadeli, P. Bamidis, I. Chouvarda, and E. Bekiaris. Monitoring sleepiness with on-board electrophysiological recordings for preventing sleep-deprived traffic accidents. *Clin Neurophysiol*, 118:1906–1922, 2007.

[156] R. Pascual-Marqui, C. Michel, and D. Lehman. Low resolution electromagnetic tomography: a new method for localizing the electrical activity in the brain. *Int. J. Psychophysiol.*, 18:49–65, 1994.

[157] A. Patel, F. Alotaibi, W.T. Blume, and S.M. Mirsattari. Independent component analysis of subdurally recorded occipital seizures. *Clin Neurophysiol*, 119:2437–2446, 2008.

[158] S. Patrizi, L.G. Holmes, M. Orzalesi, and F. Allemand. Neonatal seizures: characteristics of EEG ictal activity in preterm and fullterm infants. *Brain Dev*, 25:427–437, 2003.

[159] K. Pearson. On lines and planes of closest fit to systems of points in space. *Philosophical Magazine*, 2:559–572, 1901.

[160] J.M. Perlman. Summary proceedings from the neurology group on hypoxic-ischemic encephalopathy. *Pediatrics*, 117:28–33, 2006.

[161] J.C. Perumpillichira, R.M. Swarte, and G.H. Visser. Technical standards for recording and interpretation of neonatal electroencephalogram in clinical practice. *Ann Indian Acad Neurol*, 12:58–70, 2009.

[162] C. Pezzani, M.F. Radvanyi-Bouvet, J.P. Relier, and N. Monod. Neonatal electroencephalography during the first twenty-four hours of life in full-term newborn infants. *Neuropediatrics*, 17:11–18, 1986.

[163] D.L. Pham and J.L. Prince. Adaptive fuzzy segmentation of magnetic resonance images. *IEEE Transactions on Medical Imaging*, 9:737–752, 1999.

[164] F. Pisani, C. Copioli, C. Di Gioia, E. Turco, and L. Sisti. Neonatal seizures: relation of ictal video-electroencephalography (EEG) findings with neurodevelopmental outcome. *J Child Neurol*, 23:394–398, 2008.

[165] F. Pisani, M. Orsini, S. Braibanti, C. Copioli, L. Sisti, and E.C. Turco. Development of epilepsy in newborns with moderate hypoxic ischemic encephalopathy and neonatal seizures. *Brain Dev*, 31:64–68, 2009.

[166] E.I. Plotkin and M.N.S. Swamy. Nonlinear signal processing based on parameter invariant moving average modeling. *Proc CCECE 21*, 1992.

[167] M. Prastawa, J.H. Gilmore, W. Lin, and G. Gerig. Automatic segmentation of MR images of the developing newborn brain. *Med Image Anal*, 9:457–466, 2005.

[168] R.M. Pressler, G.B. Boylan, M. Morton, C.D. Binnie, and J.M. Rennie. Early serial EEG in hypoxic ischaemic encephalopathy. *Clin Neurophysiol*, 112:31–37, 2001.

[169] P.F. Prior and D.E. Maynard. *Monitoring cerebral function*. Elsevier, 1986.

[170] M. Raichle. The pathophysiology of brain ischemia. *Annals of Neurology*, 13:1–10, 1983.

[171] I.J. Rampil. A primer for EEG signal processing in anesthesia. *Anesthesiology*, 89:980–1002, 1998.

[172] I.J. Rampil, R.B. Weiskopf, J.G. Brown, E.I. Eger, B.H. Johnson, M.A. Holmes, and J.H. Donegan. l653 and isoflurane produce similar dose-related changes in the electroencephalogram of pigs. *Anesthesiology*, 69:298–302, 1988.

[173] J.M. Rennie, G. Chorley, G.B. Boylan, R. Pressler, Y. Nguyen, and R. Hooper. Non-expert use of the cerebral function monitor for neonatal seizure detection. *Arch Dis Child Fetal Neonatal Ed*, 89:37–40, 2004.

[174] M.W. Risinger. Electroencephalographic strategies for determining the epileptogenic zone. In H. Lüders, editor, *Epilepsy Surgery*, pages 337–347. Raven Press, 1991.

[175] R.L. Robertsona, L. Ben-Siraa, P.D. Barnesa, R.V. Mulkerna, C.D. Robsona, S.E. Maiera, M.J. Rivkina, and A.J. Plessisa. MR line-scan diffusion-weighted imaging of term neonates with perinatal brain ischemia. *Am J Neuroradiol*, 20:1658–1670, 1999.

[176] M. Rutherford, L. Srinivasan, L. Dyet, P. Ward, J. Allsop, S. Counsell, and F. Cowan. Diffusion-weighted magnetic resonance imaging in term perinatal brain injury: a comparison with site of lesion and time from birth. *Pediatrics*, 114:1004–1014, 2004.

[177] E. Salinas and T.J. Sejnowski. Correlated neuronal activity and the flow of neural information. *Nature Review Neuroscience*, 2:539–550, 2001.

[178] M. Sarkela, S. Mustola, T. Seppanen, M. Koskinen, P. Lepola, K. Suominen, T. Juvonen, H. Tolvanen-Laakso, and V. Jantti. Automatic analysis and monitoring of burst suppression in anesthesia. *Journal of Clincical Monitoring and Computing*, 17:125–134, 2002.

[179] N. Schaul. The fundamental neural mechanisms of electroencephalography. *Electroencephalography and clinical neurophysiology*, 106:101–107, 1998.

[180] M.S. Scher. Seizures in the newborn infant. Diagnosis, treatment and outcome. *Clin Perinatol*, 24:735–772, 1997.

[181] M.S. Scher. Neonatal seizures and brain damage. *Pediatric Neurology*, 29:381–390, 2003.

[182] M.S. Scher, K. Aso, M.E. Beggarly, M.Y. Hamid, D.A. Steppe, and M.J. Painter. Electrographic seizures in preterm and full-term neonates: clinical correlates, associated brain lesions, and risk for neurologic sequelae. *Pediatrics*, 91:128–134, 1993.

[183] M. Scherg and D. von Cramon. Two bilateral sources of the late AEP as identified by a spatio-temporal dipole model. *Electroencephalogr. Clin. Neurophysiol.*, 62:32–44, 1985.

[184] D.L. Scherman, A.M. Brambrink, D. Walterspacher, V.K. Dasika, R. Ichord, and N.V. Thakor. Detecting EEG bursts after hypoxic-ischemic injury using energy operators. *Proceedings of the 19th annual international conference of the IEEE/EMBS*, 3:1188–1190, 1997.

[185] S. Shankaran, A.R. Laptook, R.A. Ehrenkranz, J.E. Tyson, S.A. McDonald, E.F. Donovan, A.A. Fanaroff, W.K. Poole, L.L. Wright, R.D. Higgins, N.N. Finer, W.A. Carlo, S. Duara, W. Oh, C.M. Cotten, D.K. Stevenson, B.J. Stoll, J.A. Lemons, R. Guillet, and A.H. Jobe. Whole-body hypothermia for neonates with hypoxic-ischemic encephalopathy. *N Engl J Med*, 353:1574–1584, 2005.

[186] C.E. Shannon. A mathematical theory of communication. *Bell System Technical Journal*, 27:379–43 & 623–656, 1948.

[187] D.A. Shewmon. What is a neonatal seizure? Problems in definition and quantification for investigative and clinical purposes. *J Clin Neurophysiol*, 118:2798–2804, 2007.

[188] H.C. Shin, X. Jia, R. Nickl, R.G. Geocadin, and N.V. Thakor. A subband-based information measure of EEG during brain injury and recovery after cardiac arrest. *IEEE Trans. Biomed. Eng.*, 55:1985–1990, 2008.

[189] N. D. Sidiropoulos, R. Bro, and G. B. Giannakis. Parallel factor analysis in sensor array processing. *IEEE Trans. Signal Process.*, 48:2377–2388, 2000.

[190] N. D. Sidiropoulos, G. B. Giannakis, and R. Bro. Blind PARAFAC receivers for DS-CDMA systems. *IEEE Trans. Signal Process.*, 48:810–823, 2000.

[191] G. Simbruner, C. Haberl, V. Harrison, L. Linley, and A.E. Willeitner. Induced brain hypothermia in asphyxiated human newborn infants: A retrospective chart analysis of physiological and adverse effects. *Intensive Care Med*, 25:1111–1117, 1999.

[192] D.B. Sinclair, M. Campbell, P. Byrne, W. Prasertsom, and C.M.T. Robertson. EEG and long-term outcome of term infants with neonatal hypoxic ischemic encephalopathy. *Clin Neurophysiol*, 110:655–659, 1999.

[193] A. Smilde, R. Bro, and P. Geladi. *Multi-way Analysis with applications in the Chemical Sciences*. John Wiley & Sons, 2004.

[194] J.S. Soul, R.L. Robertson Dagger, A.A. Tzika Dagger, A.J. Plessis, and J.J. Volpe. Time course of changes in diffusion weighted magnetic resonance imaging in a case of neonatal encephalopathy with defined onset and duration of hypoxic-ischemic insult. *Pediatrics*, 108:1211–1214, 2001.

[195] E.J. Speckmann and C.E. Elgar. Introduction to the neurophysiology, basis of the EEG and DC potentials. In E. Niedermeyer and F. Lopes da Silva, editors, *Basic principles, clinical applications and related fields*, chapter 1, pages 1–13. 2nd edition, 1987.

[196] P. Strobach, K. Abraham-Fuchs, and K. Harer. Event-synchronous cancellation of the heart interference in biomedical signals. *IEEE Trans Biomed Eng*, 41:343–350, 1994.

[197] R. Swarte. *The clinical value of intensive monitoring in term asphyxiated newborns.* PhD thesis, Erasmus universteit, Rotterdam, 2010.

[198] A.C. Tang, M.T. Sutherland, and Ch.J. Mckinney. Validation of SOBI components from high-density EEG. *Neuroimage*, 25:539–553, 2004.

[199] H. Tekgul, K. Gauvreau, and J.S. Soul. Cause and outcome of neonatal seizures in the term newborn infant. *Ann Neurol*, 52:112–114, 2002.

[200] H. Tekgul, K. Gauvreau, and J.S. Soul. The current etiologic profile and neurodevelopmental outcome of seizures in term newborn infants. *Pediatrics*, 117:1270–1280, 2006.

[201] N.V. Thakor and S. Tong. Advances in quantitative electroencephalogram analysis methods. *Annu. Rev. Biomed. Eng.*, 6:453–495, 2004.

[202] E.B. Thoman. A biological perspective and a behavioral model for assessment of premature infants. In L.A. Bond and J.M. Joffee, editors, *Primary prevention of psychopathology: facilitating infant and early childhoud development*. University Press of New England, Hanover, 6 edition, 1982.

[203] M.C. Toet, W. Van der Meij, L.S. de Vries, C. Uiterwaal, and K.C. van Huffelen. Comparison between simultaneously recorded amplitude integrated electroencephalogram (Cerebral Function Monitor) and standard electroencephalogram in neonates. *Pediatrics*, 109:772–779, 2002.

[204] S. Tong, A. Bezerianos, A. Malhotra, Y. Zhu, and N.V. Thakor. Parameterized entropy analysis of EEG following hypoxic-ischemic brain injury. *Phys. Lett.*, 314:354–361, 2003.

[205] S. Tong, Z. Li, Y. Zhu, and N.V. Thakor. Describing the nonstationarity level of neurological signals based on quantifications of time-frequency representation. *IEEE Trans. Biomed. Eng.*, 54:1780–1785, 2007.

[206] S. Tong and N. Thakor. *Quantitative EEG analysis methods and clinical applications*. Artech house, 2009.

[207] Mann T.P. and Elliot R.I.K. Neonatal cold injury due to accidental exposure to cold. *Lancet*, 272:229234, 1957.

[208] K. Van Leemput, F. Maes, D. Vandermeulen, and P. Suetens. Automated model-based tissue classification of MR images of the brain. *IEEE Trans Med Imaging*, 18:897–908, 1999.

[209] M.J.A.M. Van Putten. Neonatal seizure detection. *Clin Neurophysiol*, 119:2417–2418, 2008.

[210] K. Vanderperren, M. De Vos, J.R. Ramautar, N. Novitskiy, M. Mennes, S. Assecondi, B. Vanrumste, P. Stiers, B.R.H. Van den Bergh, J. Wagemans, L. Lagae, S. Sunaert, and S. Van Huffel. Removal of bcg artifacts from eeg recordings inside the MR scanner: A comparison of methodological and validation-related aspects. *NeuroImage*, 50:920–934, 2010.

[211] S. Vanhatalo and K. Kaila. Development of neonatal EEG activity: From phenomenology to physiology. *Seminars in Fetal and Neonatal Medicine*, 11:471–478, 2006.

[212] S. Vanhatalo, J. Voipio, and K. Kaila. Full-band EEG (FbEEG): an emerging standard in electroencephalography. *Clin Neurophysiol*, 116:1–8, 2002.

[213] R.C. Vannucci and J.M. Perlman. Interventions for perinatal hypoxic-ischemic encephalopathy. *Pediatrics*, 100:1004–1014, 1997.

[214] B.V. Vaughn, S.R. Quint, J.A. Messenheimer, R.S. Greenwood, and M.B. Tennison. Heart period variability in seizure-related sinus arrest. *J. Epilepsy*, 10:67–72, 1997.

[215] J. Volpe. *Neurology of the newborn*. Philadelphia, 5th edition, 2008.

[216] M. De Vos. *Decomposition methods with applications in neuroscience.* PhD thesis, Faculty of Engineering, K.U.Leuven, 2009.

[217] C.G. Wasterlain. Recurrent seizures in the developing brain are harmful. *Epilepsia*, 38:728–734, 1997.

[218] K. Watanabe, S. Miyazaki, K. Hara, and S. Hakamada. Behavioral state cycles, background EEGs, and prognosis of newborns with perinatal hypoxia. *Electroencephalogr Clin Neurophysiol*, 49:618–625, 1980.

[219] S.P. Weiner, M.J. Painter, D. Geva, R.D. Guthrie, and M.S. Scher. Neonatal seizures: electroclinical dissociation. *Pediatr Neurol*, 7:363–368, 1991.

[220] V.C. Williams and F.S. Carter. On the rank of a matrix. *Mathematics Magazine*, 41:249–250, 1968.

[221] E. Wirrell, E. Armstrong, L. Osman, and J. Yager. Prolonged seizures exacerbate perinatal hypoxic-ischemic brain damage. *Pediatr Res*, 5:445–454, 2001.

[222] L. Xiaoyan, Z. Ping, and A.S. Alexander. Teager Kaiser energy operation of surface EMG improves muscle activity onset detection. *Ann Biomed Eng*, 35.

[223] J.H. Xue, A. Pizurica, W. Philips, E. Kerre, R. Van de Walle, and I. Lemahieu. An integrated method of adaptive enhancement for unsupervised segmentation of MRI brain images. *Pattern Recognition Letters*, 24:2549–2560, 2003.

[224] P. Zarjam, M. Mesbah, and B. Boashash. An optimal feature set for seizure detection systems for newborn EEG signal. *Proc Int Symp Circuits Syst ISCAS*, 5:33–36, 2003.

[225] V. Zarzoso and P. Comon. Comparative speed analysis of fastica. Technical report, Tech. Report I3S, CNRS/UNSA, 2007.

Publication list

Papers in international journals

1. **W. Deburchgraeve**, P.J. Cherian, M. De Vos, R.M. Swarte, J.H. Blok, G.H. Visser, P. Govaert and S. Van Huffel. Automated neonatal seizure detection mimicking a human observer reading EEG. Clinical Neurophysiology, vol. 119, no. 11, Dec. 2008, pp. 2447-2454.

2. **W. Deburchgraeve**, P.J. Cherian, M. De Vos, R.M. Swarte, J.H. Blok, G.H. Visser, P.Govaert, S.Van Huffel. Neonatal seizure localization using PARAFAC decomposition. Clinical Neurophysiology, vol. 120, no.10, Nov. 2009, pp. 1787-1796.

3. **W. Deburchgraeve**, P.J. Cherian, M. De Vos, R.M. Swarte, J.H. Blok, G.H. Visser, P.Govaert, S.Van Huffel. Time varying neonatal seizure localization Accepted for publication in Methods of Information in Medicine, 2010.

4. J. Taelman , **W. Deburchgraeve**, K. Van Damme, T. Adriaensen, A. Spaepen, S. Van Huffel. Detection algorithm for the firing of a single motor unit in surface electromyography from the trapezius muscle during a mental task. Accepted for publication in Methods of Information in Medicine, 2010.

5. **W. Deburchgraeve**, P.J. Cherian, M. De Vos, R.M. Swarte, J.H. Blok, G.H. Visser, P. Govaert and S. Van Huffel. Automated neonatal EEG artifact removal improving seizure detection. Submitted to Clinical Neurophysiology.

Papers in proceedings of international conferences

6. **W. Deburchgraeve**, B. Vanrumste, A. Vergult, M. De Vos, W. Van Paesschen and S. Van Huffel. Automatic detection and localization of epilepsy in the electroencephalogram. Proc. of the The first Annual

Symposium of the IEEE/EMBS Benelux Chapter. (IEEE EMBS), Brussel, Belgium, Dec. 2006, pp. 321-324.

7. **W. Deburchgraeve**, P.J. Cherian, M. De Vos, R.M. Swarte, J.H. Blok, G.H. Visser, P. Govaert and S. Van Huffel. Automated neonatal spike train detection as part of a neonatal seizure detection system. Proc. Joint Meeting of the 6th International Symposium on Noninvasive Functional Source Imaging of the Brain and Heart and the International Conference on Functional Biomedical Imaging (NFSI), Hangzhou, China, Oct. 2007, pp. 222-225.

8. M. De Vos, L. De Lathauwer, B. Vanrumste, **W. Deburchgraeve**, W. Van Paesschen and S. Van Huffel. Canonical Decomposition of scalp EEG as preprocessing for source localisation. Proc. of the the 6th International Symposium on Noninvasive Functional Source Imaging of the Brain (NFSI 07), Hangzhou, China, Oct. 2007, pp. 377-400.

9. **W. Deburchgraeve**, P.J. Cherian, M. De Vos, R.M. Swarte, J.H. Blok, G.H. Visser, P. Govaert and S. Van Huffel. Exploration of the CP decomposition combined with SVD analysis for neonatal oscillatory seizure localization Proc. of the 6th international Workshop on biosignal interpretation (BSI 2009), New Haven, USA, June 2009, pp. 1-4.

10. J. Taelman, **W. Deburchgraeve**, K. Van Damme, T. Adriaensen, A. Spaepen and S. Van Huffel. Detection algorithm for the firing of a single motor unit in surface electromyography from the trapezius muscle during a mental task. Proc. of the 6th international Workshop on biosignal interpretation (BSI 2009), New Haven, USA, June 2009, pp. 116-119.

11. I. Despotovic, **W. Deburchgraeve**, H. Hallez, E. Vansteenkiste and W. Philips. Development of a realistic head model for EEG event-detection and source localization in newborn infants. Conf Proc. IEEE Eng Med Biol Soc., Minneapolis, USA, Sept. 2009, pp. 2296-2299.

12. J. De Tollenaere, **W. Deburchgraeve**, M. De Vos, S. Van Huffel. New Approaches for the Adaptive Segmentation of Neonatal EEG Signals. Proceedings 4th Annual symposium of the IEEE-EMBS Benelux Chapter, Twente, The Netherlands, Nov. 9-10 2009, pp. 141-144.

13. V. Matic, **W. Deburchgraeve**, S. Van Huffel. Comparison of ica algorithms for ECG artifact removal from EEG signals. Proceedings 4th Annual symposium of the IEEE-EMBS Benelux Chapter, Twente, The Netherlands, Nov. 9-10 2009, pp. 137-140.

Abstracts in proceedings of international conferences

14. **W. Deburchgraeve**, P.J. Cherian, M. De Vos, R.M. Swarte, J.H. Blok, G.H. Visser, P. Govaert and S. Van Huffel. Automated neonatal seizure detection. Proc. of the 3rd International Conference on Brain Monitoring and Neuroprotection in the Newborn, Vienna, Austria, Jan. 2008.

15. **W. Deburchgraeve**, P.J. Cherian, M. De Vos, R.M. Swarte, J.H. Blok, G.H. Visser, P. Govaert and S. Van Huffel. Automated ECG artefact reduction in EEG as a preprocessing step for neonatal seizure detection. Proc. of the Neuromath Workshop, Advanced Methods for the Estimation of Human Brain Activity and Connectivity (Neuromath), Jena, Germany, April 2008.

16. M. De Vos, L. De Lathauwer, **W. Deburchgraeve**, K. Vanderperren and S. Van Huffel. A wide range of BSS applications in neuroscience. Proc. of the 4th European Medical and Biomedical Engineering congress (eMBEC), Antwerp, Belgium, Nov. 2008.

17. **W. Deburchgraeve**, P.J. Cherian, M. De Vos, R.M. Swarte, J.H. Blok, G.H. Visser, P. Govaert and S. Van Huffel. Automated neonatal seizure detection mimicking a human observer reading EEG. Proc. of he 4th International Conference on Brain Monitoring and Neuroprotection in the Newborn, Feb. 2009.

Invited presentations

18. **W. Deburchgraeve**, P.J. Cherian, M. De Vos, R.M. Swarte, J.H. Blok, G.H. Visser, P. Govaert and S. Van Huffel. Geautomatiseerde neonatale aanvalsdetectie gebaseerd op menselijke observator karakteristieken. KNF dagen, Nederlands Vereniging voor Klinische Neurofysiologie, St. Michielsgestel, Nederland, april 2008.

19. **W. Deburchgraeve**, P.J. Cherian, M. De Vos, R.M. Swarte, J.H. Blok, G.H. Visser, P. Govaert and S. Van Huffel. Development of an automated neonatal seizure monitor. NOS-M Symposium: Early development of brain functions, Helsinki, Finland, October 2009.

20. **W. Deburchgraeve**, P.J. Cherian, M. De Vos, R.M. Swarte, J.H. Blok, G.H. Visser, P. Govaert and S. Van Huffel. Development of an automated neonatal seizure monitor. 29th International Congress of Clinical Neurophysiology (ICCN2010), Kobe, Japan, October 2010.

Curriculum vitae

Wouter Deburchgraeve was born in Veurne, Belgium on June 1, 1982. He received the degree of engineer in electronics, from the Katholieke Hogeschool Brugge-Oostende, Belgium in July 2004. He also received the degree of electrotechnical-mechanical engineering, specialisation biomedical techniques, from the Katholieke Universiteit Leuven, Belgium in July 2006. Since then, he has been working as a researcher at the Electrical Engineering Department ESAT of the K.U.Leuven. From October 2006, he worked on a K.U. Leuven PhD grant, and since January 2007 on a I.W.T. grant (Flemisch Institute for Scientific and Technological Research in Industry).

Arenberg Doctoral School of Science, Engineering & Technology
Faculty of Engineering
Department of Electrical Engineering
Research group SISTA-BIOMED
Kasteelpark Arenberg 10, B - 3001 Leuven

